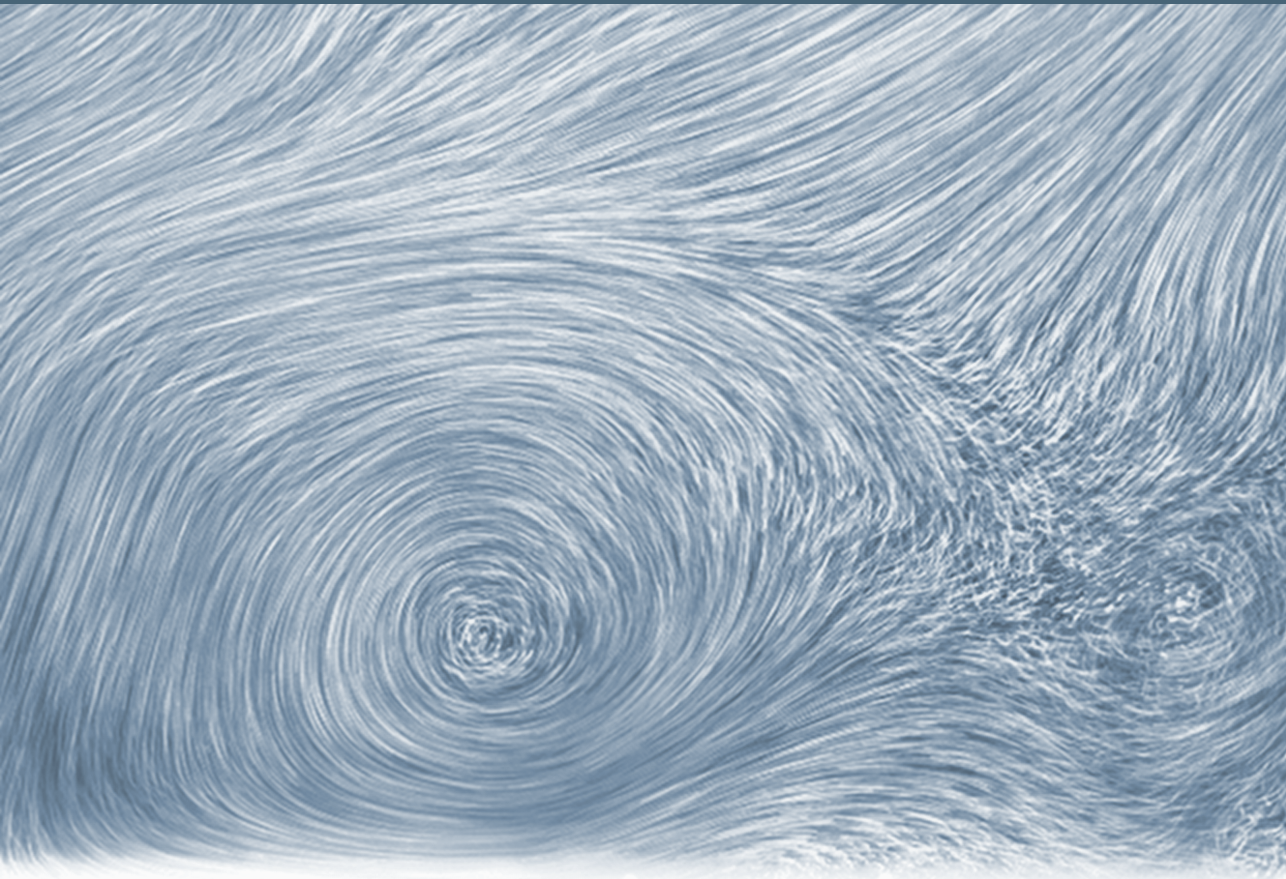


**Long-term unsteadiness and large-scale structures
in Rayleigh-Bénard convection
with and without electromagnetic forcing**



Jos Verdoold

Long-term unsteadiness and large-scale
structures in Rayleigh-Bénard convection
with and without electromagnetic forcing

Jos Verdoold

**Long-term unsteadiness and large-scale structures
in Rayleigh-Bénard convection
with and without electromagnetic forcing**

Proefschrift

ter verkrijging van de graad van doctor
aan de Technische Universiteit Delft,
op gezag van de Rector Magnificus prof.ir. K.C.A.M. Luyben,
voorzitter van het College voor Promoties,
in het openbaar te verdedigen
op dinsdag 26 oktober 2010 om 14.00 uur

door

Jos VERDOOLD

doctorandus in de meteorologie en fysische oceanografie
en doctorandus in de experimentele natuurkunde
geboren te Bergambacht.

Dit proefschrift is goedgekeurd door de promotor:
Prof.dr.Dipl.-Ing. K. Hanjalić

Samenstelling promotiecommissie:

Rector Magnificus	voorzitter
Prof.dr.Dipl.-Ing. K. Hanjalić	Technische Universiteit Delft, promotor
Prof.dr. H.J.J. Jonker	Technische Universiteit Delft
Prof.dr.ir. J. Westerweel	Technische Universiteit Delft
Prof.dr. D. Lohse	Universiteit Twente
Prof.dr.ir. A.A. van Steenhoven	Technische Universiteit Eindhoven
Prof.dr. A. Thess	Technische Universität Ilmenau
Dr.ir. M.J. Tummers	Technische Universiteit Delft

Dr.ir. Tummers heeft als begeleider in belangrijke mate aan de totstandkoming van het proefschrift bijgedragen.



Copyright © 2010 by Jos Verdoold.

All rights reserved. No part of the material protected by the above copyright notice may be reproduced or utilized in any form or by any means, electronic or mechanical, including photocopying, recording or by any information storage and retrieval system without written permission from the author.

Printed by Wöhrmann Print Service, Zutphen, <http://www.wps.nl>.
ISBN 978-90-8570-611-3

Cover: False colour, long exposed liquid crystal image near the bottom wall of the Rayleigh-Bénard convection cell at $Ra \sim 10^8$.

Voor pa en ma
Voor Rianne

Contents

Summary	ix
Samenvatting	xi
1 Introduction	1
1.1 Natural convection	1
1.2 Historical overview	2
1.3 Objectives	4
1.4 Outline	4
2 Theoretical background	7
2.1 Governing equations	7
2.2 Rayleigh-Bénard convection	9
2.3 Magnetohydrodynamics	15
3 Measurement techniques	17
3.1 Laser Doppler anemometry	17
3.2 Particle image velocimetry	23
3.3 Liquid crystal thermography	32
4 Experimental apparatus	47
4.1 Experimental set-up	47
4.2 Measurements	51
4.3 Electromagnetic forcing	58
5 Digital particle image velocimetry and thermometry in turbulent Rayleigh-Bénard convection	63
5.1 Introduction	63
5.2 Methodology	64
5.3 Results	69
5.4 Concluding remarks	73
6 Oscillating large-scale circulation in turbulent Rayleigh-Bénard convection	75
6.1 Introduction	76
6.2 Experimental set-up	77

6.3	Measurement technique	77
6.4	Results	79
6.5	Conclusion	84
7	Spectral analysis of boundary layers in Rayleigh-Bénard convection	85
7.1	Introduction	86
7.2	Methodology	87
7.3	Results	92
7.4	Conclusion	101
8	Prime modes of circulation in large-aspect-ratio turbulent Rayleigh-Bénard convection	103
8.1	Introduction	104
8.2	Experimental method	105
8.3	Karhunen-Loève decomposition	105
8.4	Results	106
8.5	Conclusion	112
9	Electromagnetic forcing visualisations	115
9.1	Introduction	116
9.2	Experimental set-up	117
9.3	Computation and design	120
9.4	Results and discussion	121
9.5	Conclusions and perspectives	125
10	Electromagnetic control experiments	127
10.1	Methodology	128
10.2	Results	130
10.3	Conclusion	138
11	Conclusion	141
	Bibliography	145
	Nomenclature	159
	List of Publications	165
	Dankwoord	167
	About the author	169

SUMMARY

Long-term unsteadiness and large-scale structures in Rayleigh-Bénard convection with and without electromagnetic forcing

This dissertation focuses on turbulent thermal convection, which occurs in a wide range of (geo)physical situations, like in the atmosphere, the oceans, the interior of stars or planets, and in engineering applications, like metal casting or crystal growth processes. In this work, a special type of thermal convection, Rayleigh-Bénard (RB) convection, is studied with and without an additional electromagnetic body force. Experiments are performed in a rectangular RB convection cell of aspect-ratio $\Gamma = 4$ filled with water. Particle image velocimetry (PIV), laser Doppler anemometry (LDA), and liquid crystal thermography (LCT) measurements are used to obtain velocity and temperature information.

Before studying the effects of an electromagnetic body force on RB convection, two characteristic phenomena in RB convection were investigated. First, an investigation of the large-scale circulation (LSC) in RB convection is reported. Secondly, a study of the boundary layers in RB convection is described. In the last part, an electromagnetic body force was added to the natural convection to enhance the heat transfer.

Large-scale circulation in Rayleigh-Bénard convection

LDA and PIV velocity measurements demonstrate that the time-averaged large-scale circulation in the aspect-ratio-four RB convection cell consists of a flow around the periphery that encloses two co-rotating rolls. Using a phase resolving technique, it is shown that the growth and decay of the rolls produce a well-defined period in the velocity components that is maintained for a very long time ($\sim 1 \times 10^4$ s).

Using a large number of PIV realisations, the structure and dynamics of the large-scale circulation in the RB convection cell are shown in detail. For small Rayleigh numbers, $Ra < 10^8$, RB convection in this geometry is characterised by isolated rolls. For higher Ra , two types of flow patterns appear. A three-dimensional model of the LSC is proposed in which the observed co- and counter-rotating modes consistently fit. The model can be generalised to bounded RB convection systems with a broader range than the aspect-ratio-4 cell described in this work.

Boundary layers in Rayleigh-Bénard convection

The second part of this thesis comprises a study of the boundary layer behaviour of RB convection in the aspect-ratio-4 cell. For a wide range of Rayleigh (Ra) numbers varying between 7.0×10^4 and 2.4×10^9 , the results of LDA measurements and direct numerical simulations (DNS) are combined to gain a better insight in the character of the boundary layer.

Probability density functions (pdfs) of the horizontal velocity components show a Gaussian-like shape for the complete Rayleigh number range, except at the lowest Ra where the flow is in a state of spatiotemporal chaos. Pdfs that are scaled with the velocity root-mean-square value overlap for the entire Rayleigh number range, with the exception of the largest Rayleigh numbers where the large-scale circulation, or “wind”, is predominantly visible in the histograms.

The spectral density functions (sdfs) of the horizontal velocity component that were determined in the bulk flow and in the (kinetic) boundary layer are surprisingly similar. Sdfs in both regions of the flow are continuous and have a wide range of active scales for $Ra > 2.6 \times 10^6$, indicating that both are turbulent. However, molecular effects are still noticeable in the boundary layer and the boundary layer does not behave like a classical shear-driven turbulent boundary layer.

Electromagnetic forcing and control

Besides the pure thermally driven forcing, the third part of this dissertation consists of an experimental investigation of the effects of electromagnetic (EM) forcing on an initially stationary conductive fluid layer. Two configurations have been studied: a 2-magnet configuration which is able to generate a well-defined three-dimensional body force that can put the entire liquid bulk into motion without any mechanical stirring, and a 3-magnet configuration which can be used for effective modulation of the wall-boundary layers. Both are of significance to fundamental studies of interactions between fluid flow and electromagnetic fields.

A good agreement is found between the PIV measurements and large-eddy simulations (LES) of the same set-up. By changing the intensity of the imposed DC electric current, different flow regimes can be achieved. A particularly intriguing and interesting feature is the simultaneous presence of different flow regimes in different parts of the setup. The structure of the mean flow and direct effects of the applied EM forcing are identified, such as local heating/cooling regions. The results indicate a great potential in using magnetic fields for designing an efficient control on friction, heat and mass transfer in electrically conducting fluids.

SAMENVATTING

Langdurige onstabieleit en grootschalige structuren in Rayleigh-Bénardconvectie met en zonder elektromagnetische forcering

Dit proefschrift richt zich op turbulente, thermische convectie, welke optreedt in een breed scala van (geo)fysische situaties, zoals in de atmosfeer, de oceanen of in de kern van sterren en planeten, en technische toepassingen, zoals bij het gieten van metalen of kristallisatieprocessen. In dit werk wordt een speciaal type thermische convectie bestudeerd, Rayleigh-Bénardconvectie (RB-convectie), met en zonder een extra elektromagnetische (EM) kracht. De experimenten zijn uitgevoerd in een rechthoekige RB-convectiecel met een breedte-hoogteverhouding van $\Gamma = 4$ gevuld met water. Met behulp van particle-image-velocimetrie (PIV), laser-Doppleranemometrie (LDA) en liquid-crystal-thermografie (LCT) zijn snelheden en temperaturen gemeten.

Voordat de effecten van een elektromagnetische werking op RB-convectie is bestudeerd, zijn eerst twee kenmerkende verschijnselen in RB-convectie onderzocht. Als eerste wordt een onderzoek naar de grootschalige circulatie in RB-convectie gerapporteerd. Daarna wordt een studie van de grenslagen in RB-convectie beschreven. In het laatste deel wordt een elektromagnetische kracht uitgeoefend op RB-convectie om de warmteoverdracht te vergroten.

Grootschalige circulatie in Rayleigh-Bénardconvectie

LDA- en PIV-snelheidsmetingen tonen aan dat de tijdsgemiddelde, grootschalige circulatie in de RB-convectiecel met breedte-hoogteverhouding vier bestaat uit een stroming langs de rand van de cel die twee co-roterende rollen omsluit. Met behulp van een fase-oplossingstechniek wordt aangetoond dat de groei en het verval van de rollen zich voordoen met een goedgedefinieerde periode in de snelheidscomponenten die voor lange tijd stand houdt ($\sim 1 \times 10^4$ s).

Met behulp van een groot aantal PIV-realiserings worden de structuur en de beweging van de grootschalige circulatie in de RB-convectiecellen in detail weergegeven. Voor kleine Rayleighgetallen (Ra), $Ra < 1 \times 10^8$, wordt RB-convectie gekenmerkt door geïsoleerde rollen. Voor grotere Ra verschijnen er twee soorten stromingspatronen. Er wordt een driedimensionaal model van de grootschalige circulatie voorgesteld, waarin de waargenomen co- en contraroterende modi consequent passen. Het mo-

del kan worden gegeneraliseerd naar begrensde RB-convectiesystemen met grotere breedte-hoogteverhoudingen dan beschreven in dit werk ($\Gamma = 4$).

Grenslagen in Rayleigh-Bénardconvectie

Het tweede deel van dit proefschrift bestaat uit een studie van de grenslagen bij RB-convectie in de convectiecel met breedte-hoogteverhouding 4. Voor een groot gebied van Rayleighgetallen variërend van 7.0×10^4 tot 2.4×10^9 zijn de resultaten van LDA-metingen en directe numerieke simulaties (DNS) gecombineerd om een beter inzicht te krijgen in het karakter van de grenslaag.

Kansdichtheidsfuncties (pdf) van de horizontale snelheidscomponenten tonen een Gaussische vorm voor alle Rayleighgetallen, met uitzondering van de kleinste getallen waar de stroming zich in chaotische toestand bevindt in ruimte en tijd. Pdfs die zijn geschaald met het kwadratisch gemiddelde van de snelheid overlappen over het gehele bereik, met uitzondering van de grootste Rayleighgetallen waar de groot-schalige circulatie, de “wind”, duidelijk zichtbaar is in de histogrammen.

De spectra van de horizontale snelheidscomponent in het midden van de cel en in de (kinetische) grenslaag zijn verrassend gelijk. De vermogensspectra van beide locaties in de stroming zijn continu en hebben een brede band van actieve schalen voor $Ra > 2.6 \times 10^6$, wat aangeeft dat beide turbulent zijn. Echter, moleculaire effecten zijn nog steeds aanwezig in de grenslaag en de grenslaag gedraagt zich niet als een klassieke schuifspanningsgedreven turbulente grenslaag.

Elektromagnetische sturing en beheersing

Naast de thermisch-gedreven krachten, wordt in het derde deel van dit proefschrift experimenteel onderzoek beschreven naar de effecten van elektromagnetische (EM) krachten op een aanvankelijk stationaire vloeistof.

Twee configuraties zijn bestudeerd: een twee-magneten-configuratie die in staat is om een goedgedefinieerde driedimensionale kracht uit te oefenen die de gehele vloeistof in beweging brengt zonder mechanische menging, en een drie-magneten-configuratie die gebruikt kan worden voor een effectieve beïnvloeding van de grenslagen bij de wanden. Beide zijn van belang voor fundamenteel onderzoek naar de interactie tussen stromingen en elektromagnetische velden.

Er is goede overeenstemming gevonden tussen PIV-metingen en large-eddy-simulaties (LES) met dezelfde configuratie. Door het veranderen van de intensiteit van de toegepaste elektrische stroom kunnen verschillende stromingstoestanden worden bereikt. Een bijzonder intrigerend en interessante eigenschap van de resulterende stroming is de gelijktijdige aanwezigheid van verschillende stromingstoestanden in verschillende delen van de opstelling. Directe effecten van de toegepaste EM kracht

zijn onderzocht, zoals gebieden met lokale opwarming/afkoeling en de structuur van de gemiddelde stroming. De resultaten geven het grote potentieel weer van het gebruik van magnetische velden bij het ontwerpen van een efficiënte controle van wrijving, warmte- en massatransport in elektrisch-geleidende vloeistoffen.

1

Introduction

1.1 Natural convection

Convection is one of the major modes of heat transfer and mass transfer and occurs in a wide range of (geo)physical situations, like in the atmosphere, the oceans and planetary mantles. It also plays an important role in many engineering applications, like crystal growth processes and in-door climate studies. Convection is enacted by body forces acting within the fluid, such as the gravity field, or surface forces acting at a boundary of the fluid.

Natural convection indicates that a fluid motion is driven by density differences. The gravity field acting on the density differences causes the so-called buoyant force, that moves denser parts of a fluid downwards and lighter parts upwards. In literature, natural convection is sometimes called free convection when an open environment along the flow is concerned. The origin of the density differences can result from a difference in concentration of the fluid's chemical species, a temperature difference, or the presence of multiple phases of the fluid.

This thesis describes an experimental study of natural convection caused by temperature differences. More specifically, it handles the type of convection where a fluid is cooled from above and heated from below, called Rayleigh-Bénard convection. Around 1898, the French physicist Henri Bénard discovered that convection cells spontaneously appear in such systems. In subsequent years he carried out many experiments on this phenomenon, which he reported in his Ph.D. thesis in 1901 (Bénard, 1901). In 1916 Lord Rayleigh, a theorist, published a paper on the stability of fluid layers that were heated from below (Rayleigh, 1916). This was seen as an explanation of the experimental observations made by Bénard. The scaling parameter called after Rayleigh, the Rayleigh number (Ra), quantifies the ratio of

buoyancy forces and viscous forces in the flow.

The convection only occurs above a critical value of the Rayleigh number. For a system with stress free boundaries the onset of turbulent fluid flow occurs at $Ra_c = \frac{27}{4}\pi^4 \approx 656$. For a confined system with two solid walls, the convection patterns start to appear above $Ra_c \approx 1708$.

Rayleigh-Bénard convection plays an important role in many fluid flows in nature. It is a major feature of the dynamics of the oceans and the atmosphere and has a significant role in the interior of stars (Getling, 1998; Bodenschatz et al., 2000). Moreover, the insights gained from Rayleigh-Bénard convection are relevant to numerous industrial processes, especially those involving local cooling and heating.

1.2 Historical overview

Transitions in thermal convection

Since the early 1900s, turbulent Rayleigh-Bénard convection and other natural convection flows triggered scientists to answer many questions. Due to its relatively simple conditions, Rayleigh-Bénard convection became a popular choice for studying e.g. thermal plumes, cellular patterns and heat transfer in fluids. An ongoing topic is the relation between the amount of heat transfer (often characterized by the Nusselt number (Nu), see Section 2.2.3) and the Rayleigh number. Davis (1922) established an empirical relationship of $Nu \sim Ra^{\frac{1}{4}}$ in an air experiment, while Malkus (1954a,b) obtained $Nu \sim Ra^{\frac{1}{3}}$ for a water experiment.

In recent years, new experimental facilities and measurement techniques created a renewed interest in the subject. Chu and Goldstein (1973) performed Rayleigh-Bénard heat transfer experiments in water at moderately large Rayleigh numbers ($10^5 < Ra < 10^8$). Later on, different less viscous fluids were used to increase Ra further. Libchaber (1987), Heslot et al. (1987), Sano et al. (1989), and Castaing et al. (1989) found specific turbulent regimes depending on Ra, earlier described by Kraichnan (1962). They referred to the behaviour in the range $5 \times 10^5 < Ra < 4 \times 10^7$ as “soft turbulence”. From $Ra = 4 \times 10^7$, “hard turbulence” is identified by exponential probability density functions (pdfs) of temperature in the Rayleigh-Bénard cell center, in contrast to Gaussian pdfs for lower Ra. The late 1980s experiments revealed a new Nu-Ra scaling power factor of $\frac{2}{7}$. In more recent years, further transitions were found by changes in the temperature’s power spectrum at $Ra \sim 10^{11}$ and $Ra \sim 10^{13}$.

During the past two decades many studies of Rayleigh-Bénard systems were performed using temperature and pressure probes (e.g. Tong and Shen, 1992; Du and

Tong, 2000; Ching et al., 2003, 2004; Brown and Ahlers, 2006a; He and Tong, 2009), laser Doppler anemometry (e.g. Qiu and Tong, 2002; Qiu et al., 2004) and particle image velocimetry (e.g. Sun et al., 2005a). An overview of the work done in high Rayleigh number convection can be found in review papers from Siggia (1994) and Bodenschatz et al. (2000).

Based on many of those experimental observations, Grossmann and Lohse (2000) proposed a unifying model for the heat transfer scaling in high Rayleigh number convection for different types of fluid, based on the Prandtl number Pr (see Sect. 2.2). Several regimes were identified in the Ra, Pr space, based on the thickness of the kinetic and thermal boundary layer and on whether the bulk or boundary layer is the dominant factor in the dissipation.

Plumes and planform structures

The experiments from the late 1980s, intended to reach very turbulent regimes, used special properties of gases cooled to very low temperatures (typically near 5 K). However, due to those special experimental conditions, point measurements of temperature and pressure were the only measurement sources available.

A different branch of Rayleigh-Bénard experiments involved optical techniques, albeit for moderately high turbulent conditions. Solomon and Gollub (1990) used thermochromic tracers (liquid crystals, see Section 3.3) to visualize Rayleigh-Bénard flows around the transition at $Ra = 4 \times 10^7$. They observed a significant difference between the soft and hard turbulence regimes. For $Ra < 4 \times 10^7$, plumes are coherent across the full height of the cell, whereas for higher values, coherent groups of plumes break up before traversing. Zocchi et al. (1990) and Gluckman et al. (1996) applied the same technique to study the behaviour of the boundary layers. Theerthan and Arakeri (1998, 2000) and Puthenveetil et al. (2005) report on measurements of the near-wall dynamics. Planform structures of plumes emerging in the boundary layer were visualized near the top and bottom walls.

Large scale oscillation

Another important phenomenon in Rayleigh-Bénard convection is the occurrence of a slowly moving mean flow. For convection in a water cell with large aspect ratio $\Gamma = W/H$, where W is the width of the cell and H is its height, Krishnamurti and Howard (1981) and Krishnamurti (1995) reported that a steady large scale flow sets in at $Ra \sim 2 \times 10^6$. This nonzero mean velocity in Rayleigh-Bénard cells was also reported for water cells by Zocchi et al. (1990) and for cryogenic helium cells by Castaing et al. (1989) and Wu and Libchaber (1991) in both large aspect-ratio cells

and $\Gamma = 1$ cells. Moreover, the mean flow tends to reverse itself in a non-periodic way (Niemela et al., 2000).

1.3 Objectives

The interaction between coherent structures and heat transfer is important to understand the nature of the unsteadiness in Rayleigh-Bénard convection in wide horizontal fluid layers. Therefore, the primary objective of the present investigation is to gain a better understanding of the interaction of the flow, coherent structures, and the boundary layer in turbulent Rayleigh-Bénard convection. This is achieved by measuring the fluid velocity and the heat transfer in a confined system of aspect-ratio-4 ($\Gamma = W/H = 4$). To identify coherent flow structures and gather detailed statistics, sophisticated laser diagnostic techniques such as particle image velocimetry (PIV) and laser Doppler anemometry (LDA) are used. Temperature information is obtained with the liquid crystal thermography (LCT) technique. Furthermore, a Karhunen-Loève analysis of the instantaneous velocity fields is used to characterize the long-term flow.

Using the knowledge of the coherent structures and the boundary layer gained from the Rayleigh-Bénard experiments, the second objective is to actively change the behaviour of the boundary layer and the flow in RB convection with an extra, electromagnetic body force. Visualizations and velocity measurements in the same measurement system provided information on two generic EM configurations. These were used in an attempt to control the flow actively, but non-intrusively.

1.4 Outline

In Chapter 2, an introduction is presented on turbulent flows in general and Rayleigh-Bénard convection in particular. Section 2.1 describes the governing equations in turbulent flow and heat transfer processes. Section 2.3 presents a brief overview of the basics of magnetohydrodynamic flows.

Chapter 3 describes the three measurement techniques that were used to measure flow and heat transfer in Rayleigh-Bénard convection and electromagnetically forced flows. Section 3.1 summarizes the basic principles of LDA. PIV is explained in Section 3.2, including optimization criteria and post-processing techniques. Section 3.3 describes the LCT technique, as well as the characteristics of the used thermochromic liquid crystals. Additionally, image processing techniques to obtain accurate field temperature measurements are discussed.

Chapter 4 introduces the experimental set-up which is used throughout this work. First, the experimental rig is described in detail, and in the subsequent sections the modifications made for performing specific measurements are explained.

Chapter 5 describes the results of a simultaneous use of two measurement techniques, i.e. PIV and LCT. Detailed statistical information on both velocity and temperature as well as a detailed study of a thermal plume are presented for Rayleigh-Bénard convection in the $\Gamma = 4$ cell around $Ra \sim 1 \times 10^8$.

Chapter 6 is based on Verdoold et al. (2006a) and reports on a study of the long-term behaviour in the aspect-ratio-four Rayleigh-Bénard convection cell at $Ra \sim 1 \times 10^8$. The existence of a very long periodic component was found with LDA. A similar experiment with PIV revealed a co-rotating flow pattern with the same long periodicity.

Chapter 7 is based on Verdoold et al. (2008) and describes a combined experimental and numerical study of the boundary layer in an aspect-ratio-four Rayleigh-Bénard cell over a four-decade range of Rayleigh numbers. LDA measurements in the boundary layer and the bulk are compared with the results of direct numerical simulations (DNS).

Chapter 8 is based on Verdoold et al. (2009) and extends the view on the large periodic component. The Rayleigh-Bénard convection cell has been observed at a number of different Rayleigh numbers. Long series of instantaneous velocity fields have been analysed using the Karhunen-Loève theorem.

In the second part of this work, electromagnetic forcing acting upon a flow is investigated. Chapter 9 describes visualization experiments in the experimental set-up, with Lorentz forces generated by sub-surface permanent magnets and an external electric field. In Chapter 10, PIV and LCT measurement results are discussed for EM forced flows.

Chapter 11 concludes this thesis with a general discussion of the results obtained.

2

Theoretical background

This chapter gives a brief overview is provided of the governing equations of Rayleigh-Bénard convection and magnetohydrodynamics. The characteristic parameters and scales for turbulent flows driven by buoyancy and by electromagnetic body forces are presented. For full derivations and detailed descriptions of these equations, the reader is referred to textbooks (Tennekes and Lumley, 1972; Nieuwstadt, 1998; Pope, 2000).

2.1 Governing equations

Most flows can be described by the equations for the conservation of mass, momentum and energy. In many textbooks the derivation of the differential form of these equations can be found. For the present research, some simplifications are made. Throughout this work it is assumed that the fluid is Newtonian and the Boussinesq approximation is applied (Sect. 2.2).

Continuity equation

The continuity equation describes the conservation of mass. For incompressible flows, this equation reduces to the criterion that the divergence of the velocity field equals zero:

$$\frac{\partial u_i}{\partial x_i} = 0, \tag{2.1}$$

where u_i is the velocity component in the x_i -direction.

Conservation of momentum

The equation for conservation of momentum is derived from Newton's second law of motion. Under the assumption that the fluid stress is composed of a diffusive viscous term and a pressure term, the Navier-Stokes momentum equation can be described by:

$$\rho \frac{\partial u_i}{\partial t} + \rho u_j \frac{\partial u_i}{\partial x_j} = -\frac{\partial p}{\partial x_i} + \mu \frac{\partial^2 u_j}{\partial x_j^2} + f_i, \quad (2.2)$$

where t denotes time, p is the pressure, μ is the dynamic viscosity of the fluid and f_i is the component of the body forces in the x_i -direction (per unit volume).

The first term on the left-hand side of the equation represents the local temporal change in velocity of a fluid element at a point in space, the second is the advection term. The terms on the right-hand side denote the forces acting on the fluid element, i.e. the forces due to pressure gradients, viscous stress gradients and the body forces, respectively. The body forces f_i include gravitational, centrifugal, Coriolis and electromagnetic forces. In this work, gravitational body forces $f_{i,g}$ and electromagnetic forces $f_{i,em}$ are considered, i.e.,

$$f_i = f_{i,g} + f_{i,em}. \quad (2.3)$$

The gravitational body force is the driving force in Rayleigh-Bénard convection, discussed in Sect. 2.2. The electromagnetic body force will be discussed in detail in Sect. 2.3.

Conservation of energy

The conservation of energy is expressed by

$$\frac{\partial T}{\partial t} + u_j \frac{\partial T}{\partial x_j} = \kappa \frac{\partial^2 T}{\partial x_j^2}, \quad (2.4)$$

where T is the temperature of the fluid and κ is the thermal diffusivity of the fluid. In Eq. 2.4 the first term represents the change of thermal energy of a fluid element in time, the second term is the advection of heat. The term on the right-hand side describes the heat transfer through diffusion (conduction).

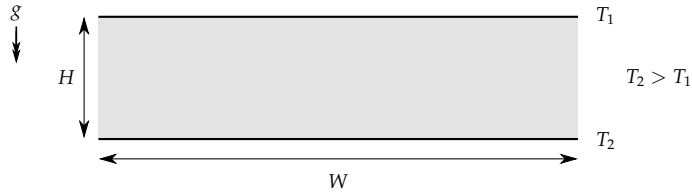


Figure 2.1: Sketch of a Rayleigh-Bénard convection cell. W and H denote the width and the height of the cell, T_1 and T_2 represent the (constant) temperatures of the upper and lower walls, and g is the gravitational acceleration.

2.2 Rayleigh-Bénard convection

Consider a layer of fluid heated from below and cooled from above by constant temperature walls, like in Fig. 2.1. The temperature gradient induces buoyancy as the fluid at the bottom becomes lighter than at the top due to thermal expansion. Viscosity and thermal diffusivity will dampen this convective motion to some extent close to the walls. When the gradient across the fluid layer is large enough, a convective motion sets in.

The momentum equation for Rayleigh-Bénard convection is given by Eq. 2.2 where the gravitational force $f_{i,g}$ is the only body force (per unit volume). It is defined by

$$f_{i,g} = -\rho g, \quad (2.5)$$

where g denotes the vertical component of the gravitational acceleration vector \vec{g} .

In the Boussinesq approximation (Boussinesq, 1903), density fluctuations ρ' are assumed to be sufficiently small compared to a reference density ρ_0 ($\rho'/\rho_0 \ll 1$) and all density variations can be neglected except the term with the gravitational acceleration g in the momentum equation (Nieuwstadt, 1998; Bird et al., 2007). In that case the density is assumed to vary linearly with the temperature and by Taylor approximation of the density around a reference temperature T_0 , this results in

$$\rho(T) = \begin{cases} \rho_0[1 - \alpha(T - T_0)] & \text{in the term } \rho g; \\ \rho_0 & \text{elsewhere;} \end{cases} \quad (2.6)$$

where T is the temperature, and α is the thermal expansion coefficient of the fluid defined by

$$\alpha = -\frac{1}{\rho_0} \left. \frac{\partial \rho}{\partial T} \right|_{T_0}. \quad (2.7)$$

From a zero-order balance (without flow, $u_i = 0$, and no density fluctuations, $\rho = \rho_0$) a deviatory pressure p' is defined:

$$p' = p + \rho_0 g . \quad (2.8)$$

Combined with Eqs. 2.2 and 2.6 this leads to

$$\frac{\partial u_i}{\partial t} + u_j \frac{\partial u_i}{\partial x_j} = -\frac{1}{\rho_0} \frac{\partial p'}{\partial x_i} + \nu \frac{\partial^2 u_j}{\partial x_j^2} + \alpha (T - T_0) g_i , \quad (2.9)$$

where ν is the kinematic viscosity, defined as $\nu = \mu / \rho_0$.

To describe the characteristics of Rayleigh-Bénard convection in a consistent way, several relevant dimensionless numbers are used. To obtain their definitions, the governing Equations 2.1, 2.2 and 2.4 are rewritten in dimensionless form. A characteristic length scale L , characteristic velocity κ / L and characteristic temperature difference $T_1 - T_0$ are chosen to define the following dimensionless variables: $\tilde{x}_i = \frac{x_i}{L}$, $\tilde{u}_i = \frac{u_i L}{\kappa}$ and $\tilde{T} = \frac{T - T_0}{T_1 - T_0}$. Dimensionless time and pressure scales can be defined by $\tilde{t} = \frac{t \kappa}{L^2}$ and $\tilde{p}' = p' \frac{L^2}{\rho \kappa^2}$ respectively. From these definitions, a dimensionless set of Navier-Stokes equations follow:

$$\frac{\partial \tilde{u}_i}{\partial \tilde{x}_i} = 0 , \quad (2.10)$$

$$\frac{1}{\text{Pr}} \left[\frac{\partial \tilde{u}_i}{\partial \tilde{t}} + \tilde{u}_j \frac{\partial \tilde{u}_i}{\partial \tilde{x}_j} + \frac{\partial \tilde{p}'}{\partial \tilde{x}_i} \right] = \frac{\partial^2 \tilde{u}_i}{\partial \tilde{x}_j^2} + \text{Ra} \tilde{T} , \quad (2.11)$$

$$\frac{\partial \tilde{T}}{\partial \tilde{t}} + \tilde{u}_j \frac{\partial \tilde{T}}{\partial \tilde{x}_j} = \frac{\partial^2 \tilde{T}}{\partial \tilde{x}_j^2} . \quad (2.12)$$

The pre-factor in the last term of Eq. 2.11 is the Rayleigh number, which is the ratio of the thermal driving buoyancy force and the viscous force, defined as

$$\text{Ra} = \frac{\alpha g \Delta T L^3}{\nu \kappa} , \quad (2.13)$$

with $\Delta T = T_1 - T_0$.

Furthermore, on the left-hand side in Eq. 2.11, the Prandtl number is introduced, defined as the ratio of the diffusion of momentum and the diffusion of heat:

$$\text{Pr} = \frac{\nu}{\kappa} . \quad (2.14)$$

A third important dimensionless number, the Reynolds number, describes the ratio of inertial forces to the viscous forces:

$$\text{Re} = \frac{\rho U^2}{\frac{\mu U}{L}} = \frac{\rho}{\mu} UL = \frac{UL}{\nu}, \quad (2.15)$$

where U is a characteristic velocity.

The mathematical Rayleigh-Bénard problem is defined for a fluid layer of infinite extent in horizontal directions. However, in practice, Rayleigh-Bénard convection is studied in cells with finite horizontal dimensions. Therefore, the aspect-ratio Γ of the system is introduced:

$$\Gamma = \frac{W}{H} \quad (2.16)$$

where W and H are the width and the height of the cell, respectively.

2.2.1 Scale parameters

Macro scales

At the macro scale, the flow can be described by the following characteristic variables:

$$U_* = \sqrt{\alpha g \Delta T L}, \quad (2.17)$$

$$t_* = \frac{L}{U_*}, \quad (2.18)$$

$$L_* = L. \quad (2.19)$$

U_* can be derived from the concept of the free-fall velocity. Consider a fluid package at the top of the convection cell, with a density difference $\Delta\rho$ compared to the bulk density ρ . Assuming this package falls with the free fall velocity, it must obey the relation (based on conservation of energy):

$$\Delta\rho g L \sim \rho U_*^2. \quad (2.20)$$

Combining this equation with the integral form of the thermal expansion coefficient α (Eq. 2.7)

$$\frac{\Delta\rho}{\rho} = \alpha \Delta T, \quad (2.21)$$

results in Eq. 2.17.

Dissipative scales

The flow's dissipative scales can be derived from their relationship with the macro scales by the dissipation of kinetic energy. The kinetic energy k scales corresponding to $k \sim U_*^2$ as the large structures, are the most energetic. As the change of k is related to viscous dissipation ε by $\frac{dk}{dt} = -\varepsilon$, this results in

$$\varepsilon \sim \frac{U_*^3}{L}. \quad (2.22)$$

As mentioned before, the turbulent energy cascade process facilitates the transfer of produced energy at large scales to the smaller scales where it is dissipated. At the micro scale, there are only two important parameters, the kinematic viscosity ν and the amount of energy to be dissipated ε . Using dimensional analysis, this results in the following micro scales for length, velocity and time (Nieuwstadt, 1998):

$$\eta = \left(\frac{\nu^3}{\varepsilon} \right)^{\frac{1}{4}} = L\text{Re}^{-\frac{3}{4}}, \quad (2.23)$$

$$u_\eta = (\nu\varepsilon)^{\frac{1}{4}} = U_*\text{Re}^{-\frac{1}{4}}, \quad (2.24)$$

$$\tau_\eta = \left(\frac{\nu}{\varepsilon} \right)^{\frac{1}{2}} = \frac{\eta}{u_\eta}. \quad (2.25)$$

2.2.2 Reynolds decomposition

The conservation equations mentioned in Sect. 2.1 combined with initial and boundary conditions can fully describe laminar and turbulent flows. However, the equations will not lead to an exact solution. The instantaneous velocity, pressure and temperature values can then only be described in terms of probability. This leads to the introduction of averaged values. Each instantaneous quantity can be split into a mean value and a fluctuation:

$$\begin{aligned} u_i &= \bar{u}_i + u'_i, \\ p &= \bar{p} + p', \\ T &= \bar{T} + T'. \end{aligned} \quad (2.26)$$

In this *Reynolds decomposition* \bar{u}_i , \bar{p} and \bar{T} denote the ensemble (or time-averaged) values of velocity, pressure, and temperature, respectively, and u'_i , p' and T' are the corresponding fluctuations.

Substitution of Eq. 2.26 into Eq. 2.1 results in a Reynolds-averaged continuity equation:

$$\frac{\partial \bar{u}_i}{\partial x_i} = 0. \quad (2.27)$$

Substituting Eq. 2.26 into Eq. 2.2, and taking the Reynolds average yields

$$\rho \frac{\partial \bar{u}_i}{\partial t} + \rho \bar{u}_j \frac{\partial \bar{u}_i}{\partial x_j} = -\frac{\partial \bar{p}}{\partial x_i} + \frac{\partial}{\partial x_j} \left[\mu \frac{\partial \bar{u}_i}{\partial x_j} - \overline{u'_i u'_j} \right] + f_i, \quad (2.28)$$

where the $\overline{u'_i u'_j}$ term denotes the Reynolds stress tensor, originating from the non-linear advection term.

The Reynolds stress tensor can be interpreted as the transport of fluctuating momentum per unit mass u_i in x_i -direction by velocity fluctuations in the x_j -direction. The Reynolds stress tensor is a new unknown giving rise to the so-called “turbulence closure” problem.

Substitution of Eq. 2.26 into the energy equation Eq. 2.4 and taking the ensemble average results in

$$\frac{\partial \bar{T}}{\partial t} + \bar{u}_j \frac{\partial \bar{T}}{\partial x_j} = \frac{\partial}{\partial x_j} \left[\kappa \frac{\partial \bar{T}}{\partial x_j} - \overline{u'_j T'} \right], \quad (2.29)$$

where the term $\overline{u'_j T'}$ appears. It is known as the turbulent heat flux, and it represents the heat transfer counterpart of the turbulent momentum transfer described above.

Another important quantity in turbulent flows is the turbulence kinetic energy per unit mass, k , defined as $k = \frac{1}{2} \overline{u_i'^2}$. By multiplying Eq. 2.28 by \bar{u}_i , taking an ensemble average of all terms and subtracting the equation of kinetic energy conservation of the mean flow (see Tennekes and Lumley, 1972), one obtains the k -equation or turbulence kinetic energy budget:

$$\frac{\partial k}{\partial t} + \bar{u}_j \frac{\partial k}{\partial x_j} = P_k - \varepsilon + \mathcal{T}_k + \mathcal{P}_k + \mathcal{D}_k, \quad (2.30)$$

with

$$P_k = -\overline{u'_i u'_j \frac{\partial \bar{u}_i}{\partial x_j}}, \quad (2.31)$$

$$\varepsilon = \nu \overline{\frac{\partial u'_i}{\partial x_j} \frac{\partial u'_i}{\partial x_j}}, \quad (2.32)$$

$$\mathcal{T}_k + \mathcal{P}_k + \mathcal{D}_k = -\frac{\partial \overline{u'_j k'}}{\partial x_j} - \frac{1}{\rho} \frac{\partial \overline{p' u'_j}}{\partial x_j} + \nu \frac{\partial^2 k}{\partial x_j^2}, \quad (2.33)$$

where P_k is the production of k , ϵ is the viscous dissipation of k , $k' = \frac{1}{2}u'_i u'_i$ and \mathcal{T}_k , \mathcal{P}_k , and \mathcal{D}_k represent transport of k by velocity fluctuations, pressure fluctuations and diffusion, respectively.

Turbulence kinetic energy is produced (P_k) at large scales by the deformation of the mean flow field. The energy is transferred to smaller scales by vortex stretching. The three transport mechanisms \mathcal{T}_k , \mathcal{P}_k , \mathcal{D}_k distribute the energy through the flow. The molecular diffusive term \mathcal{D}_k is only of influence near walls. At the smallest scales in the flow, energy is eventually dissipated by molecular diffusion (ϵ).

2.2.3 Heat transfer

Radiative heat transfer from a surface is described by the Stefan-Boltzmann law for an ideal black body. For real surfaces an emissivity factor ϵ needs to be introduced:

$$q''_{\text{rad}} = \epsilon \sigma_B T_{\text{surf}}^4, \quad (2.34)$$

where q''_{rad} is the radiative heat flux, σ_B is the Boltzmann constant, and T_{surf} the surface temperature. Conductive heat transfer is proportional to the temperature gradient and is described by Fourier's law of heat conduction:

$$q''_{\text{cond}} = -\lambda \frac{dT}{dx}, \quad (2.35)$$

where q''_{cond} is the conductive heat flux, λ is the thermal conductivity, and dT/dx is the temperature gradient.

Where heat is transferred from a solid surface to an adjacent flowing liquid or gas, convective heat transfer takes place. The rate of heat transfer by convection is described by Newton's law of cooling:

$$q''_{\text{conv}} = -h(T_{\text{surf}} - T_{\text{bulk}}), \quad (2.36)$$

where q''_{conv} is the convective heat flux, h the convective heat transfer coefficient, and T_{surf} and T_{bulk} are the temperatures of the surface and bulk liquid, respectively.

The heat transfer coefficient h is often non-dimensionalised using the thermal conductivity of the fluid, λ , and a length scale, L , typical for the geometry. This leads to the definition of the dimensionless Nusselt number:

$$\text{Nu} = \frac{hL}{\lambda}. \quad (2.37)$$

The Nusselt number is the ratio of the total heat transfer in case of convection and the heat transfer in case of a stagnant fluid.

2.3 Magnetohydrodynamics

In order to find an equation for the electromagnetic body force $f_{i,em}$ from Eq. 2.3, some additional equations are needed to relate the various electromagnetic quantities. This section gives a quick overview of relevant equations for the present work. For more information on electrodynamics, the reader is referred to Griffiths (1989) and Jackson (1999). Further details on magnetohydrodynamics (MHD) can be found in Moreau (1990) and Davidson (2001).

2.3.1 Electromagnetic equations

The force on a moving point charge q with velocity \vec{u} , caused by electromagnetic fields \vec{E} and \vec{B} , is called the Lorentz force

$$\vec{F} = q \left[\vec{E} + \vec{u} \times \vec{B} \right]. \quad (2.38)$$

In this expression the first term describes the Coulomb force, which is important in electrostatics but negligible in conducting media. Within the electromagnetic approximation, Eq. 2.38 is generalised as a Laplace force, the force per unit volume on an electric current in a conductor (Moreau, 1990):

$$\vec{f} = \vec{j} \times \vec{B}. \quad (2.39)$$

The relation between the electric current density \vec{j} , the electric field \vec{E} , the magnetic field \vec{B} and the velocity field \vec{u} is given by Ohm's law. It connects the electric current density in the presence of a magnetic field and is defined by

$$\vec{j} = \sigma(\vec{E} + \vec{u} \times \vec{B}), \quad (2.40)$$

where σ is the electrical conductivity of the medium. At the right-hand side, the first term describes the current due to the presence of the electrical field \vec{E} . The second term adds the induced current from the motion of the fluid with velocity \vec{u} through a magnetic field \vec{B} .

The Maxwell-Faraday law of induction shows that a spatially varying electric field can induce a magnetic field:

$$\vec{\nabla} \times \vec{E} = -\frac{\partial \vec{B}}{\partial t}. \quad (2.41)$$

Maxwell-Ampère's circuital law relates the electric current passing through a closed loop with a magnetic field around the loop:

$$\vec{\nabla} \times \vec{B} = \mu_0 \vec{j} + \mu_0 \epsilon_0 \frac{\partial \vec{E}}{\partial t}, \quad (2.42)$$

where μ_0 is the permeability of free space and ϵ_0 is the permittivity of free space.

Combining Eqs. 2.40, 2.41, and 2.42 and assuming that the electric field will not vary in time, results in the induction equation:

$$\frac{\partial \vec{B}}{\partial t} = \vec{\nabla} \times (\vec{u} \times \vec{B}) + \frac{1}{\mu_0 \sigma UL} \vec{\nabla}^2 \vec{B}. \quad (2.43)$$

The denominator of the fraction in the last term of this equation is called the magnetic Reynolds number Re_m :

$$Re_m = \mu_0 \sigma UL. \quad (2.44)$$

It describes the ratio of advection to diffusion of the magnetic field.

2.3.2 Scaling parameters

Two scaling parameters are introduced to characterise the driving forces of the flow. The squared Hartmann number Ha is the ratio of the electromagnetic driving force and the viscous force in the boundary layer and is defined as

$$Ha^2 = \frac{\sigma E B_0}{\rho \nu U / L^2}, \quad (2.45)$$

where B_0 is the characteristic magnitude of the magnetic field and E , U and L are respectively the characteristic electric field, velocity and length of the system. The Stuart number or magnetic interaction parameter N relates the electromagnetic forces to inertial forces and is defined as

$$N = \frac{Ha^2}{Re} = \frac{\sigma E B_0 L}{\rho U^2}. \quad (2.46)$$

3

Measurement techniques

In this chapter the basic principles of the techniques for measuring velocity and temperature will be discussed. Laser Doppler anemometry and particle image velocimetry will be introduced first. These are two non-intrusive techniques for measuring velocities at a single point at high time resolution, and in a plane of interest, respectively. Further on in this chapter, liquid crystal thermography will be discussed. This temperature measurement technique is used in both sheet-like and suspended forms, sharing the same principles. Parts of this chapter are drawn upon Raffel et al. (1998, 2007), Tummers (1999), and Geers (2004).

3.1 Laser Doppler anemometry

The laser Doppler anemometry (LDA) technique is based on the Doppler effect. When light is scattered by small tracer particles that move with the flow, a frequency shift will occur. This Doppler frequency shift is related to the velocity of the particle. By measuring the Doppler frequencies, accurate information on fluid velocities can be obtained, assuming that the particles accurately follow the flow. While discussing the basics of LDA in this section, the focus lies on a dual beam (shifted) LDA system. For a more complete description of the principles of the LDA measurement technique the reader is referred to Absil (1995) and Tropea et al. (2007).

3.1.1 Measurement principle

Figure 3.1 depicts the optical arrangement of a dual-beam LDA system. A continuous laser provides a light beam with frequency $f_0 = c/\lambda_0$ that is subsequently transformed into two equal intensity beams by a beam splitter, with c is the speed of light

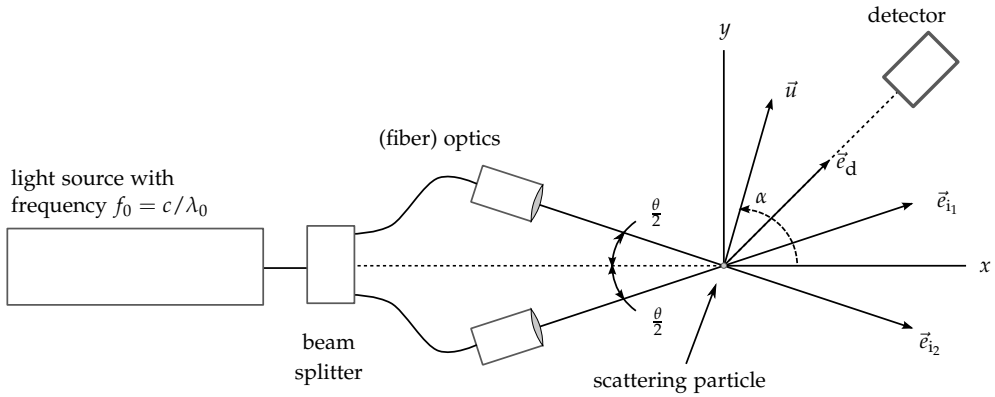


Figure 3.1: Schematic of the optical arrangement for the dual-beam LDA system.

and λ_0 is the wavelength of the beam. The unit vectors \vec{e}_{i_1} and \vec{e}_{i_2} indicate the directions of the incident beams. The beams are crossed with crossing angle θ and are focused in one point thus forming a small measurement volume. Particles that move through this volume scatter the light of both beams. According to the Lorenz-Mie scattering theory the light is scattered in all directions. As a result the photomultiplier receives light with two different frequencies f_1 and f_2 given by

$$\left. \begin{aligned} f_1 &= f_0 + \vec{u} \cdot (\vec{e}_d - \vec{e}_{i_1}) / \lambda_0 \\ f_2 &= f_0 + \vec{u} \cdot (\vec{e}_d - \vec{e}_{i_2}) / \lambda_0 \end{aligned} \right\} \Rightarrow f_D \equiv f_2 - f_1 = \frac{\vec{u} \cdot (\vec{e}_{i_1} - \vec{e}_{i_2})}{\lambda_0}, \quad (3.1)$$

where λ_0 is the wavelength of the laser light, \vec{e}_d the unit vector in the direction of the scattered light falling onto the detector and \vec{u} the velocity vector of the scattering particle. When both frequencies are mixed on a photodetector, the resulting output signal will oscillate with the difference frequency of the beams, the Doppler frequency f_D .

As the photomultiplier not only receives light from the scattering particle, filtering of the detector's output signal is required. High-pass and low-pass band filters remove the pedestal of the signal and the high frequency noise respectively, which -ideally- results in a clean signal. This signal is called the Doppler burst, which oscillates with the Doppler frequency f_D .

3.1.2 Fringe model

A frequently used procedure to relate the Doppler frequency to the velocity of the scattering particle is given by the "fringe model". The fringe model focuses on the

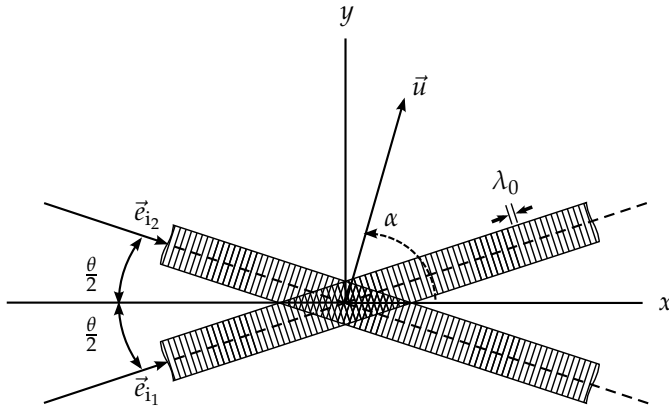


Figure 3.2: The interference pattern of two plane light waves.

interference pattern generated by planar waves of the incident beams crossing in the measurement volume, as depicted in Fig. 3.2.

The maxima of the light intensity in the interference pattern shown in Fig. 3.2 have a regular spacing, the fringe spacing d_f , which is given by

$$d_f = \frac{\lambda_0}{2 \sin(\theta/2)}. \quad (3.2)$$

The velocity component in the y -direction can now easily be computed by multiplying the measured Doppler frequency with the fringe spacing, i.e. $u_y = f_D d_f$.

As the photodetector cannot observe a difference between particles moving with velocities \vec{u} or $-\vec{u}$, the obtained velocities from LDA are directionally ambiguous. To overcome this problem, a frequency pre-shift is commonly used. The frequency of one of the incident beams is shifted by a small constant value f_s using an acousto-optic Bragg cell. This pre-shift frequency changes Eq. 3.1 into

$$f_D = f_s + \frac{\vec{u} \cdot (\vec{e}_{i1} - \vec{e}_{i2})}{\lambda_0}. \quad (3.3)$$

If the frequency shift f_s is chosen larger than the Doppler frequency corresponding to the smallest velocity in the flow, each value of $|f_D|$ is uniquely related to one velocity value and the directional ambiguity is removed.

For simultaneously measuring more than one velocity component, multiple single-point LDA systems operating on laser beams with different wavelengths, can be combined. When equipped with specific narrow band filters, the photomultipliers

are able to distinguish between the light coming from the different LDA systems. When carefully aligning the different coloured laser beams in such a way that the measurement volumes spatially overlap, one could measure the instantaneous velocity of a scattered particle in more than one direction. While post-processing the data, a time coincidence window filter is used to ensure that the same particle is observed on different channels.

The fringe model description is physically not fully correct, as the mixing of scattered light takes place on the detector and the detector does not “see” the light intensity. Nonetheless, it proves to be a convenient way to explain the system’s characteristics and to perform the calibration of the dual-beam LDA system.

3.1.3 Seeding particles

The LDA measurement technique relies on seeding particles to measure fluid velocities. Seeding or tracer particles have to be small enough to follow the flow properly. Too large or too heavy particles do not respond quickly enough to rapid changes in the velocity of the fluid. Additionally, tracer particles need to be neutrally buoyant during the experiment. The difference between the density of the fluid ρ and the particle ρ_p needs to be as low as possible. From Stokes’ law, one can deduce the following equation for the characteristic time scale τ_D associated with the dynamic behaviour of particles:

$$\tau_D = \frac{(\rho_p - \rho)d_p^2}{18\eta}, \quad (3.4)$$

where η is the dynamic viscosity of the fluid and d_p is the diameter of the tracer particle.

In general it can be said that the light scattering by small particles is a function of the ratio of the refractive index of the particles to that of the surrounding medium (Raffel et al., 1998). In addition, the light scattering also depends on the polarisation of the light and observation angle.

As the refractive index of water is considerably larger than that of air, the scattering of particles in water is at least one order of magnitude smaller compared to particles in air of the same size. Therefore larger particles have to be used for water flow experiments, which is practical since the particle’s density can now more easily be matched with the density of water. For gas flows the diameter of the particles is typically near $1 \mu\text{m}$, while for liquid flows it is typically between $10 \mu\text{m}$ and $100 \mu\text{m}$.

The scattering efficiency of small particles is strongly dependent on the observation angle. In Fig. 3.3 the polar distribution of the scattered light is depicted for three dif-

ferently sized glass particles in water. Smaller particles have a large scatter efficiency in the forward direction, but they scatter much less light to the side and back of the particle. For backward scatter systems, larger particles have to be used.

For a given laser light intensity, an optimum particle size can be found. The scattering intensity as well as the lag time of the particle are proportional to the square of the particle size. A smaller particle will more accurately follow the flow, but result in smaller scattering intensities. Moreover, the fringe spacing is also a limiting factor. For particles that have the same size or are larger than the fringe spacing, the amplitude of the Doppler signal is largely reduced, resulting in a lowering of the signal-to-noise ratio.

3.1.4 Velocity bias

When LDA measurements are performed in time varying flows, the probability of measuring high velocities is larger than that of low velocities. This is the so-called *velocity bias* in LDA. Consider a measurement volume in a time varying flow which is crossed by a certain number of particles. The expected number of particles ϑ_p moving through the volume per unit time can be written as

$$\vartheta_p = |\vec{u}|C_pA_p, \quad (3.5)$$

where C_p is the number concentration of the particles, \vec{u} is the instantaneous velocity vector, and A_p is the area of the projection of the volume on a plane normal to \vec{u} . The equation shows that the number of particles depends on the particle volume flux $|\vec{u}|A_p$. Therefore, the probability of measuring high-velocity particles is higher than the probability of measuring low velocity particles. This leads to velocity probability density functions biased to high values, underestimating near-zero values, which will eventually result in a systematic error in all statistical quantities (Tummers, 1999).

In general, two types of methods are known to correct for this bias. From a signal processing point of view, the discrete samples can be transformed into a signal with equidistant time intervals at a high frequency. For these reconstruction techniques the data density, defined as the product of the mean data rate ϑ_p and a characteristic time scale of the velocity, is crucial. Commonly, all resampling techniques require a high sampling rate for successful processing and are nearly impossible to use with the intermittent signals obtained in the present Rayleigh-Bénard experiments.

An alternative is the use of weight functions, where each velocity is compensated for the velocity bias during the processing of the velocity samples. The (unbiased) mean velocity and the (unbiased) variance of the velocity fluctuations are then computed

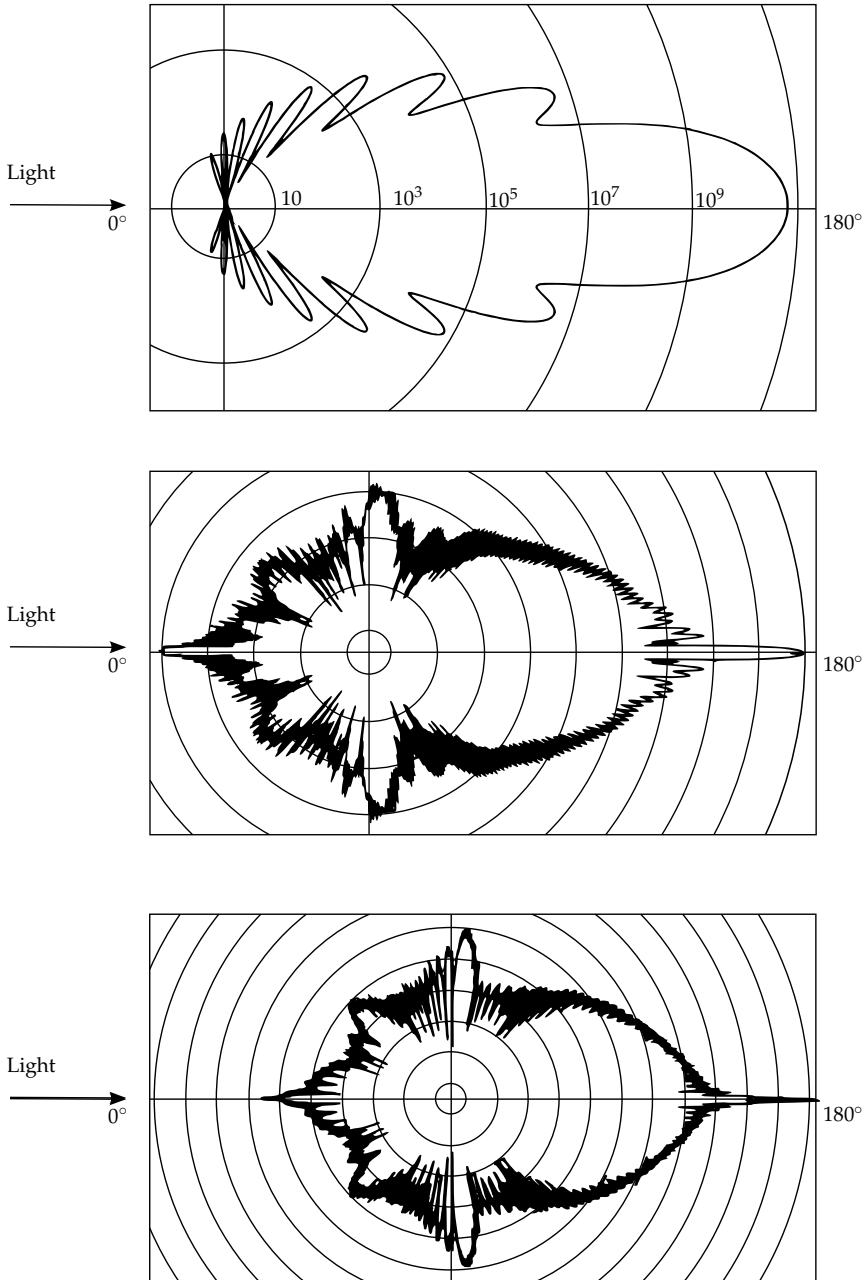


Figure 3.3: Light scattering by a 1 μm (top), 10 μm (centre) and 30 μm (bottom) glass particle in water (Raffel et al., 1998). Logarithmic scale, neighbouring circles differ by a factor 100.

from

$$\bar{u} = \frac{\sum_{i=1}^N w_i u_i}{\sum_{i=1}^N w_i}, \quad (3.6)$$

$$\overline{u'^2} = \frac{\sum_{i=1}^N w_i (u_i - \bar{u})^2}{\sum_{i=1}^N w_i}, \quad (3.7)$$

where u_i is the velocity of the i^{th} sample, w_i is the weight factor for the i^{th} sample, and N is the total number of samples.

Three commonly used weight functions are the inverse-velocity, interarrival-time and transit-time weighting. For the first, w_i is defined as the inverse of the volume flux $1/(\bar{u}^2 A_p)$, Eq. 3.5, (McLaughlin and Tiederman, 1973). For measurements in two dimensions, it is simplified to the reciprocal of the Eulerian vector length in two dimensions. This reduction leads to a weight factor that is systematically too large, resulting in a too strong correction for the velocity bias (Tummers, 1999). The second frequently used weight factor is the interarrival-time weighting (Barnett and Bentley, 1974). The interarrival time is defined as the time interval between consecutive particles passing through the measurement volume. Interarrival-time weighting requires a high data rate to be accurate, but an advantage is that it can be used when the particle concentration is correlated with the local velocity. A third commonly used weighting is the transit-time weight factor. Hoesel and Rodi (1977) show that weighting with the inverse volume flux is equivalent to weighting with the mean time particles need to pass through the measurement volume. As Petrie et al. (1988) showed, the transit-time of a particle is related to the pathway of the particle through the volume. Hence, the transit-times values scatter around their mean value, which increases the statistical scatter of the derived statistical quantities. Tummers (1999) shows that for a sufficiently high number of samples, the two-dimensional inverse-velocity and the transit-time weighting lead to almost identical results.

Due to the intermittent character of Rayleigh-Bénard convection, the transit-time weighting is applied in the present work.

3.2 Particle image velocimetry

Particle image velocimetry (PIV) is a non-intrusive measurement technique that allows the measurement of velocities in a planar cross-section of the fluid. Small tracer particles added to the flow are illuminated at least twice within a short time interval. The scattered light from the particles is recorded by a camera on two consecutive images. The particle displacements are determined by calculating the correlation between the first and the second image. Velocity vectors then follow by dividing the measurement displacement by the time between the two images.

This section briefly describes the principles of the PIV technique. For a more detailed review the reader is referred to Westerweel (1993) and Raffel et al. (1998, 2007).

Seeding material

The requirements for the seeding particles for PIV are generally equal to those for LDA. The seeding particles for PIV should follow the flow within a lag-time (Eq. 3.4) that is typically smaller than the flow time scales. Furthermore, the light scattered by the particles must have sufficient intensity to be recorded properly. To obtain a well recorded particle image, the contrast between background and particles needs to be as large as possible by choosing the right particle size and by increasing the laser power.

Light source

The tracer particles in the fluid are usually illuminated with a pulsed light source. For PIV systems frequency doubled Nd:YAG or Nd:YLF lasers are mostly used, producing light at wavelengths of 532 nm and 527 nm, respectively. The coherence of these type of lasers eases the alignment of the system and their monochromaticity allows easy collimation of the light beam. Nd:YAG and Nd:YLF lasers are employed for their constant pulse energy within pulses of a few nanoseconds (in the order of 10 ns and 100 ns respectively).

The duration of the light pulse should be short compared to the flow's typical time scales in order to avoid motion blur in the particle images. To generate two pulses shortly after each other, two laser cavities are used, as can be seen in Fig. 3.4. Precision optics are used to precisely overlap the beams.

After the beam leaves the laser it passes through a combination of lenses to form a light sheet. A typical combination of two cylindrical lenses is depicted in Fig. 3.5. There are multiple lens combinations to create this light sheet. The reader is referred to Raffel et al. (2007) for more details.

Image acquisition and image sensors

In general two types of electronic image sensors can be used for digital recording: a charge coupled device (CCD) and a complementary metal oxide semiconductor (CMOS). Both types of sensors use silicon photodiodes to convert light into electrical energy by the photoelectric effect, i.e. charge is accumulated by incident

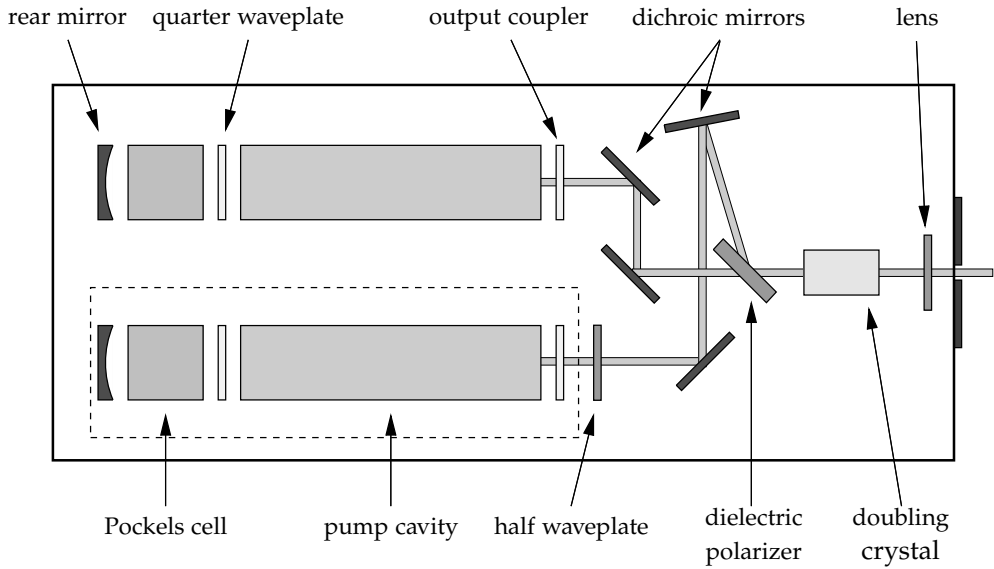


Figure 3.4: Schematic of a typical dual Nd:YAG laser, after Raffel et al. (1998); Geers (2004).

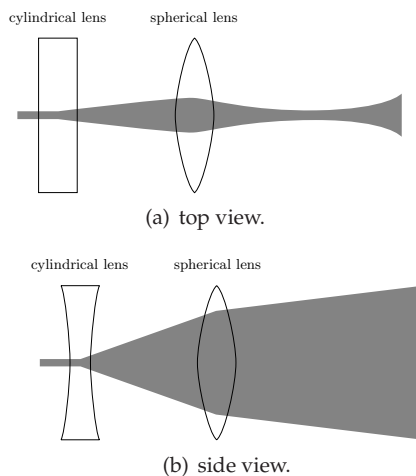


Figure 3.5: Sketch of the lens arrangement for creating a light sheet.

3 photons freeing electrons from the silicon lattice. CMOS sensors are characterised by the way the sensor is manufactured. To measure the collected signal charge, these charges are converted into voltages by a capacitor. CCDs are named after the method by which charges are read after exposure. This happens at one output node of the CCD sensor array where the voltage is amplified and send off-chip. Row by row, the measured charges are fed to a read-out register. The charges on each row are “coupled” to those on the row above. When a row moves down the next row occupies its space. From the read out register the charges are fed to the output node pixel by pixel.

CMOS sensors convert charge to a voltage in each pixel and output these voltages when selected by row and column busses. This marks an important difference. In case of a CCD there is only one amplifier, but there are multiple amplifiers for CMOS. Therefore, CCD sensors are less susceptible to noise, but cannot reach high frame rates. On the other hand, CMOS sensors are well suited for high-speed operation, but noise levels are higher and each pixel needs to be calibrated regularly. The number of frames per second for CCD image sensors is limited to 10 to 15 images per second. CMOS sensors are currently able to capture frames at a rate up to 5 kHz.

Diffraction limited imaging

The seeding particles can be considered as point light sources due to their small sizes. When a point source is imaged by a perfectly aberration-free lens, it does not appear as a point on the image plane. Instead, a Fraunhofer diffraction pattern can be observed, consisting of a central disk (Airy disk) and surrounding circular rings. The diameter of the Airy disk represents the smallest particle image for a given imaging configuration. It is called the diffraction limited spot size d_{diff} and can be found from

$$d_{\text{diff}} = 2.44 f^{\#} (M + 1) \lambda, \quad (3.8)$$

where $f^{\#}$ is the numerical aperture of the imaging lens, M is the image magnification factor defined as the ratio of the image sensor size and the object size, and λ is the wavelength of the scattered light (Raffel et al., 1998). The numerical aperture $f^{\#}$ is defined as the ratio of the focal length f and the aperture diameter D_a for the lens. The diameter of particle image, d_i , can be estimated from:

$$d_i = \sqrt{(M d_p)^2 + d_{\text{diff}}^2}, \quad (3.9)$$

where d_p is the particle diameter (Adrian and Yao, 1985).

For a typical PIV system using a Nd:YAG laser with $\lambda = 532 \text{ nm}$, a numerical aperture of 5.6, and a magnification factor of 0.1, the diffraction limited spot size is $d_{\text{diff}} = 8.0 \mu\text{m}$. The typical size d_p of the tracer particles is in the order of $10 \mu\text{m}$.

Eq. 3.9 then shows that the first term on the right-hand side is much smaller than the second. The particle image size is mainly controlled by d_{diff} and the optical arrangement and the imaging is said to be diffraction limited.

Depth of field

When imaging objects with a camera, the depth of field δ_z defines the portion of a scene that appears sharp in the image. The lens will normally focus at one distance, but the decrease in sharpness is gradual on each side of the focused distance and not visible under normal viewing conditions. The depth of field δ_z is defined by

$$\delta_z = 4(1 + M^{-1})f^{\#2}\lambda. \quad (3.10)$$

As can be seen from this formula, the depth of field is proportional to the square of the numerical aperture. Increasing the camera's aperture leads to an increased volume in which the particles can be observed.

Algorithm

To calculate velocity distributions from the recorded particle image snapshots, the images are subdivided into small regions or interrogation areas. The flow velocity in these interrogation areas is assumed to be uniform, so no image distortion is assumed during the time interval between every two exposures. Each interrogation area in the particle image recording at time t is correlated with the second image at time $t + \Delta t$, as depicted in Fig. 3.6. The cross-correlations are calculated efficiently in Fourier space according to the correlation theorem (Priestley, 1981), using the Fast Fourier Transform (FFT) algorithm. In the first step, both interrogation zones are Fourier transformed. Secondly, the FFT of the first field \hat{I}_1 is multiplied by the complex conjugate of the FFT of the second field \hat{I}_2^* , which is the equivalent of calculating a correlation in real space. An inverse Fourier transform results in the two-dimensional correlation function of the two interrogation zones.

The calculated correlation can be decomposed into three parts: the displacement correlation R_D , the convolution of the mean pixel intensities R_C and a fluctuating noise component R_F . For a typical measured interrogation zone, the cross correlation function is depicted in Fig. 3.7. The peak R_D generated by the displacement of the particle images between the first and the second images is clearly visible above the background of R_C and R_F . The location of the peak with respect to the origin of the correlation function represents the mean in-plane particle displacement vector \vec{x} .

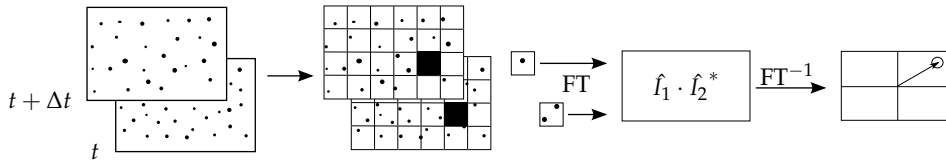


Figure 3.6: Schematic representation of the cross-correlation of interrogation areas (Raffel et al., 1998).

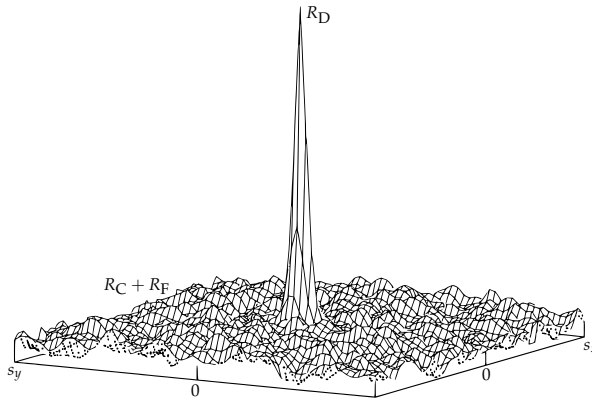


Figure 3.7: Example of a cross-correlation function (Raffel et al., 2007).

The local mean velocity per interrogation area can easily be determined using

$$\vec{u} = \frac{\vec{x}}{\Delta t}, \tag{3.11}$$

where Δt is the time interval between the two images.

Criteria for accurate velocity measurements

The displacement should stand out against the background noise level to make detection possible. The width and the height of the peak depend on the particle image diameter, the number of particles present within the interrogation areas in both images, and the velocity gradient over the interrogation area. In order to obtain a certain level of accuracy while determining the velocity of the interrogation zone, a number of criteria exist regarding the number of particle image pairs and the velocity gradient in the interrogation zone:

- PIV measurements should be performed in such a way that sufficient particles are visible in both the first and the second interrogation area, i.e. one has to

ensure that the correlation is calculated from the same particles in both zones. The particle image density in both areas can be calculated from the particle image concentration in one interrogation area N_I , the fraction of particle images lost due to in-plane displacement, $(1 - F_I)$, and the fraction of images lost by out-of-plane displacement of the particle, $(1 - F_O)$. When no loss of pairs occurs, F_I and F_O will equal one. Keane and Adrian (1992) show that the particle image pair density $N_I F_I F_O$ should exceed 5 to assure a probability of 95% that at least two particle image pairs can be detected.

- To achieve a minimum in-plane loss of particle image pairs, i.e. $F_I \rightarrow 1$, the maximum displacement of the particle image pattern should not exceed a quarter of the interrogation area width:

$$\frac{M|u_{\max}|\Delta t}{d_I} < 0.25, \quad (3.12)$$

where u_{\max} is the maximum in-plane velocity and d_I is the size of an interrogation area.

- Minimising the loss of image pairs due to the out-of-plane displacement, i.e. $1 - F_O \rightarrow 0$ can be achieved satisfying the criterion

$$\frac{|w_{\max}|\Delta t}{\Delta z_0} < 0.25, \quad (3.13)$$

where w_{\max} is the maximum out-of-plane velocity and Δz_0 is the thickness of the light sheet.

- The height and the width of the displacement peak R_D strongly depend on the velocity gradient over the interrogation area (Keane and Adrian, 1990). For strong velocity gradients the peak broadens and becomes less prominent, reducing the probability of detecting the displacement peak from the background noise. This effect is called *detection bias*. To retain sufficient accuracy, the displacement due to changes of the particle velocity in the interrogation area should not be larger than the diameter of the particle image d_i , thus

$$\frac{M\Delta u\Delta t}{d_i} \leq 1, \quad (3.14)$$

where Δu is the velocity difference within the interrogation area due to the velocity gradient.

- Finally, velocity gradients give rise to *gradient bias* since the correlation is biased towards the faster moving particles within the interrogation area. The correlation peak is statistically biased towards velocities that are lower than the average velocity in the interrogation area. This effect can be minimised by satisfying the criterion

$$\frac{M\Delta u\Delta t}{d_I} \leq 0.05. \quad (3.15)$$

Peak detection and displacement estimation

The coordinates of the correlation peak need to be determined by an accurate method to obtain an accurate particle displacement. When one simply takes the coordinates of the highest value in the correlation plane, one would obtain integer coordinates with an uncertainty of ± 0.5 pixels. Due to the statistical nature of the cross-correlation function based on multiple particles, more accurate results can be obtained using additional information from the correlation peaks. The peak value and the spread of the correlation peak enables the determination of the correlation peak maximum with sub-pixel accuracy, in some cases the peak location can be estimated with an 0.05 pixel inaccuracy.

As correlation peaks can be narrow, it is common practice to use only three adjoining values in the mathematical fit of the peak. For the fit function of such three-point estimators, a Gaussian function, $f(x) = C \exp [-(x_0 - x)^2/k]$, is most commonly chosen. The reason is that the particle image, the Airy disk, resembles a Gaussian distribution and the correlation of two Gaussian distributions is Gaussian as well. From the value of the highest correlation value, $R_{i,j}$, and its nearest neighbours, ($R_{i-1,j}$, $R_{i,j-1}$, $R_{i+1,j}$ and $R_{i,j+1}$), the peak location (x_0, y_0) can be estimated:

$$x_0 = i + \frac{\ln R_{i-1,j} - \ln R_{i+1,j}}{2 \ln R_{i-1,j} - 4 \ln R_{i,j} + 2 \ln R_{i+1,j}} \quad (3.16)$$

$$y_0 = j + \frac{\ln R_{i,j-1} - \ln R_{i,j+1}}{2 \ln R_{i,j-1} - 4 \ln R_{i,j} + 2 \ln R_{i,j+1}} \quad (3.17)$$

where x_0 and y_0 are the exact coordinates of the peak, i and j are the integer coordinates of the peak, and $R_{i,j}$ is the value of the correlation function at (i, j) .

The correlation peak should neither be too wide nor be too narrow for accurate estimates of its location. If the size of the particle image is smaller than one pixel, the correlation peak will be very narrow. In this case the three-point estimator introduces a bias error. The obtained displacement vectors will be biased towards integer pixel displacements. A scatter plot of all obtained velocities will clearly show this preferential discrete behaviour, also known as *peak locking*. Changing the aperture or optical system can increase the particle image size to avoid this. As a rule of thumb, best results are obtained when the particle image size d_i is around 2 pixels (Willert, 1996).

Validation

After the full analysis of the PIV images, some obtained velocity vectors are clearly incorrect, as their magnitude and direction strongly deviates from that of their neighbours. These *spurious* vectors often originate from detection failures or result from locally disrespecting the criteria stated in the previous section. Spurious vectors are often encountered in near-wall regions with different light-scattering properties compared to the rest of the flow.

Several statistical methods exist to detect and remove spurious vectors. Detailed descriptions can be found in Westerweel (1994) and Westerweel and Scarano (2005). Besides a minimum correlation filter, a peak height filter and a signal-to-noise filter, the local median technique is most commonly used (Raffel et al., 2007). For each obtained displacement vector the median is calculated for an area of 3×3 or 5×5 pixels around the central vector. The difference between the median vector and the central vector should not exceed a certain preset value:

$$\|\vec{u}_{i,j} - \vec{u}_{\text{surr}(i,j)}\| < \alpha \sigma_{\text{surr}(i,j)}, \quad (3.18)$$

where $\vec{u}_{i,j}$ denotes the velocity vector at position (i, j) in the $n \times n$ neighbourhood, $\vec{u}_{\text{surr}(i,j)}$ is the median of the vectors surrounding the central vector, $\sigma_{\text{surr}(i,j)}$ is the standard deviation of the magnitudes of all vectors within the search area and α an extra parameter to set the stringency of the validation.

Adaptive cross-correlation and grid refinement

The small, discrete number of particle images and the discretisation of an image in interrogation zones introduce systematical measurement noise in the velocity results of PIV measurements. Westerweel et al. (1997) showed that this systematical error is nearly independent of the displacement, except for small displacements in the order of 0.5 pixel where it is directly proportional to the displacement.

The above relation between measurement error and displacement can be used to improve the PIV results in a multi-pass approach. First, a normal cross-correlation is calculated, spurious vectors are detected, removed and replaced by interpolated vectors. In a second phase, the procedure is repeated, where the interrogation area of the second image has been shifted relative to the first area by the earlier calculated displacement. This reduces the in-plane loss, $F_1 \rightarrow 1$, and more particle image pairs will be found. This procedure can be performed multiple times to let the calculated correlation peak converge. The residual displacement will decrease to values between ± 0.5 pixels, which ensures a low measurement error.

Westerweel et al. (1997) demonstrate that the signal-to-noise ratio (SNR) becomes independent from the displacement for low turbulent flows and the SNR improves significantly for high turbulent flows. Moreover, with such adaptive cross-correlations, the dynamic range of the PIV technique with such adaptive cross-correlations increases as the maximum measurable velocity is not confined to the size of a single interrogation area.

Another advantage of a multi-pass interrogation approach is the possibility to decrease the size of the successive interrogation areas, which proves to be especially useful when a wide range of displacements are present in the observed flow. As mentioned above, the interrogation window offsets between the first and second image decrease per additional adaptive cross-correlation, allowing for smaller size interrogation windows. Without the window offsetting, standard evaluation schemes would lose the correlation signal due to the larger displacement. The whole procedure can be repeated several times with smaller interrogation areas. The grid refining method or *Window Displacement Iterative Multi-grid* (WIDIM) method is described in detail by Scarano and Riethmuller (1999, 2000).

3.3 Liquid crystal thermography

The liquid crystal state is an intermediate state of matter in between the isotropic liquid state and the crystalline solid state. Liquid crystals have the mechanical properties of fluids, like viscosity or surface tension, but they have the optical properties of solids, like birefringence and anisotropy. Many types of liquid crystals are known, some primarily sensitive to pressure, others to shear, electromagnetic fields or temperatures. The latter are called thermochromic liquid crystals. When they are illuminated with white light, they reflect a specific dominant wavelength depending on their temperature and can thus be used as temperature indicators.

Liquid crystal thermography (LCT) has been mainly used for visualisation and for surface temperature measurements, either by spraying a thin layer of liquid crystals onto the investigated objects or by applying self-adhesive coated liquid crystal sheets.

The first applications of LCT in fluids were mainly qualitative visualisations (Zocchi et al., 1990; Moffat, 1990) and quantitative surface temperature measurements (e.g. Theerthan and Arakeri, 1998, 2000). Since the introduction of digital image processing, the technique was explored further for non-intrusive temperature measurements in a flow (Dabiri and Gharib, 1996).

As PIV and LCT both employ small tracer particles, combined PIV-LCT techniques obtaining simultaneous velocity and temperature data were studied by Hiller and

Kowalewski (1986); Hiller et al. (1989, 1993). Later, the technique was employed and extended for various applications by Kowalewski and Stasiek (1998); Kowalewski (1999); Sabatino et al. (2000); Park et al. (2001); Praisner et al. (2001); Stasiek and Kowalewski (2002); Pottebaum and Gharib (2004); Funatani et al. (2004). More recent, scanning (tomographic) techniques for measuring temperature and velocity simultaneously in three dimensions have been presented by (Fujisawa and Hashizume, 2001; Lutjen et al., 2001; Ciofalo et al., 2003; Fujisawa et al., 2005).

In the present section, a brief presentation will follow on the liquid crystal properties and the calibration and measurement procedures will be explained. For more information on liquid crystals in general the reader is referred to Khoo (1995); Collings and Patel (1997). Dabiri (2009) presents an extensive review on the application for thermochromic liquid crystals in fluids.

3.3.1 Thermochromic liquid crystals

Based on their optical behaviour and molecular structure, liquid crystal structures are commonly categorised into three groups: smectic, nematic and cholesteric. The latter is named after cholesterol, the first material found to have the ability to change colour. Currently, non-sterol liquid crystals have been developed which are named chiral nematic referring to their nematic molecular structure. Confusingly, both the non-sterol as the sterol types are called cholesteric, even though their physical and chemical properties are quite different. In Fig. 3.8 a typical molecular structure of a non-sterol thermochromic liquid crystal (TLC) is depicted. The H_mC_n group in the molecule is a long straight chain alkyl group, which makes the molecule long and rigid. The chiral point is the central C-atom of the tetraeder. If this material is illuminated with vertically polarised light on one side, it will reflect horizontally polarised light on the other side, which can be left polarised or right polarised, depending on the ordering of the groups around the C-atom.

Figure 3.9 depicts the structural change of liquid crystals as temperature increases. In the solid state liquid crystals are organised in a three-dimensional ordered structure, like any other crystalline solid. Upon melting the molecules will organise in layers, perpendicular to the long molecule axes. Within these layers the molecules are mobile in two directions. As temperature increases, the molecules will enter the nematic state, where the layered structure disappears and the molecules can move in three directions.

Optical active materials that form a nematic state, will form a chiral or twisted structure. The preferred direction of the long axes of the molecules, the molecular director \vec{r} , is no longer constant. The structure is made of thin layers of molecules stacked on top of each other. The molecules in the nematic layers are not symmetric with re-

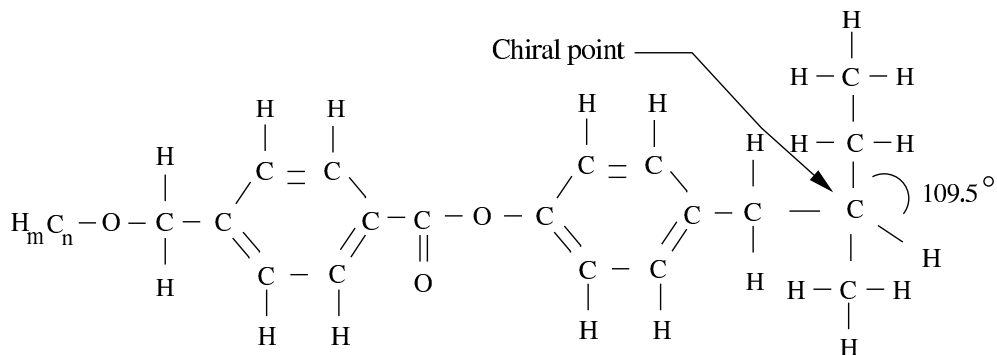


Figure 3.8: A typical chiral nematic molecule, (2-methyl-butyl)phenyl 4-alkyl(boxy)benzoate molecule.

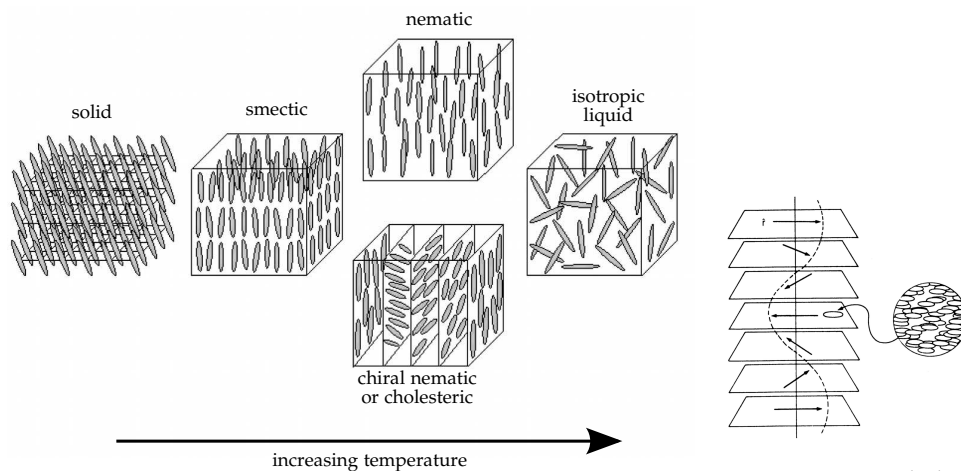


Figure 3.9: Liquid crystal structure for increasing temperature.

Figure 3.10: Cholesteric liquid crystal.

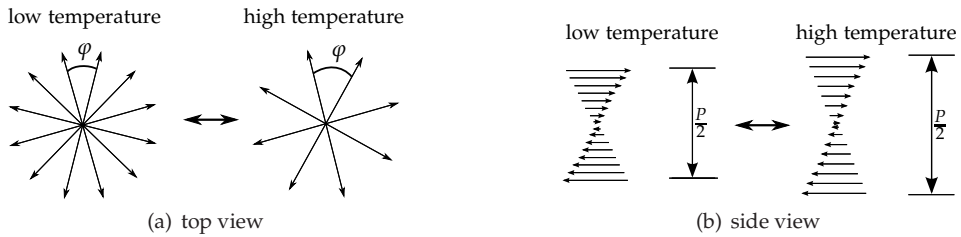


Figure 3.11: Two possible effects on the pitch P with rising temperature. (a): increasing displacement angle φ between the layers (Parsley, 1991). (b) increasing distance between nematic layers.

spect to their long axis, as the side group of the molecule extend out of the flat layer of the molecule. This asymmetry causes molecular forces to twist each nematic layer a little. Therefore, the director \vec{r} is rotated from layer to layer, forming a helical structure as depicted in Fig. 3.10.

The helix aggregates of molecules are responsible for the optical activity of the chiral nematic structure. The helical structure is characterised by two parameters, the pitch P and the displacement angle φ , indicated in Fig. 3.11. The pitch is defined as the longitudinal distance the director \vec{r} spans to make a complete revolution, clockwise or counterclockwise. The helix can be left- and right-handed. The displacement angle φ describes the rotation of adjacent nematic layers.

The pitch of the helices determines the wavelength of the reflected light. As temperature increases, the thermal motion of the molecules also increases which results in a change in molar volume and could affect the helical structure in two opposing ways. First, the distance between adjacent layers increases, resulting in a larger pitch and reflected wavelength, see Fig. 3.11(a). However, the displacement angle φ of the molecule will increase as well, resulting in a smaller pitch and decreasing wavelength as depicted in Fig. 3.11(b). In general, and for the liquid crystals used in this work, the latter effect dominates, resulting in a red appearance at low temperatures and a blue appearance at high temperatures.

Optical properties

Due to the anisotropic structure of the nematic and smectic phase, a light wave travels faster in a direction parallel to the layers than in a direction orthogonal to the layers. However, the anisotropy in the cholesteric phase results in a faster light propagation orthogonal to the layers compared to light in the parallel direction. Due to these different light propagation speeds, different refraction indices can be defined

for the polarisations perpendicular, n_o , and parallel, n_p to the director \vec{r} . The different refraction indices define the magnitude indicate of birefringence $\Delta n = n_o - n_p$, which is known to be strong for liquid crystals (Hecht, 1998; Dabiri, 2009).

Circular dichroism

For the cholesteric phase the helical structure introduces an extra effect on the optical properties. When illuminated with nonpolarised light, the birefringent behaviour results in two circularly polarised light components, one to the left and one to the right. The component that propagates in the same direction as the helix would not show any variation in refractive index. The other will experience a sinusoidal variation in the refractive index at every half pitch length $P/2$. This causes the circularly polarised light to be scattered when $\lambda_1 = n_p P$ for the parallel direction and $\lambda_2 = n_o P$ for the orthogonal polarisation. Thus, when unpolarised light illuminates chiral nematic liquid crystal structure, all wavelengths between λ_1 and λ_2 will be reflected, while the others will be completely transmitted. A reflection bandwidth $\Delta\lambda$ can be related to the birefringence: $\Delta\lambda = P(n_p - n_o) = P\Delta n$.

Bragg scattering for liquid crystal layers

For liquid crystals, as for every crystalline solid, Bragg scattering can appear. Given a distance d between parallel planes of the helix and an incident angle Θ , incident light scatters according to the Bragg Law (Kittel, 1996)

$$2d \sin \Theta = m\lambda, \quad (3.19)$$

with m an integer value. For the chiral nematic crystal phase, the helical structures act as a three-dimensional grating with periodicity $P/2$. Furthermore, one has to compensate for the change of refraction index for light entering a chiral nematic liquid crystal. This has been done by introducing the mean refractive index \bar{n} which changes Eq. 3.19 into (Ferguson, 1968)

$$P\bar{n} \cos \Theta = \lambda_0, \quad (3.20)$$

where λ_0 denotes the wavelength of selectively reflected light. The Bragg scattering on a chiral nematic liquid is illustrated in Fig. 3.12.

Eq. 3.20 is a rather simplistic representation of the optical response, as it relates only a single wavelength for given values of P , \bar{n} and Θ . In reality, a narrow band of wavelengths $\Delta\lambda$ is reflected, which strongly depends on the wavelengths of the illumination source, the illumination angle and the viewing angle. Moreover, the alignment of the helical structures in the liquid crystal is crucial: the liquid crystal layer should be a uniformly aligned planar structure as this will exhibit optimal reflection.

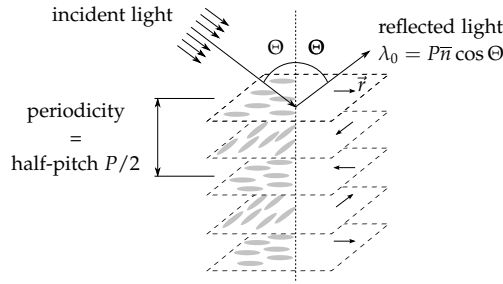


Figure 3.12: Schematic of Bragg scattering in liquid crystals.

Elser and Ennulat (1976) extended 3.20 to a more realistic relation:

$$\lambda_p = \lambda_n \cos \frac{1}{2} \left[\sin^{-1} \frac{\sin \Theta_i}{\bar{n}} + \sin^{-1} \frac{\sin \Theta_v}{\bar{n}} \right]. \quad (3.21)$$

This equation describes, based on simple geometrical considerations and assuming a mean refractive index \bar{n} , the relation between the obtained peak wavelength λ_p as a function of the illumination angle Θ_i , viewing angle Θ_v and the wavelength λ_n . The wavelength λ_n denotes the peak wavelength obtained from light travelling along the helical axis, i.e. where $\Theta_i = \Theta_v = 0$: $\lambda_n = P\bar{n}$.

Bragg scattering for liquid crystal capsules

Encapsulated liquid crystals, as described in Sect. 3.3.1, commonly have a lower reflectance than continuous liquid crystal films of the same thickness as only a small part of the particle is within the optimum angle for reflection (Elser and Ennulat, 1976). Considering an angle Θ_t between illumination and observer, defined by $\Theta_t = \Theta_i + \Theta_v$. The optimal reflection will occur at $\Theta_i = \Theta_v = \Theta_t/2$. This wavelength will dominate all other wavelengths reflected by the crystal and fully determines the reflected (and thus observed) colour. Since the mean refraction is relatively small ($\bar{n} \approx 1.5$), substitution of $\Theta_i = \Theta_v = \Theta$ in Eq. 3.21 leads to a relation similar to Eq. 3.20 except for a minor angle dependent factor:

$$\lambda = f_n(\Theta) P\bar{n} \cos \Theta. \quad (3.22)$$

Therefore, in practice changes in illumination and observation angles will be characterised by a change in Θ , which further on will be called the viewing angle.

Encapsulation

Liquid crystal material is very sensitive to aging, chemical reactants, ultra violet light and mechanical stress. For practical use, a layer of liquid crystals can be placed between a thin sheet of transparent polyester and black coloured sheet. The obtained stack of sheets could be used to measure surface temperatures. Another method is encapsulation of liquid crystals in a protective layer. This coacervation process involves the addition of gelatin and gum arabic to a suspension of the liquid crystal in water at a certain pH level and elevated temperature. Reducing the temperature again and changing the pH leads to a reaction which eventually leads to a protective shell around the liquid crystal. The nearly spherical liquid crystal micro-capsules formed in this process have diameters varying between 10 μm and 50 μm . They can be employed in a sprayable paint to cover (complex) surfaces, or as temperature tracers in a fluid (Parsley, 1991).

Responsiveness

To use an encapsulated LC particle as temperature sensor in a fluid, the response time to a temperature change should be quantified. It depends on the rate of change of the LC pitch and the thickness of the encapsulation layer, and the coating layer for a liquid crystal sheet. There is still a debate on the typical response time of the LC material. Ferguson (1968) found the time response for cholesteric liquid crystals to be in the order of (20 to 100) ms. Nematic crystals are considered to be much faster. Ireland and Jones (1987) showed experimentally that the response time for 10 μm chiral nematic liquid crystal capsules is in the order of 3 ms. A study of the thermal properties of a 150 μm liquid crystal by Dabiri and Gharib (1996) resulted in a response time of 60 ms. Kobayashi and Saga (1998) found the response time for chiral nematic liquid crystals to be 150 ms. Based on the experimental results of Ireland and Jones (1987) and Dabiri and Gharib (1996), it is expected that the micro capsules have a response time in the order of ten milliseconds.

Liquid crystal sheets are protected in same way by a thin layer of acetate or polyester film. The main advantage is that the layer thickness is constant and the surface is perfectly smooth. Nonetheless, the thickness of the stack of sheets is in the order of 100 μm . This creates an extra thermal inertia of the sheet and the sheets exhibit a greater dependence on the viewing angle (Kasagi et al., 2001).

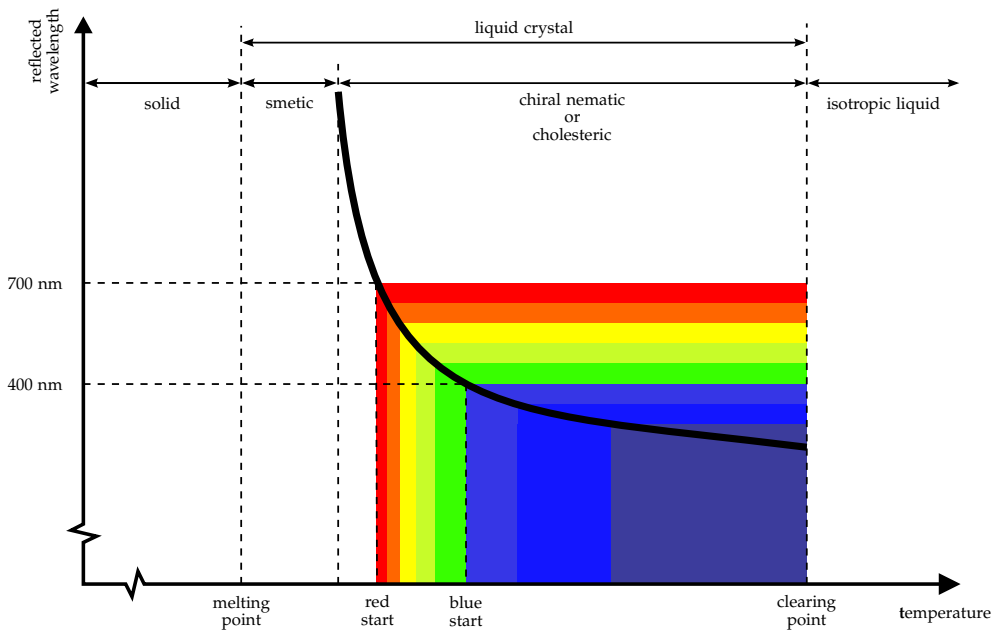


Figure 3.13: Qualitative liquid crystal response to temperature. Reflected wavelength as function of temperature for a temperature sensitive liquid crystals mixture, after Stasiek (1997).

3.3.2 Temperature-colour correlation

In Fig. 3.13 the reflected wavelength as a function of temperature is depicted for a liquid crystal illuminated with white light. At a certain temperature, the *red start*, the crystals enter their cholesteric state and will reflect a red colour. The red start temperature is the lower limit of the measurable temperature range, the colour play. The upper limit is marked by the *blue start* marking the temperature at which the crystals turn blue. Increasing the temperature above the *clearing point* will eventually change the crystals to the isotropic liquid phase where no reflection will occur (Roberts and East, 1996; Stasiek, 1997).

In early day liquid crystal research, isotherms were studied using mixtures of narrow-band liquid crystals with different red start temperatures. Later on, wide-band crystals were more frequently used. For example, Akino et al. (1989) used 18 optical filters and a black-and-white camera to generate a temperature distribution from discrete monochromatic regions. This isotherm approach resulted in a low resolution and a small number of discrete temperatures. Nowadays, these drawbacks have been set aside using full-colour imaging equipment by which a more continuous distribution is obtained.

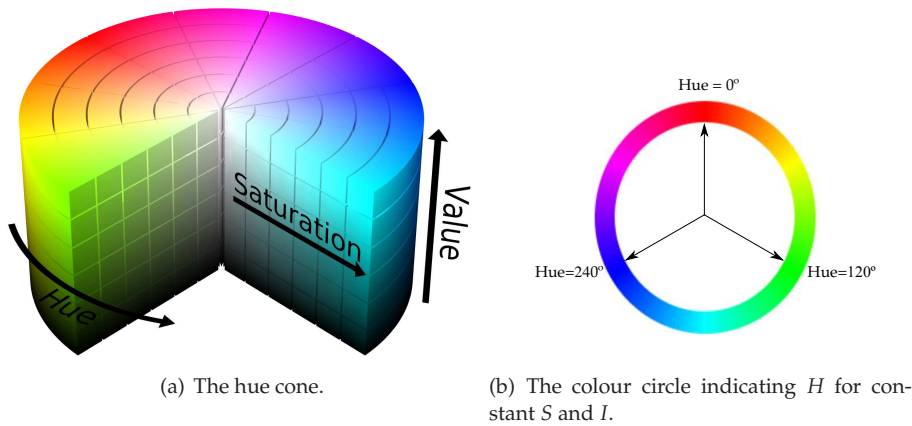


Figure 3.14: The HSI colour space.

To determine absolute temperature information from liquid crystals, a method is necessary by which different colours can be quantified. An obvious choice to quantify a colour would be to decompose it in the primary colours. This decomposition is not a fundamental property of light, but merely related to the physiological response of the human eye to incident light. The International Commission on Illumination defined a standard colour space in 1931 based on three monochromatic primary colours: blue/violet ($\lambda = 436$ nm), green ($\lambda = 546$ nm) and red ($\lambda = 700$ nm) (Travis, 1990). Most electronic devices for colour imaging decompose the perceived colours in three signals Q_1 , Q_2 and Q_3 using a so-called trichromatic decomposition (Hay and Hollingsworth, 1996; Travis, 1990). The obtained *tristimulus* or *triplet* signals are often the above described primary colours.

There are several ways to associate temperature with these three values. The simplest one would be a linear combination:

$$T = \alpha_1 Q_1 + \alpha_2 Q_2 + \alpha_3 Q_3 + \beta. \quad (3.23)$$

As the distribution of the RGB triplet is not linear with temperature, this linear combination does not give satisfactory results (Hay and Hollingsworth, 1996). A common way to relate the triplet to temperature is to transform the RGB colour space to a perceptual colour space, the HSI (or HSV) colour space. The axes in this colour space stand for *hue* (H), *saturation* (S) and *intensity* (I). The latter component is sometimes called *value* (V).

Figure 3.14(a) illustrates the HSI colour space as a cone. The intensity is the brightness of the colour. It ranges from the origin (black, where $R = G = B = 0$), along the axis of the cone to the maximum values of R , G and B (white). The saturation identifies the purity of the perceived colour and can be interpreted as the distance

from the centre axis of the cone. The hue indicates the dominant wavelength of the colour. It is defined as the angle with respect to the line between the cone axis and the maximum red value. Each colour can be transformed to a unique hue value in the range of 0° to 360° . Somewhat arbitrarily, a hue of 0° corresponds to red, 120° corresponds to green and 240° corresponds to blue. For each combination of S and I there is a similar colour circle as depicted in Fig. 3.14(b).

As hue and HSV colour space are perceptual concepts, several definitions exist. Hay and Hollingsworth (1996, 1998) compared a number of commonly used definitions for HSV and concluded that the lowest average uncertainty is obtained using

$$H = \arctan \left(\frac{\sqrt{3}(G - B)}{2R - G - B} \right). \quad (3.24)$$

As the arctangent can be numerically demanding, a nearly equivalent calculation procedure is used in the present work to transform from RGB to HSV colour spaces. The complete set of equations is indicated below:

$$S = \frac{\max(R, G, B) - \min(R, G, B)}{\max(R, G, B)} \quad (3.25)$$

$$I = \frac{R + G + B}{3} \quad (3.26)$$

$$H = -1 \quad \text{if } S = 0$$

$$h = \frac{G - B}{\max(R, G, B) - \min(R, G, B)} \quad \text{if } \max(R, G, B) = R$$

$$h = 2 + \frac{B - R}{\max(R, G, B) - \min(R, G, B)} \quad \text{if } \max(R, G, B) = G$$

$$h = 4 + \frac{R - G}{\max(R, G, B) - \min(R, G, B)} \quad \text{if } \max(R, G, B) = B$$

$$H = 60 h \quad \text{if } h > 0$$

$$H = 60 h + 360 \quad \text{if } h < 0. \quad (3.27)$$

Anderson and Baughn (2004) compared Eq. 3.24 against the set of equations in 3.27 and found a maximum hue difference of about 0.003 on a unity hue scale. As this difference is negligible compared to the typical hue standard deviations in the measurements, both methods are practically equivalent.

3.3.3 Illumination and imaging

It is important to carefully select the illumination source as liquid crystals are strongly dependent on the incident light. Preferably the illumination provides a light of constant intensity and a complete white spectrum during calibration and measurements. In-situ calibrations, performing calibrations and measurements in the same configuration, are preferred as they avoid variations in viewing angles, background noise, reflections and layer thickness. The white balance, a constant ratio for the three values of the RGB triplet, could be used to enhance the images. This corresponds, as Sun et al. (1997); Witte (2006) report, to a change in calibration curves. However, in practice, the white balance does not play an important role when the same camera settings are applied in calibration and measurement situations (Witte, 2006).

3.3.4 Bayer filtering

Digital image acquisition systems use colour CCD cameras to provide fast acquisition and storage of image data. The individual colours are decomposed by colour filters mounted on the CCD arrays of the camera. Colour CCD cameras are manufactured with one or three CCD chips. In the 3CCD camera, incoming light which passes the lens is split by a trichroic prism assembly. The red, green and blue wavelength are separated and three different CCDs are exposed with three different colours. The single chip CCD is a cheaper alternative and employs a pixel based colour filter, see Fig. 3.15(a). To have a square layout, there are twice as many green pixels as red and blue pixels. To obtain colour information from this so-called Bayer-filtered CCD, virtual pixels are created from one red, two green and one blue pixel, as depicted in Fig. 3.15(a). In this way the resolution is decreased by a factor two in both directions. An important disadvantage of this filter is the occurrence of colour aliasing. In Fig. 3.16 a white stripe with a width of 3 (virtual) pixels on a black background is exposed on a Bayer filter. The right side of the image shows the resulting colours. Not only the colours are affected, also the hue algorithm could not be used as the hue values of certain virtual pixels are undefined due to invalid RGB combinations.

A Bayer interpolation filter can be applied to obtain more spatial information from a Bayer filtered image. For each R , G or B pixel, the two unknown colour values are interpolated from the neighbouring pixels, as depicted in Fig. 3.15(b). This results in an $((W - 1) \times (H - 1))$ pixels RGB image with nearly the same resolution as the original Bayer image ($W \times H$ pixels). However, the resulting colour information of the Bayer interpolated images is not fully uncorrelated in contrast to an image obtained with a 3CCD camera. These images are preferably not used for second-order statistics of hue or temperature (Witte, 2006).

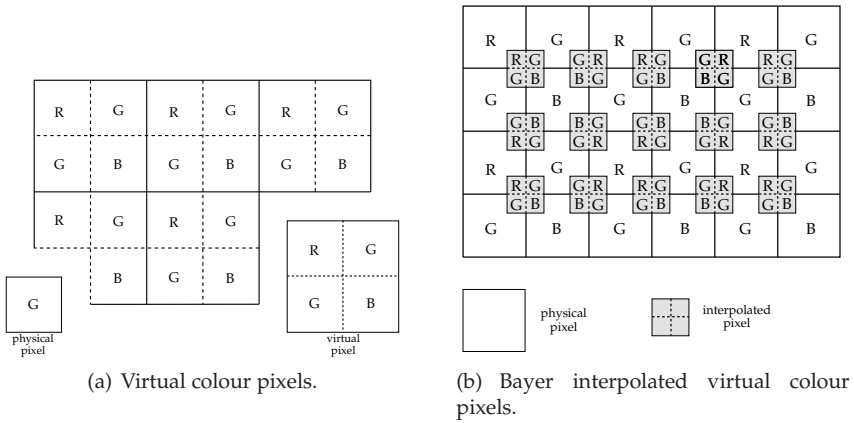


Figure 3.15: Colour signal reconstruction for single CCD cameras.

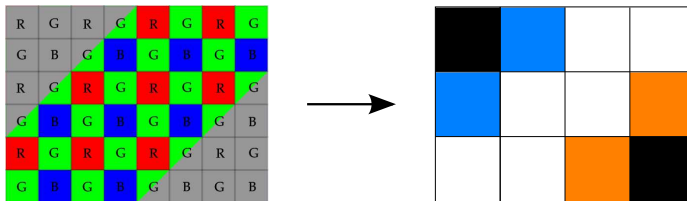


Figure 3.16: Colour aliasing effect due to the Bayer filter.

3.3.5 Image processing

In Witte (2006) an extensive study has been reported on the optimisations for performing liquid crystals measurements in the present set-up. The main conclusions for optimal results from converting raw liquid image data to HSV data, and finally to temperature, include:

- Applying an intensity filter to remove low intensity image information which could negatively affect the hue results;
- Applying a saturation filter to distinguish between image data from particles and background information, which enhances the overall result;
- Subtracting of the background illumination in order to improve the signal-to-noise ratio. This will affect the hue range, which is enlarged considerably and the standard deviations in the hue results will decrease as well.

The reader is referred to Wiberg and Lior (2005); Dabiri (2009) for more information on error reduction and increasing the accuracy of the quantitative results.

3.3.6 Calibration

In order to derive quantitative temperature information from liquid crystals images, a hue-temperature relationship needs to be established. Usually such calibrations could be performed by acquiring liquid crystal images at constant, known temperatures. However, even in that case, the liquid crystal colours are not uniformly distributed due the viewing angle dependencies. Sabatino et al. (2000) proposed a point-wise or local calibration technique where hue and temperature are calibrated for each position in the area of view. Instead of one relation, for each pixel in the image there would exist a different calibration curve. Moreover, they report on additional advantages of this techniques.

- It requires no assumptions concerning the isolation and removal of reflective components of the lighting.
- It inherently compensates for noise or defects in the background signal.
- It allows calibration of test surfaces with significant lighting and viewing angle variations.

Employing a point-wise calibration results in a large database of hue values per temperature and per pixel. When the temperature intervals during calibration are small,

each temperature could be assigned a hue value by interpolation of the data, using a linear or spline interpolation function.

One could reduce the curve data by fitting it to polynomial curve of arbitrary order (Behle et al., 1996; Hay and Hollingsworth, 1998). However, the choice of the order of the polynomial is subjective and can only be determined empirically. More recently, the calibration curves are constructed using neural networks (e.g. Park et al., 2001; Grewal et al., 2006). See Dabiri (2009) for more information.

For suspended liquid measurements, as Hekker (2003) and Witte (2006) report, there are gaps in the hue data from the acquired liquid crystal images. The concentration of liquid crystal particles could not be further increased as light would then not be uniformly distributed in the convection cell. Witte (2006) used a combination of pixels of an image, a so-called zone, to extract the calibration curves locally. This *zone-wise* calibration has been used in the present work.

Another approach to reduce viewing angle effects could be using different optics. Günther and Rudolf von Rohr (2002b,a); Kruse and Rudolf von Rohr (2006) use telecentric lenses to ensure the observer looks at a constant viewing angle at an object plane.

Colour play and hysteresis

When liquid crystal material is heated to temperatures above their clearing point, its reflectivity decreases and a shift occurs in the hue-temperature calibration towards higher hue values. Anderson and Baughn (2004) investigated this hysteresis behaviour for five types of liquid crystals and concluded that the hysteresis is significant, up to 60 % bias for small-banded TLCs. Therefore it is important to adjust the maximum and minimum temperatures to remain within the colour play of the LC material. Cooling the LC material below the red start will shift the calibration curve back to its original position (Baughn et al., 1999).

4

Experimental apparatus

This chapter discusses the experimental rig that was used for temperature and velocity measurements in thermal convective situations, electromagnetically forced flows and combinations of both. All experiments reported in this thesis are performed in a rectangular glass cell with a $4 \times 4 \times 1$ ($W \times W \times H$) aspect ratio. Section 4.1 describes this experimental facility and the parameters for the thermal convection experiments. Section 4.2 explains the measurements with PIV, LDA and thermochromic liquid crystals. Finally, Section 4.3 discusses the adjustments made for incorporating an electromagnetic field on the flow.

4.1 Experimental set-up

4.1.1 Convection cell

The experimental set-up is depicted in Figure 4.1. It consists of a $600 \times 600 \times 155 \text{ mm}^3$ cell in which tap water or water-like solutions can be subjected to electromagnetic fields and to different temperatures.

Throughout this work, a coordinate system is used which originates at the centre of the lower copper plate as indicated in Fig. 4.1. Therefore, the measurement domain is spanned by $-0.5W < x < 0.5W$, $-0.5W < y < 0.5W$ and $0 < z < H$, where W is the cell's width and H is the cell's height.

The top and bottom walls of the cells are two copper plate stacks. Each stack consists of two 3 mm thick flat copper plates, with 3 mm high, small copper spacers in between, to create a hollow cavity in which a cooling/heating fluid can be brought into the stack, see Fig. 4.2. In this way, the plate stacks can be kept at a constant temper-

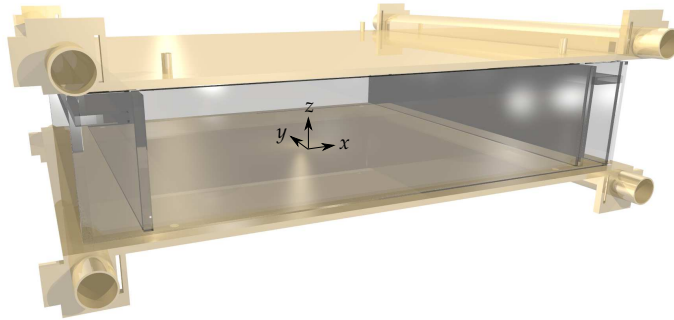


Figure 4.1: The Rayleigh-Bénard convection cell.

ature. Copper is chosen for construction because of its relatively high specific heat constant. Furthermore, as it is a non-ferro metal, it can be used in the neighbourhood of strong magnetic fields.

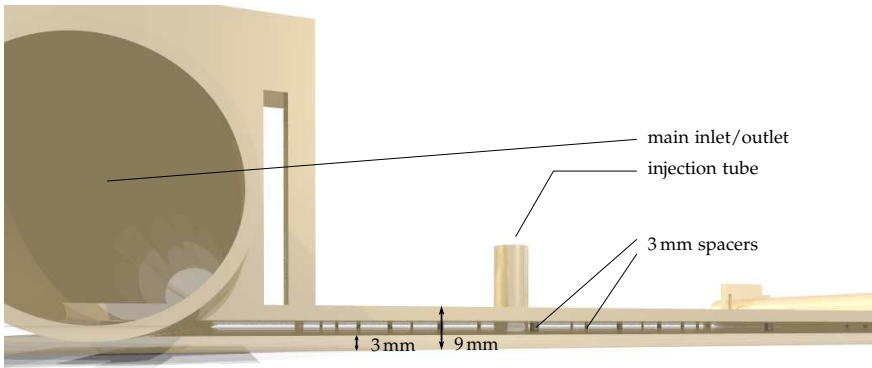
The hot and cold water in- and outlets are connected with PVC piping to 300l basins in which water can be temperature controlled within a range of $0.02\text{ }^{\circ}\text{C}$. To prevent heat losses by transporting the water through the system, the hoses and the outer sides of the plate stacks are insulated. The water is transported through the system by two pumps connected to the outlets of the respective plate stacks. The pumps suck the fluid through the plate stacks and thus create a pressure drop within the plate stacks, which ensure the mechanical stability and flatness of the plate stacks. Moreover, the pumps dissipate heat so that they should not be placed at the inlet of the plate stacks. Using two three-way valves the cooling and heating circuits can be independently switched to the top or bottom plate stack, which is useful for setting starting conditions or performing calibrations.

To allow insertion of tracer particles, four injection tubes are constructed in the plate stacks as can be seen in Fig. 4.2.

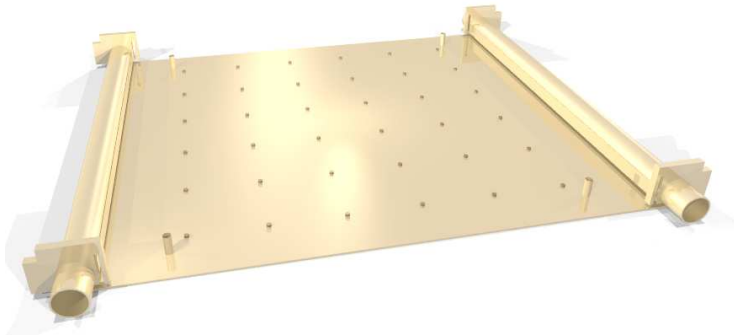
4.1.2 Working fluid

For each convection experiment the cell has been filled with degassed tap water. The use of degassed water is essential to prevent bubble formation at the walls. During long term experiments coalescent gas bubbles in the water could form larger bubbles which offset the heat transfer at certain locations of the convection cell.

For the electromagnetic experiments the electrical conductivity of the fluid had to be



(a) Detailed view.



(b) Inside view.

Figure 4.2: The composition of the warming and cooling plates. (a) shows the plate stack with both 3 mm copper slides. In (b) the top massive plate is removed to view the position of the placeholders.

thermal diffusion coefficient κ	$0.141 \times 10^{-6} \text{ m}^2 \text{ s}^{-1}$
thermal expansion coefficient α	$0.147 \times 10^{-3} \text{ K}^{-1}$
density ρ	999.13 kg m^{-3}
kinematic viscosity ν	$1.156 \times 10^{-6} \text{ m}^2 \text{ s}^{-1}$
thermal conductivity λ	$0.585 \text{ W m}^{-1} \text{ K}^{-1}$
specific heat c_p	$4.194 \times 10^3 \text{ J kg}^{-1} \text{ K}^{-1}$

Table 4.1: Fluid properties of water at $T = 15^\circ\text{C}$ and $p = 1.0 \times 10^5 \text{ Pa}$ (Janssen and Warmoeskerken, 1997; Lide, 2006)

enhanced by adding salt, see Sect. 4.3.1. Relevant properties of water at a working temperature $T = 15^\circ\text{C}$ at pressure of $p = 1.0 \times 10^5 \text{ Pa}$ are given in Table 4.1 for details.

As optical measuring techniques are used, pollution by dust particles or other impurities of the working fluid water must be prevented.

4.1.3 Temperature monitoring

The temperature in the large basins, the transporting system as well as the Rayleigh-Bénard cell are continuously monitored by Copper-Constantan thermocouples. Each thermocouple wire has its cold end in a melting-ice bath for cold-junction compensation, see also Arts and Charbonnier (1994). The microvoltages between both thermocouple wires due to the Seebeck effect are measured by HP3497A data acquisition devices, which in turn transferred the data to an in-house coded software application for data storage. All thermocouples are calibrated using a Pt-100 thermistor probe (Systemtechnik AB, S1320) with an accuracy of 0.01 K. Due to relay circuits in the HP3497A device, the sample rate was relatively low, 0.3 Hz, which was sufficient for monitoring the system. By bypassing the relay in case of a single thermocouple per acquisition device, a sampling rate of 20 Hz could be reached.

For monitoring the cooling and heating circuit, four thermocouples are placed in the each water basin. Two thermocouples are placed in both the inlet and outlet of the plate stack. In the plate stack eight additional thermocouples are mounted to measure the temperature of the copper plate that is in contact with the working fluid. In this way the temperature gradients over the plate stacks and the temperatures in the heating and cooling circuits could be monitoring accurately. The large water basins could be regarded as constant in temperature with an inaccuracy of 0.02 K.

The temperature of the working fluid inside the convection cell was monitored as well. In each corner of the cell a series of six thermocouples were mounted to meas-

ure local temperatures. Each series has thermocouples at the same vertical position: $z/H = 0.03, z/H = 0.10, z/H = 0.33, z/H = 0.67, z/H = 0.90$ and $z/H = 0.97$.

4.1.4 Required water flow through plate stacks

Water flow rates through the plate stacks have to be sufficiently high for the water temperature difference between the inlet and the outlet of the plate stack to remain within an arbitrarily chosen maximum temperature difference δT of 0.1°C . Assuming an average temperature difference ΔT between top and bottom plate of approximately 10K during experiments, the required flow rate can be calculated from the Nusselt scaling laws. Using Eq. 2.37 and Table 4.1, the required heat flux for the a typical case of $Ra = 3 \times 10^8$, $\Delta T = 10\text{K}$ is $q'' = 1.8 \times 10^3\text{W m}^{-2}$. The plate covers an area of $(0.60)^2 = 0.36\text{m}^2$, leading to a required power $P = 1.1 \times 10^3\text{W}$ to be delivered by the cooling and heating circuits. This power is related to the volumetric flow rate Q of the water passing through the plate stacks and the temperature difference δT between inlets and outlets:

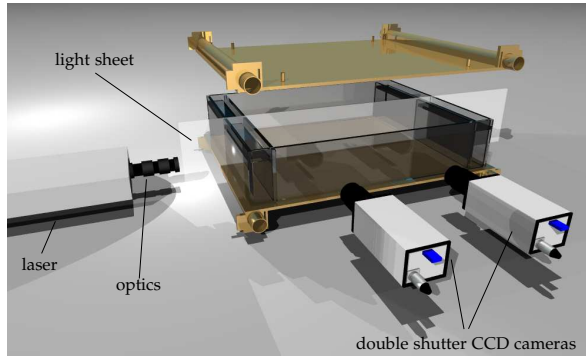
$$P = \rho c_p Q \delta T. \quad (4.1)$$

For the abovementioned power and a temperature difference $\delta T = 0.1\text{K}$, the volumetric flow Q through the system should be $Q = 1.1 \times 10^2\text{l min}^{-1}$ to transport the required amount of heat. As the pumps in the cooling and heating system deliver a constant flow rate around $2 \times 10^2\text{l min}^{-1}$, the requirement $\delta T < 0.1\text{K}$ is fulfilled for all experiments. Moreover, the plate's internal thermocouples showed that the actual temperature deviation over the plate was much smaller than 0.1K during the performed experiments.

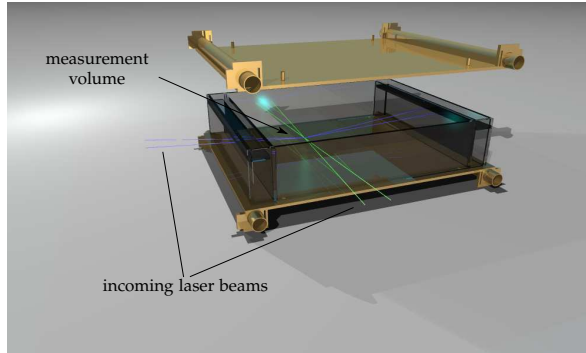
4.2 Measurements

4.2.1 PIV measurements

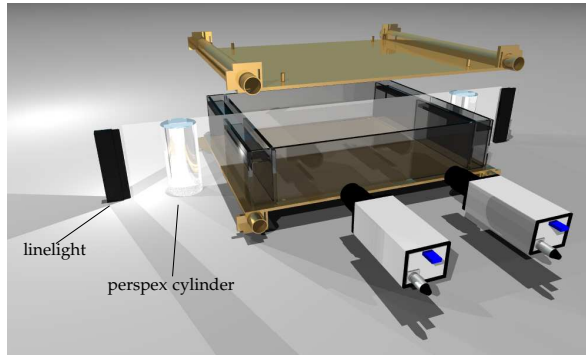
The PIV system included a double pulsed Continuum Minilite Nd:YAG laser with a pulse energy of 25mJ , manufactured by Optical Flow Systems Ltd./ILA GmbH. A laser light sheet was constructed by a lens system attached to the laser, which was capable of producing a sheet with a waist of 1mm . Depending on the arrangement, one or two PCO Double-Shutter Sencam CCD cameras with a resolution of 1280×1024 pixels were used to record images of the seeding particles in the laser sheet. The CCD sensor in the cameras is actively cooled to reduce thermal noise. Image analysis was done using the commercial software VidPIV 4. The fluid was



(a) Details of the PIV set-up.



(b) Details of the LDA set-up.



(c) Details of the LCT set-up.

Figure 4.3: Sketches of the experimental set-up for the different types of measurements.

seeded with Potters-Ballotini hollow glass spheres which were selected to be naturally buoyant in the investigated fluids. Their sizes varied between approximately $10\ \mu\text{m}$ and $20\ \mu\text{m}$.

For the PIV measurements the camera was equipped with a 55 mm focal length lens and a numerical aperture of 2.8 – 5.4, depending on the light conditions. For a full width PIV field, two cameras are used each equipped with 28 mm focal length lenses. The time separation between the subsequent laser pulses ranged from (15 to 90) ms depending on the fluid velocity. Images pairs were taken at 0.5 s and 1.0 s intervals. For accurate statistics and time sequences, the PIV measurements typically consisted of 20000 to 30000 image pairs.

The particle images were processed in three subsequent steps. In the first step, interrogation areas of 32×32 pixels which had an overlap of 50 % were cross-correlated. A local median filter was used to remove spurious vectors and the removed vectors were filled with interpolated values from the neighbouring interrogation areas. The resulting particle displacements are used as window displacement for the next step, an adaptive cross-correlation with interrogation areas of 16×16 pixels with a 50 % overlap. After filtering and interpolation the third step follows the same procedure for 8×8 pixels interrogation areas. Depending on the seeding and illumination conditions the analysis of the images for some experiments only comprised the first two steps. In all cases the number of filtered out vectors was smaller than 4 % of the total amount of vectors.

4.2.2 LDA measurements

The LDA measurements were performed with two one-component laser Doppler anemometers, depicted in Fig. 4.3(b). The green ($\lambda = 514\ \text{nm}$) and blue ($\lambda = 488\ \text{nm}$) colours of a 5 W Spectra-Physics Argon-ion laser are used to measure two velocity components simultaneously. Both colours were split and one beam of each colour was frequency pre-shifted 40 MHz by a Bragg cell to detect instantaneous flow reversals. The flow was seeded with $5\ \mu\text{m}$ polyamide seed particles. The light scattered by these particles was collected in on-axis forward direction, which, in comparison to back-scatter, results in a superior signal-to-noise ratio of the Doppler signals. The outputs of these photomultipliers were down-mixed electronically to an effective pre-shift frequency of 30 kHz and were led to two signal processors. In the described experiments in the following chapters, we used two pairs of signal processors, a TSI IFA-750 signal processor and two Dantec BSA signal processors. The measured Doppler burst are further analysed with the respective TSI and Dantec commercial software packages. In general, both systems measured the instantaneous velocities of the seed particles with an inaccuracy of 0.5 %. The length and diameter of the measurement volumes was in all experiments sufficiently small ($0.8\ \text{mm} \times 0.1\ \text{mm}$)

	R15C20W (large)	R15C10W (small)	R30C5WA
size	~ 50 μm	~ 20 μm	
red start	15 $^{\circ}\text{C}$	15 $^{\circ}\text{C}$	30 $^{\circ}\text{C}$
colour play 20 $^{\circ}\text{C}$	10 $^{\circ}\text{C}$	5 $^{\circ}\text{C}$	
red start in set-up ~ 13 $^{\circ}\text{C}$	~ 14 $^{\circ}\text{C}$	28 $^{\circ}\text{C}$	
effective bandwidth	~ 6 $^{\circ}\text{C}$	3 $^{\circ}\text{C}$	6 $^{\circ}\text{C}$
density	nearly naturally buoyant	nearly naturally buoyant	

Table 4.2: Characteristics of Hallcrest R30C5WA liquid crystal sheet and Hallcrest R15C20W and R15C10W liquid crystal slurries (Witte, 2006). The liquid crystals in the R15C20W and R15C10W slurries are referred to as large and small crystals respectively. The red start and effective bandwidth in the setup denote the observed values for the actual viewing angle.

to resolve the smallest length scales of the flow.

Depending on the type of measurement and the measurement location, the mean data rate varied between 10 Hz and 30 Hz. For moderate Ra numbers, the relatively low characteristic velocities result in a relatively low data rate. The higher data rates can be obtained for $Ra > 10^8$ and electromagnetically forced flows. Furthermore, measurement locations in the direct vicinity of the walls have an inherently lower data rate than in the centre of the cell due to the low volume flux.

Since the time scales in thermal convection are relatively long, each measurement series comprised typically (3600 to 1.8×10^5) s. All first and second order statistics were computed as transit-time weighted results to eliminate velocity bias effects.

4.2.3 TLC measurements

Suspended liquid crystals

Encapsulated liquid crystals from Hallcrest were used for the suspended liquid crystal measurements. These encapsulated spheres consist of raw liquid crystal material coated with a layer of gum arabic, as explained in Section 3.3.1. A disadvantage of the encapsulation is the different and more diffusive refraction, which causes a less pronounced colour signal than when using unencapsulated liquid crystal material. Two types of suspended liquid crystals have been used in the present work. Their specifications can be found in Table 4.2.

Concentration of suspended liquid crystals

The liquid crystals are delivered by the manufacturer in a slurry composed of 40 % liquid crystal and 60 % water. The concentration of liquid crystal particles needed per measurement is determined empirically and depends on the way the data is processed. The liquid crystal concentration ϕ_{LC} is defined as the ratio of the volume of the liquid crystal material and the volume of the working fluid. Hekker (2003) used a low liquid crystal concentration, $\phi_{LC} < 0.1 \times 10^{-3} \%$ in an attempt to determine the hue for individual crystals. However, it appeared to be very difficult to determine the hue value for individual crystals accurately and Hekker (2003) reported coarse temperature fields for which large regions remained without temperature information. Witte (2006) focused on determining the mean hue value of groups of liquid crystal in small zones where higher liquid crystal concentrations could be used. In the present Rayleigh-Bénard set-up Witte (2006) found an empirical maximum of $\phi_{LC} = 0.3 \times 10^{-3} \%$. When the concentration is higher, the illumination is negatively affected by the “milky” appearance of the abundant liquid crystal material.

Calibration

The calibration of the liquid crystal response to temperature is performed in an automatic procedure using a dedicated software application. Both plate stacks, and subsequently the working fluid in the cell, are heated very slowly, in the order of 2 K h^{-1} .

To ensure the fluid in the convection cell has a uniform temperature, a small pump circulates the fluid during a calibration. In this way settling of liquid crystals particles is prevented. The encapsulated particles are slightly heavier than water and could form a reflective layer without a flow in the cell.

During the calibration, the fluid’s temperature and the temperature of the plate stacks is constantly monitored by the software and an accurate average is calculated of at least six thermocouples in the convection cell. When the temperature has increased with a chosen temperature value, the camera system is triggered to acquire a number of images of the liquid crystals at the current temperature. The temperature interval per calibration step is small, typically, 0.05 K or 0.10 K. For each step 20 image frames are captured, which are stored for further processing.

Calibration curve

A typical calibration result is shown in Fig. 4.4. The part of the curve where the hue-temperature curve is a monotonically rising function, i.e. where a one-to-one

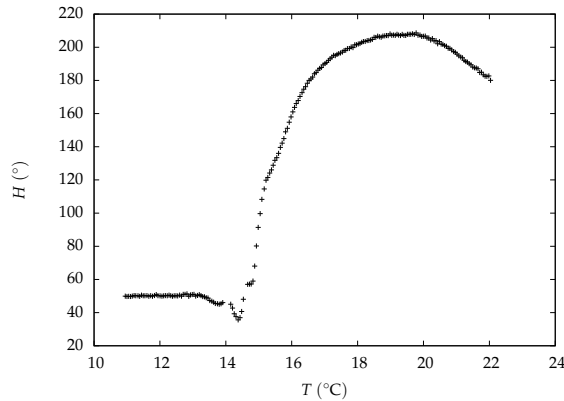


Figure 4.4: A typical hue-temperature calibration result.

relationship between hue and temperature exists, is the range where temperature values can be obtained.

Witte (2006) gives a detailed picture on the effects of the filters that were discussed in Sect. 3.3.5 on the calibration curves. The uncertainty in temperature is calculated from the standard deviations in the observed hue values during calibration (the local derivative of each calibration curve):

$$\delta T = \left| \frac{dT}{dH} \right| \delta H, \quad (4.2)$$

with δT and δH respectively the uncertainties in temperature and $\frac{dT}{dH}$ the slope of the calibration curve at this temperature. The temperature uncertainty is around 0.1°C , a typical value for LCT applications Kasagi et al. (2001); Dabiri (2009).

Illumination

Two Schott-Fostec DC regulated light sources illuminate the liquid crystals during the measurements. The devices are equipped with two 150 W DDL halogen lamps with a colour temperature of approximately 3150 K. After passing an infrared filter, the light is transferred through fibre optic cables to two 30 cm Schott-Fostec lightlines (A08912), depicted in Fig. 4.3(c), which generate a slightly divergent light sheet.

For suspended liquid crystal measurements, a perspex cylinder is placed in front of each lightline to create a uniform light sheet, comparable with the sheet optics for PIV. Both light sources are mounted opposite to each other to ensure a well illuminated light sheet over the full width of the cell. For liquid crystal sheet measurements

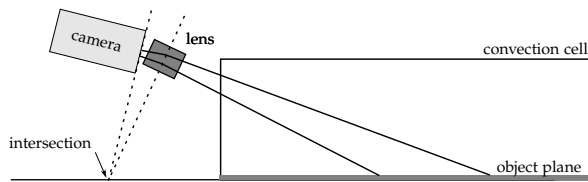


Figure 4.5: Schematic of the Scheimpflug condition for acquiring sharp images. The CCD sensor, lens and object plane must intersect at a single line.

the lightlines are mounted at the side of the tank without a lens in order to illuminate the bottom plate.

A “white” light source, i.e. a light with colour temperatures close to that of normal daylight (6500 K) is required for the liquid crystal response to pass through the entire visible spectrum with varying temperature. The use of different halogen lamps, i.e. 50 W Solux halogen lamps with a colour temperature of 4700 K, resulted in a better spectral emittance, but the lack of power disqualified this option (Witte, 2006).

Liquid crystal sheets

For investigating heat transfer at the top and bottom walls, liquid crystal sheets from Hallcrest (R20C5, details in Table 4.2) has been mounted on the wall. The material changes colour which can be observed with a PCO Sensicam Colour camera. For MHD experiments, the colour camera can be mounted directly above the tank viewing the liquid crystal sheet through a glass top plate. When buoyant forcing is used, the camera views the liquid crystal sheet through one of the side windows. To obtain sharp images, the Scheimpflug condition is used, i.e. the CCD sensor plane, lens plane and the observed liquid crystal plane must intersect in a single line, as illustrated in Figure 4.5 (Raffel et al., 1998). Notice that the angle of inclination is limited due to height of the tank. The tilt reduces the effective angle of view and thus enlarges the dynamic range of the LCT system.

Like for the suspended liquid crystal measurements, the colour-temperature calibration is carried out in-situ for liquid crystal sheets. As for the suspended liquid crystals, during the calibration the fluid temperature is slowly increased. This to ensure a minimal temperature difference between the plate and the working fluid, which is important to find a reproducible liquid crystal colour.

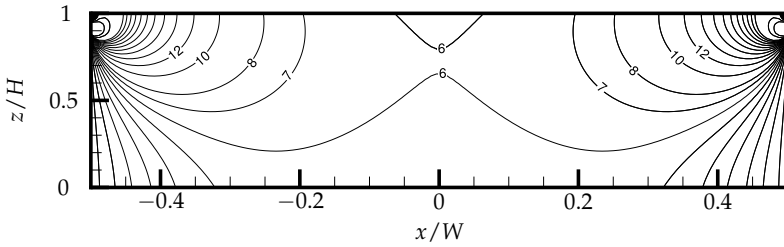
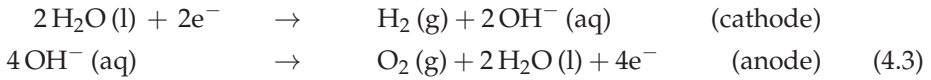


Figure 4.6: Calculated horizontal component j_x of the electric volume current density in A m^{-1} for an input current of 1 A.

4.3 Electromagnetic forcing

To introduce a significant MHD force onto the working fluid in the cell, an electric field has to be applied in the cavity. This field is generated by applying an electric current through mounted Platinum wires at two opposing sides of the glass tank. The electrodes are submerged in the measurement fluid in two designated cavities. By passing an electrical current through the system, electrons are freed at the anode as ions in the fluid. The electrolysis consists of two reactions:



The electrodes are connected to a current supply, generating typically $I = 2 \text{ A}$ at $V = 10 \text{ V}$. The resulting electrical field distribution or volume current density \vec{j} can be derived from the amount of charge dI crossing a unit area A_\perp unit time (Griffiths, 1989; Jackson, 1999; Rossi, 2001):

$$I = \int \vec{j} \cdot d\vec{A}_\perp \Rightarrow j_x = \frac{dI}{dA_\perp}. \quad (4.4)$$

Fig. 4.6 depicts the calculated horizontal component of the current density j_x for a cross section of the set-up at $I = 1 \text{ A}$. The placement of the electrode at the top of the tank leads to the most homogeneous field near the bottom of the tank, i.e. the location where the permanent magnets have their largest influence.

4.3.1 Working fluid

The electrical conductivity of degassed tap water for the thermal convection experiments is quite low, i.e. it typically varies between $\sigma = (5 \times 10^{-4} \text{ and } 5 \times 10^{-2}) \text{ S m}^{-1}$. To significantly increase the conductivity without changing the

		water	7% Na ₂ SO ₄ solution
density ρ	(kg m ⁻³)	995.4	1061.9
dynamic viscosity η	(kg m ⁻¹ s ⁻¹)	0.797×10^{-3}	1.244×10^{-3}
electrical conductivity σ	(S m ⁻¹)	5.00×10^{-2}	5.55
kinematic viscosity $\nu = \frac{\eta}{\rho}$	(m ² s ⁻¹)	0.801×10^{-6}	1.172×10^{-6}
thermal diffusivity κ	(m ² s ⁻¹)	0.147×10^{-6}	1.386×10^{-7}
thermal expansion coefficient α	(K ⁻¹)	0.303×10^{-3}	0.303×10^{-3}

Table 4.3: Physical properties of water and 7% Na₂SO₄ solution at $T = 20^\circ\text{C}$ (Roth and Scheel, 1923; Lide, 2006).

physical properties of the observed fluid too much, a salt is added to the fluid. In this way viscosity will not deviate much from that of tap water and the fluid remains optically accessible. Sodium sulphate (Na₂SO₄) has been added to the water to create a 7% (by weight) Na₂SO₄ solution. Although common substances as sodium chloride (NaCl), sulfuric acid (H₂SO₄) and hydrochloric acid (HCl) could increase the conductivity even further, those solutions would imply large safety adjustments. The less hazardous Na₂SO₄ solution acts as a good compromise between practicality and increased conductivity. The ratio of the absolute viscosity of the solution to that of water at 20 °C is 1.242 (Lide, 2006). A comparison of the working fluid for the MHD experiments is given in Table 4.3.

4.3.2 Permanent magnets

To introduce a Lorentz force, as described in Sect. 2.3, permanent neodymium-iron-boron (Nd₂Fe₁₄B) magnets are placed underneath the lower copper plate stack. Two configurations have been used, which are depicted in Fig. 4.7. The material, an alloy of neodymium, iron and boron, is currently known as the strongest type of permanent magnet, having an intrinsic field strength $|\vec{B}_0| = (1.0\text{--}1.4)$ T. The field strength of the permanent magnets was measured several times with a Hall-flux sensor, where its magnitude was found to be 1.0 T. To increase the range of influence in the working fluid of the cell, $40 \times 40 \times 84$ mm³ magnetic blocks are constructed from 16 smaller ($10 \times 20 \times 42$ mm³) blocks each, held together by a strong non-ferro metal clamp and mounted on an iron plate.

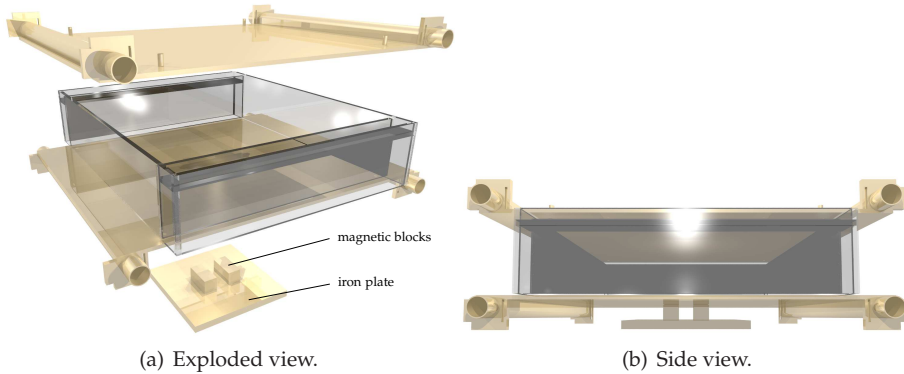


Figure 4.7: The set-up used for MHD experiments.

4.3.3 Forcing

The present set-up implies some simplifications in the induction equation, Eq. 2.43. As the electrical conductivity σ is relatively low and the fluid velocity moderately large, the magnetic Reynolds number $Re_m \ll 1$. Because of the use of permanent magnets, the induction term can be neglected as well, i.e. $\frac{\partial \vec{B}}{\partial t} = 0$. Thus, the induction equation reduces to

$$\nabla^2 \vec{B} = 0. \quad (4.5)$$

As a consequence, the magnetic field can be approximated as purely diffusive. Additionally, the induction part in Ohm's law, Eq. 2.40, is very small compared to the current terms due to the electric field. Therefore, the electric density is then only imposed by the external electric field:

$$\vec{j} = \sigma \vec{E}. \quad (4.6)$$

The electromagnetic body force $f_{i,em}$ in Eq. 2.3 can be substituted by the Laplace force in Eq. 2.39. If the Eqs. 4.5 and 4.6 are used, the electromagnetic body force becomes

$$f_{i,em} = \vec{j} \times \vec{B} = \sigma \vec{E} \times \vec{B}. \quad (4.7)$$

Using the characteristic scales for Eq. 2.45 leads to a Hartmann number $Ha \sim 10^1$ for all experiments. Thus, the electromagnetic forces are high enough to overcome the damping forces caused by viscous terms. The interaction parameter, Eq. 2.46, becomes $N \sim 10^{-1}$, which indicates that the flow in the cell is dominated by inertia.

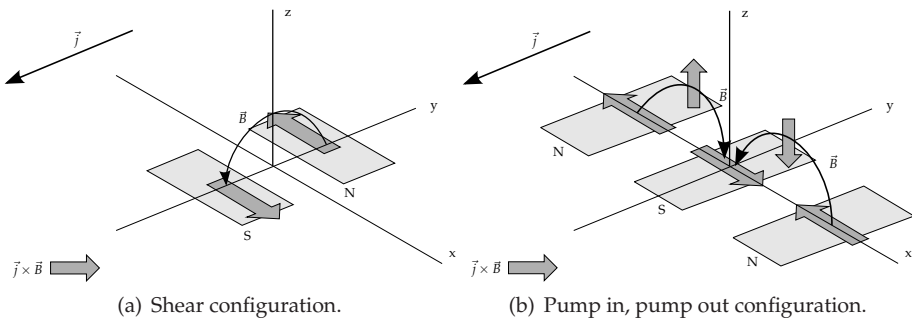


Figure 4.8: Sketches of used MHD forcing configurations.

4.3.4 Configurations

The gradient of the magnetic field can be positioned perpendicular and normal to the electric field, leading to two standard configurations, displayed in Fig. 4.8.

In Fig. 4.8(a) two magnetic blocks with alternating polarity are placed 0.04 m from each other. The Lorentz force F_L is maximum above the surface of the magnets and zero in between the magnets, where \vec{j} and \vec{B} are aligned parallel. This configuration leads to a mainly two-dimensional force above the magnetic blocks. The two magnet configuration will be referred to as the *shear* configuration.

In Fig. 4.8(b) three magnetic blocks with alternating polarity are again placed 0.04 m from each other, but now the gradient in the magnetic field is aligned normal to the current density \vec{j} . In this configuration the Lorentz force has always a non-zero value in the x, z plane and an attraction and repulsion area are created. This configuration will be referred to as the *pump in, pump out* configuration.

5

Digital particle image velocimetry and thermometry in turbulent Rayleigh-Bénard convection

This chapter describes an investigation of turbulent flow structures and their correlation with the instantaneous heat transfer in an aspect-ratio-four Rayleigh-Bénard (RB) convection cell. In RB convection, the formation of plumes and their impingement is associated with motion in the wall boundary layers, governing the heat transfer. The distinct structures important in RB convection Rayleigh-Bénard convection are investigated quantitatively using digital particle image velocimetry and liquid crystal thermometry.

5.1 Introduction

Heat transfer by convection is a common topic in the field of applied engineering. Mostly, a combination of laminar and turbulent flows, consisting of free and natural convective flows, is employed. The effect of laminar flows on heat transfer is well understood. This is in contrast to turbulent convective heat transfer, which is often difficult to simulate numerically or to measure experimentally.

Whereas (digital) particle image velocimetry (PIV) has been the commonly used technique for measuring planar velocity fields in fluids, there is no de-facto standard for measuring two-dimensional temperature fields. Two techniques that are frequently used for this purpose are planar laser-induced fluorescence (PLIF) and liquid crystal thermography (LCT). In the first, a temperature dependent dye is made to fluoresce by laser light and a calibration is then used to relate the intensity of

the fluorescence to the fluid temperature (Coolen et al., 1999; Seuntjens et al., 2001; Watanabe et al., 2007). The second technique uses thermochromic liquid crystals, which when illuminated with white light, reflect a specific dominant wavelength depending on their temperature. Small particles of this material suspended in the fluid can act as local temperature probes. These thermochromic liquid crystals (TLCs) are commonly used to measure temperatures qualitatively (Dabiri and Gharib, 1996; Kowalewski, 1999; Fujisawa and Funatani, 2004; Dabiri, 2009). Seeding a fluid with TLC tracers provides local temperature information by the colour variation and enables velocity information by calculating a particle image correlation on subsequent images.

Besides the abovementioned techniques, several experiments in Rayleigh-Bénard convection have been carried out using the refractive properties of the Rayleigh-Bénard system. Chu and Goldstein (1973) used a helium-neon laser and an interferometer to perform measurements of the mean temperature. Cerisier et al. (2002) used laser beam deflection to study temperature gradients in Rayleigh-Bénard convection. A review of early day experiments of turbulence in wide horizontal fluid layers can be found in Adrian et al. (1986).

This chapter reports on a detailed study of long-term velocity and temperature measurements in an aspect-ratio-4 Rayleigh-Bénard convection cell for a range of moderately high Rayleigh numbers. The experimental set-up will be described first, after which the measurement techniques, calibration procedure and data processing are explained. Lastly, the results of the velocity and temperature measurements for the full measurement volume and zoomed-area will be presented.

5.2 Methodology

5.2.1 Experimental set-up

The experimental set-up consists of a $600 \times 600 \times 155 \text{ mm}^3$ ($W \times W \times H$) cell with horizontal top and bottom walls that are kept at constant temperatures, see Fig. 4.3(c). These constant-temperature walls are stacks of plates, each consisting of two 3 mm thick flat copper plates, with 3 mm high, small copper cylinders in between, thus creating a hollow cavity through which a cooling/heating fluid can flow. In this way, the plate stacks can impose a constant temperature difference on the working fluid in the cell.

To keep each horizontal wall at constant temperature (the top wall cold and the bottom wall hot), the plate stacks are connected to two 300 l water basins that are kept at constant temperature with an inaccuracy of 0.02 K. The cooling/heating water is

transported through the top and bottom temperature system by two pumps connected to the outlets of the plate stacks. The pumps suck the fluid through the stacks and thus create a pressure drop within the plate stacks ensuring the mechanical stability and flatness of the plate stacks.

5.2.2 Rayleigh-Bénard system

To ensure the temperature difference between the inlet and the outlet of the plate stack remains within a maximum difference δT , the water volume flow of the heating and cooling circuits have to be sufficiently large. The maximum tolerable temperature difference was, somewhat arbitrarily, set to $\delta T = 0.1$ K. The temperature difference ΔT between the top and bottom plate of the measurement volume is typical 10 K. Using an estimation of the Nusselt number, Eq. 2.37, scaling and the properties of the working fluid in Table 4.1, the required heat flux for this typical case becomes $q'' = 2.2 \times 10^3$ W m⁻².

A plate stack covers an area of $W^2 = 0.36$ m² and is insulated at the side not exposed to the measurement volume. This results in a required power $P = 1.8 \times 10^3$ W to be delivered by the cooling and heating circuits. This power is related to the volumetric flow rate Q of the water passing through the plate stacks and the temperature difference δT between inlets and outlets:

$$P = \rho c_p Q \delta T. \quad (5.1)$$

For the abovementioned power and a temperature difference $\delta T = 0.1$ K, the volume flow Q through the system should be $Q = 1.1 \times 10^2$ l min⁻¹ to transport the required amount of heat. As the pumps in the cooling and heating system deliver a constant flow rate around 2×10^2 l min⁻¹, the requirement $\delta T < 0.1$ K is fulfilled for all experiments. Moreover, the plate's internal thermocouples showed that the actual temperature deviation over the plate was indeed smaller than 0.1 K during the performed experiments.

5.2.3 Velocity measurements

For single PIV velocity measurements, not combined with LCT, the velocity field was measured using a PIV system including a Continuum Minilite double-pulsed Nd:YAG laser with a pulse energy of 25 mJ. This laser produced an approximately 1 mm thick light sheet that illuminated the seeding particles in the flow. The working fluid in the cell was seeded with hollow glass spheres (Potters-Ballotini) with a diameter of approximately 10 μm at a concentration of approximately 1.0×10^{-2} g l⁻¹.

For the use of PIV combined with LCT, the flow was illuminated by the continuous light source. The timing of the two individual PIV snapshots was determined by the exposure times of the cameras and a delay between the exposures.

Two PCO Sensicam cameras, one black-and-white and one colour camera, both with a resolution of 1280×1024 pixels recorded images of the seed particles in the light sheet, see Fig. 4.3(c). The field-of-view per camera was about $0.35 \times 0.16 \text{ m}^2$. A 28 mm focal length lens with a numerical aperture $f^\# = 4$ was mounted on each camera. Due to the small maximum velocity, the time separation between pulses was set to 25 ms. Because two cameras from different viewpoints observed the flow, a two-dimensional interpolation function was used to create a regularly spaced velocity field of the whole domain (Shepard, 1968).

PIV measurements were performed in the x, z -plane in the middle of the measurement volume at $y = 0$. The image pairs were analysed using the commercial software VidPIV Rowan v4.0g in three subsequent steps as described in Sect. 4.2.1. The number of non-valid vectors is about 2 percent of the total number of vectors.

5.2.4 Temperature measurements

Temperature measurements in the Rayleigh-Bénard cell were performed using the liquid crystal measurement technique. A suspended liquid crystal slurry (Hallcrest, R15C10W) was added to the working fluid resulting in 0.3 vol.% of liquid crystal (LC) material. The size of the LC particles was approximately $20 \mu\text{m}$. The normal temperature range indicated by the manufacturer was 10 K. However, in the present experiment, the liquid crystal particles were observed under an angle of 90 degrees with respect to the illumination plane. This reduced the effective temperature bandwidth to 4 K.

Two Schott-Fostec DC regulated light sources illuminate the liquid crystals during the measurements. Each light source is equipped with a 150 W DDL halogen lamp with a colour temperature of approximately 3150 K. After passing an infrared filter, the light is transferred through fibre optic cables to a Schott-Fostec lightline (A08912) to produce a slightly divergent light sheet of 0.30 m height. To reduce the divergence of the light sheet, a perspex cylindrical lens is placed in front of each lightline. Both lightlines are mounted opposite to each other to produce a well illuminated light sheet over the full width of the cell, as illustrated in Fig. 4.3(c).

5.2.5 Data processing and calibration

A common procedure to determine temperatures from liquid crystals is to use a hue-to-temperature conversion. In the first step of this procedure the red, green and blue (RGB) triplets obtained from camera images are transformed to a perceptual HSV (or HSI) colour space. The H , S , and V coordinates stand for *hue* (H), *saturation* (S), and *value* (V). The latter is sometimes called *intensity* (I). Several algorithms for the transformation of RGB coordinates to HSV transformation coordinates are described in literature. Most commonly used is the algorithm proposed by Hay and Hollingsworth (1996), Eq. 3.24. However, in the present experiment a computationally less demanding transformation is used, Eq. 3.27, that produces nearly the same results.

To form a bijective relation between hue and temperature, an in-situ calibration is performed that takes into account variations in experimental conditions like the lighting system, liquid crystal concentration, and the observation angle. The in-situ calibration of the liquid crystals is performed in an automatic procedure using a dedicated software application. Both plate stacks, and subsequently the working fluid in the cell, are heated very slowly, at a rate of approximately 2 K h^{-1} . To ensure the working fluid in the cell has a uniform temperature, a small pump stirs the fluid during the calibration. Stirring of the working fluid is required because the encapsulated particles are slightly heavier than water. Therefore, the particles could form an unwanted, reflective layer on the bottom of the cell due to settling of the particles in case of the working fluid is stagnant

The used PCO Sencam incorporates a Bayer filter instead of having three separate CCD chips for the different colours. Therefore, no problems of colour calibration or white balancing need to be taken into account, except for having the same colour calibration during the calibration phase and during the measurements. As in Günther and Rudolf von Rohr (2002a), it is emphasised that the liquid crystal tracers have a particle (image) diameter that is sufficiently large for performing both LCT and PIV measurements in a transient flow.

As indicated in Fig. 5.1, the temperature and velocity fields are obtained from the same colour images but in different steps. Each of the two sequential snapshots is converted from RGB to HSV. The intensity information is extracted for the two frames used for PIV evaluation. The hue component is used with the hue-temperature calibration curve to extract temperatures. Each colour pixel is converted from four physical pixels, as explained in Sect. 3.3.4.

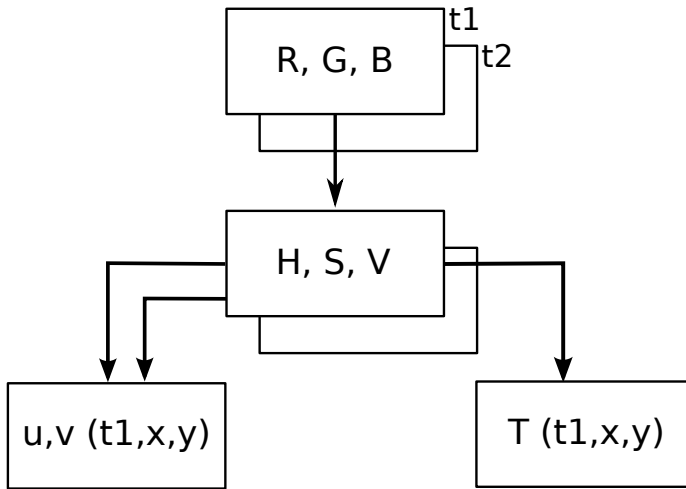


Figure 5.1: Data processing procedure from two raw RGB image frames to a velocity field and a temperature field.

Zone averaging

As the liquid crystal particle images are not fully covering the CCD sensor, temperature information cannot be obtained from each colour pixel. To get a continuous temperature field, one can either interpolate the hue field before conversion to temperature or interpolate the temperature field after the conversion. In Fig. 5.2 both methods are visualised. In the left a raw colour image of a liquid crystal measurement is depicted. The middle images depict the hue value after conversion to HSV and filtering the low intensity and saturation pixels. The red squares in the lower image illustrate the division of the image into measurement zones. For each measurement zone, the mean hue values are derived. A typical zone size is about 8×8 colour pixels. The fields on the right of Fig. 5.2 depict the temperature fields that result when the (mean) hue values are related to temperature. Witte (2006) has reported that averaging of valid hue values in a certain zone of pixels, comparable to the common interrogation zones used with PIV, gives the best results and the smallest error in the obtained temperature field.

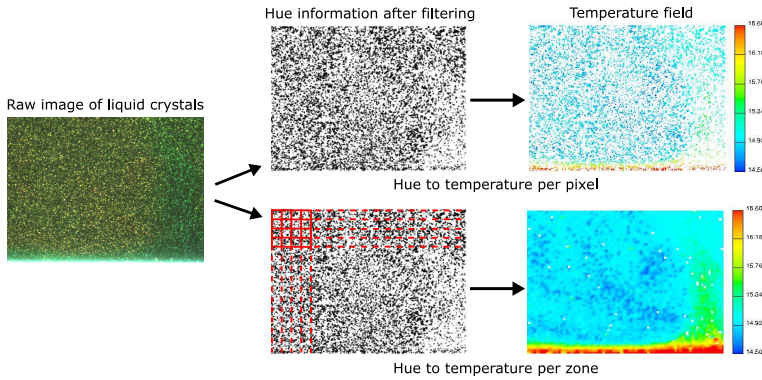


Figure 5.2: The difference between pixel-based and zone-averaged processing.

Ra	3.7×10^7	3.9×10^7	3.3×10^8	5.9×10^8	6.1×10^8	6.2×10^8	7.4×10^8	1.1×10^9	2.8×10^9	3.7×10^9
Pr	7.0	7.0	5.5	5.3	5.4	5.4	6.9	5.9	5.0	5.1

Table 5.1: Overview of Rayleigh and Prandtl numbers of the performed experiments.

5.3 Results

5.3.1 Velocity measurements

PIV measurements were performed at 10 different Rayleigh numbers, as indicated in Table 5.1. For each Ra number between 1×10^4 and 3.3×10^4 snapshots were obtained at a rate of 2 Hz. Fig. 5.3 shows the vertical profiles of the variance of both measured velocity components at different horizontal locations in the tank for three Ra numbers. x ranges from the edge of the cell ($x = 0.20$ m to the centre $x = 0.5$ m). For $Ra = 3.3 \times 10^8$ and $Ra = 3.7 \times 10^9$, the horizontal velocity component exhibits a peak near both walls. The location of the peak is commonly used to determine the kinematic boundary layer height. For $Ra = 3.7 \times 10^7$, the horizontal velocity variance profile is less clear, most likely as turbulent levels are too low to have an influence upon the full width of the cell.

The variance of the vertical velocity components show the same distinction between high and low Ra. For the higher Rayleigh numbers, the vertical velocity variances are similar over the full width of the cell, with an exemption of some edge effects for $x = 0.25$ m for $Ra = 3.7 \times 10^9$. For the lower Rayleigh number, the vertical velocity variance is maximum in the tank's centre, and is decreasing towards the side. Due to the presence of the electrode cavity (see Sect. 4.3) the layer closest to the to plate of the cell $z = 0.15$ m was not illuminated well. As a consequence, the result near $z = 0.15$ m are not as accurate at the results near $z = 0$.

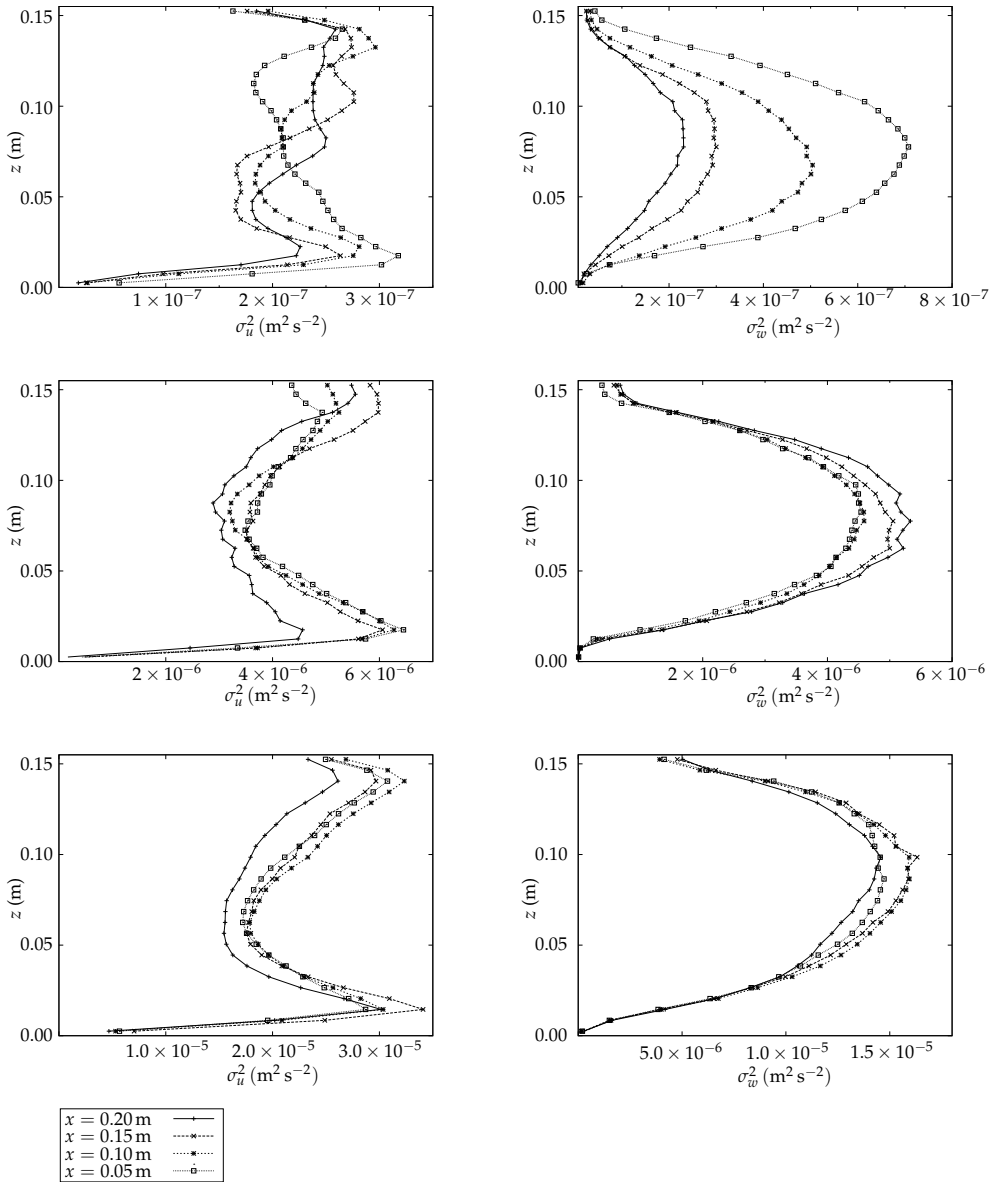


Figure 5.3: Horizontal velocity variance σ_u^2 (left), and vertical velocity variance σ_w^2 (right), profiles for three decades of Ra: $Ra = 3.9 \times 10^7$, $Ra = 3.3 \times 10^8$, and $Ra = 3.7 \times 10^9$.

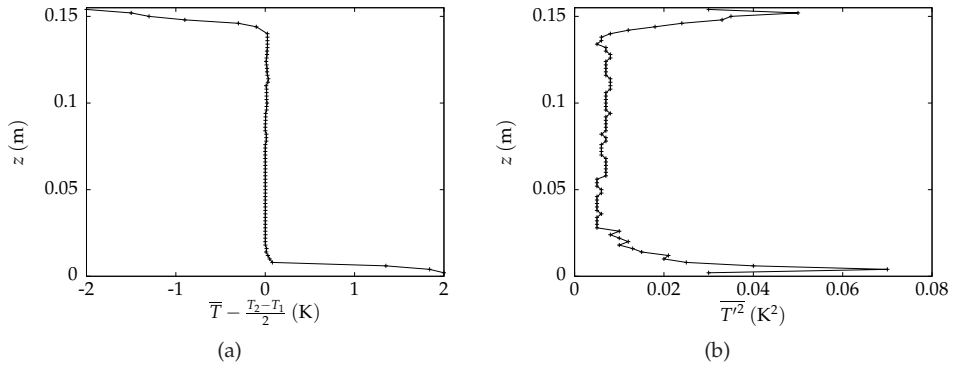


Figure 5.4: Mean temperature (a) and variance (b) for a Rayleigh-Bénard convection experiment at $Ra = 2 \times 10^8$.

5.3.2 Temperature measurements

In Fig. 5.4(a) the mean temperature field of 3.2×10^4 individual snapshots is depicted for an experiment at $Ra = 2 \times 10^8$. The curve confirms the traditional view of a well-mixed bulk region and strong gradients in the thermal boundary layers near the top and the bottom walls. Fig. 5.4(b) shows that the variance is nearly uniform in the bulk. Only a few measurement points are available near the top wall, due to the sub-optimal illumination conditions as explained before. This explains the difference in the maxima near the top and bottom wall.

5.3.3 Temperature measurements near-wall region

Another feature of Rayleigh-Bénard convection studies is the behaviour of thermal plumes. Plumes are regarded as a major transport mechanism of heat in Rayleigh-Bénard convection and their interaction with the large-scale circulation is a topic of intense research (see also the next chapters). Using the liquid crystal technique, the plume formation process can be investigated quantitatively. Fig. 5.5 shows a series of snapshots of temperature distributions in a vertical plane near the top wall for a measurement at $Ra = 1.7 \times 10^8$ as determined with the suspended liquid crystals. The time interval between the images is 2 s.

The eruption of a plume from the thermal boundary layer can be followed quantitatively. We observed waves travelling along the top of the boundary layer and an accumulation of heat in the thermal boundary layer thus forming a local thickening of the layer. These hot spots were slightly warmer than the average temperature in

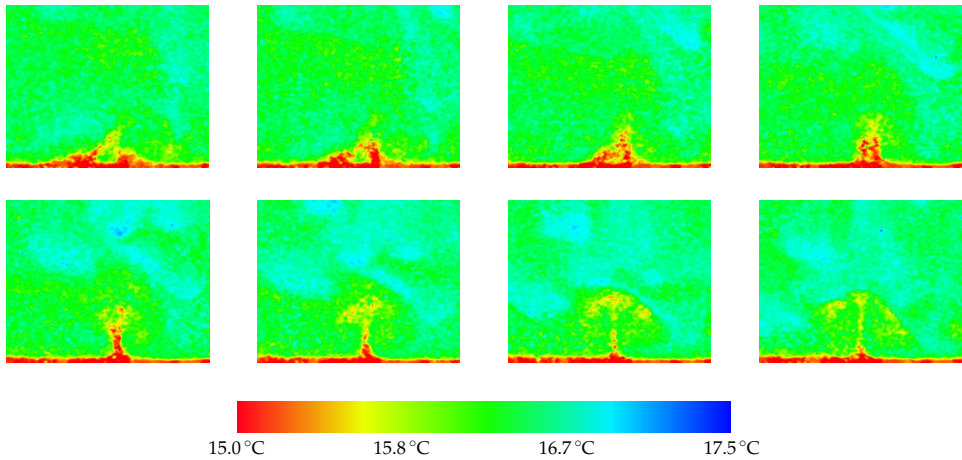


Figure 5.5: Temperature measurement series near the bottom wall in the x, z -plane during a Rayleigh-Bénard convection measurement at $Ra = 3 \times 10^8$. Area of view: $40 \times 60 \text{ mm}^2$.

the layer. The first snapshots in Fig. 5.5 show an accumulation of heat within the boundary layer, thus forming a bulge. Hot fluid erupts from the bulge, and rises vertically in a thin sheet. The thickness of this sheet appears to decrease when the plume continues to rise. While moving further upwards, the plume decelerates and cools down due to heat transfer with the cold surroundings.

Since the orientation of the measurement plane is normal to the spanwise direction of the thermal plume, a typical mushroom-type structure appears. The vertical rise velocity of the plume indicates that at this particular moment, the convection velocity of a possible large scale circulation is either zero or normal to the plane in which the temperature distribution is measured.

In the last snapshots of Fig. 5.5, the heat flux from the thermal boundary layer decreases. The centre part of the plume decays due to shear near the “tail” of the plume. Finally, the plumes breaks down and both edges consisting of still relatively warm fluid move as separately structures in the flow. Surprisingly, these relative, warm structures are advected downward due to the shear of the surrounding cold fluid, while one would expect they would tend to rise due to buoyancy. We observed that these structures, which are separated from the boundary layer transport warm fluid quite efficient, were less vulnerable for mixing with downward moving fluid than the plumes.

Howard (1964) described a “bubble model” in which the thermal boundary layer thickens in time, causing the upward diffusion of the temperature field. The boundary layer erupts when a critical thickness is attained and all the hot, buoyant fluid is expelled into the bulk layer. The depleted boundary layer will grow by the continu-

ous inflow of heat and the process will repeat itself. The scavenging plume model, suggested by Krishnamurti (2000), adds a horizontal dimension to the model. As we observe in Fig. 5.5, this model suggests that the plumes remain attached to the boundary layer for a longer time, letting the plumes extend further, until the source of heat from the boundary layer is depleted. When the plume disconnects, the boundary layer will be thinner locally at the eruption spot, and will be a favourite position for new plumes to grow. The observations of the thermal plumes in our set-up confirm this behaviour.

5.4 Concluding remarks

Two optical measurement techniques, particle image velocimetry (PIV) and liquid crystal thermography (LCT), were used to obtain statistical information and study structures in Rayleigh-Bénard convection. Velocity measurements show over two decades of Rayleigh number a typical distinction between the measurements for $Ra < 1 \times 10^8$ and $Ra > 1 \times 10^8$. The near-wall temperature measurements give insight on the vertical structure of thermal plumes as well as its creation and decay. The experiments reveal a cause for the preferential plume eruption location in Rayleigh-Bénard convection.

6

Oscillating large-scale circulation in turbulent Rayleigh-Bénard convection

In this Chapter, we report on the dynamics and structure of the turbulent velocity field in a high-Rayleigh-number ($Ra = 5.9 \times 10^8$) thermal convection cell with an aspect ratio of four. Spectral density functions (measured with laser Doppler velocimetry) indicated the existence of a large scale periodic component. The long-time mean flow field (measured with particle image velocimetry) revealed that the large scale circulation in the aspect-ratio-four cell consists of two co-rotating rolls. The periodicity in the flow could be traced back to the alternating growth and decay of these rolls.

6.1 Introduction

Rayleigh-Bénard convection (RBC) in a fluid layer between two horizontal surfaces heated from below and cooled from above has long been regarded as a paradigm of many examples of thermal convection encountered in nature and in man-made environment. RBC is characterised by the Rayleigh number $Ra = g\alpha\Delta TH^3/(\kappa\nu)$, the Prandtl number $Pr = \nu/\kappa$ and the aspect ratio $\Gamma = W/H$. Here, g is the gravitational acceleration, ΔT is the temperature difference between the plates, H is the distance between the plates, and W is the lateral extent of the plates. The symbols α , ν and κ are the fluid's thermal expansion coefficient, kinematic viscosity, and thermal diffusivity, respectively. Despite the simplicity of the geometry, the boundary conditions and extensive studies, many physical phenomena in RBC are not fully understood (Siggia, 1994; Kadanoff, 2001). Among the most debatable issues is the scaling law for heat transfer, especially above approximately $Ra = 4 \times 10^7$, see Niemela et al. (2000). Underlying the discussion about the appropriate value of the exponent of the Ra number are the possible differences in the dynamics of the turbulence and large-scale convective structures, which may be easily overlooked in experimental studies of the global heat transfer without having sufficient insight into the flow and turbulence field. Experiments in RBC cells have been conducted in a wide variety of Ra , aspect-ratios and flow media, but detailed quantitative studies of the turbulent flow field are scarce, and, as pointed out by Qiu and Tong (2001), often hampered by the use of sub-optimal measurement techniques. In a transparent fluid like water, the techniques of choice for velocity measurements are laser Doppler anemometry (LDA) and particle image velocimetry (PIV). Both techniques are non-intrusive. The strength of the latter lies in its ability to capture (instantaneous) velocity fields, while the former is a single-point technique capable of measuring velocity time-series with superior spatial and temporal resolution. LDA has been applied to study RBC by Qiu et al. (2000); Qiu and Tong (2001) and Shang et al. (2003), whereas PIV has been conducted by Prasad and Gonuguntla (1996), Xia et al. (2003) and Sun et al. (2005b).

In this Chapter, we report on experimentally detecting an oscillating convective pattern from long-term velocity measurements in an aspect-ratio-four ($\Gamma = 4$) RBC cell at $Ra = 5.9 \times 10^8$. Grossmann and Lohse (2003) argue that the majority of studies on RBC concentrate on cells with an aspect ratio of approximately one, and that future experiments on RBC should be aimed at large aspect ratios. The present experiment can be seen as a step in that direction. Experiments with rectangular RBC cells of larger aspect-ratios are reported before, e.g. Fitzjarrald (1976) and Ciliberto et al. (1996) report on (traversing) point measurements. However, to the author's knowledge, there is no detailed information in literature on the turbulent flow field in RBC cells with $\Gamma = 4$ at similar Rayleigh and Prandtl numbers. The focus of the present study is on the large-scale circulation (LSC), also known as "wind," and the origin of the low-frequency oscillation in this large-scale flow. It will be shown that the LSC in the

$\Gamma = 4$ cell shares certain characteristics with the $\Gamma = 1$ cell, but exciting, previously unknown differences occur as well.

6.2 Experimental set-up

The RBC results reported here have been obtained in a $600 \times 600 \times 155 \text{ mm}^3$ ($W \times W \times H$) cell filled with water. Two copper plates at the top and at the bottom are kept at a constant temperature by passing water through them from two basins containing constant temperature water. By doing so, the plates impose a controlled temperature difference on the working fluid. Experiments were conducted at a Rayleigh number $Ra = 5.9 \times 10^8$, corresponding to a temperature difference of $6.3 \text{ }^\circ\text{C}$. The mean temperature of the bulk fluid was approximately $30 \text{ }^\circ\text{C}$ corresponding to a Prandtl number $Pr = \nu/\kappa = 5.5$. Throughout this Chapter we will use a Cartesian coordinate system with its origin at the centre of the bottom wall. The x - and y -coordinates are measured along the bottom wall, parallel to the side walls of the RBC cell. The z -coordinate measures the wall-normal distance.

6.3 Measurement technique

Single-point measurements of the velocity were carried out by using a two-component LDA system manufactured by Dantec. The green (514.5 nm) and blue (488.0 nm) colours of a 5 W Argon-ion laser were used to measure two velocity components simultaneously. One beam of each colour was frequency pre-shifted by a Bragg cell to enable the detection of instantaneous flow reversals. The two beam pairs were oriented such that two wall parallel velocity components could be measured directly. Sometimes the optical configuration was changed such that the wall normal and a wall parallel velocity component were measured directly. The length and diameter of both measurement volumes are 0.8 mm and 0.1 mm, respectively, which is sufficiently small to resolve the smallest length scales of the flow. The light scattered by $5 \text{ }\mu\text{m}$ polyamide seed particles (Dantec) was collected in forward direction. The photomultiplier output signals were fed to two Dantec BSA signal processors to determine the instantaneous velocities. The LDA system measured the instantaneous velocities of the seed particles with an inaccuracy of 0.5%.

Velocity fields were measured by using a PIV system that included a Continuum Minilite double-pulsed Nd:YAG laser with a pulse energy of 25 mJ. This laser was used to make an approximately 1 mm thick light sheet that illuminated the seeding particles in the flow. Hollow glass spheres (Potters-Ballotini) with a diameter of approximately $10 \text{ }\mu\text{m}$ were used as seed particles. Two PCO Sensicam cameras with

a resolution of 1280×1024 pixels recorded images of the seed particles in the light sheet. A 28 mm focal length lens with a numerical aperture $f^\# = 4$ was mounted on each camera. The time separation between the two consecutive images was set to 25 ms. The image pairs were analysed in three subsequent steps using Gaussian local median filtering and interpolation for interrogation areas of 16×16 pixels. The resulting vector field covered the complete RBC cell with a resolution of 0.5×0.5 cm.

LDA measurements were taken at various points in the cell, but for brevity we present results only for one point at $x/W = 0.17$, $y = 0$, $z/H = 0.22$. At this point approximately 2.8×10^6 samples were taken at a mean rate of 16 Hz, resulting in a long measuring time of approximately 49 hours. The average of the velocity signal is -2.15 mm s^{-1} . A 2000 s long segment of the velocity time series for the wall-parallel velocity component is shown in Fig. 6.1. The graph indicates the presence of a large-scale quasi-periodic motion. This was investigated further by computing the spectral density function (sdf) for the entire time series, which is defined as the Fourier transform of the autocorrelation function $\rho(\tau) = \overline{u'(t)u'(t+\tau)}/\overline{u'^2}$, where $u'(t) (\equiv u(t) - \bar{u})$ is a fluctuating component of the turbulent velocity, t is time, τ is the time lag, and the overline denotes ensemble averaging. Computing the sdf from LDA velocity samples requires a special algorithm that takes into account the randomness of the sampling times and the velocity bias. In the present work the sdf was determined from the algorithm described by Tummers and Passchier (2001). The resulting sdf, shown in Fig. 6.2, indicates that the large scale motion has a periodicity of approximately 308 s. The inset in Fig. 6.2 shows that the oscillations in the autocorrelation function (acf) are maintained for a very long time with the amplitude varying irregularly as reported by Funkschilling and Ahlers (2004). From integration of the different parts of the measured sdf, one can determine the contribution of the periodicity to the total power of the velocity fluctuations. It is found that approximately 20% of the total power is due to the periodicity, which is consistent with the amplitude of the acf.

The periodic motion is a well known phenomenon in Rayleigh-Bénard convection for $Ra > 4 \times 10^7$. It has been reported in literature (see, for example, Castaing et al. (1989) or Qiu et al. (2000)) that the periodicity in RBC cells with an aspect ratio of about 1 is related to the formation of a LSC. The interaction between this LSC and the thermal plume formation is a topic of intense research, and, to the author's knowledge, this is the first time that a similar periodicity has been reported in a RBC cell with an aspect ratio 4.

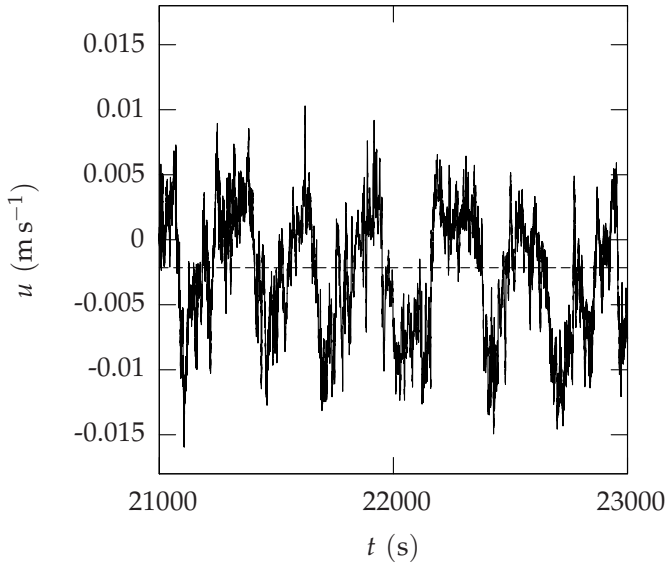


Figure 6.1: Wall-parallel velocity component u as a function of time. Dashed line indicates the average velocity.

6.4 Results

Inspired by the above observations the following questions arose. Is there a LSC in the aspect-ratio-four cell? If so, what form does it have? Furthermore, is there a relation between the LSC and the periodicity, and is this relation different from that in an aspect-ratio-one cell? To answer these questions we focused on the turbulent flow structures. Since it is difficult to study these flow structures from a single-point measurement technique (such as LDA), it was decided to deploy PIV. Our PIV system was used to collect a series of 3.0×10^4 snapshots of the velocity field in the x, z -plane at a rate of 1 Hz. The long-time mean flow field is shown in Fig. 6.3. Inspection of this mean flow field has resulted in the qualitative sketch of the streamline pattern that is shown in Fig. 6.4. There is a flow along the periphery of the cell that encloses two co-rotating rolls (centres) and a saddle point.

The LSC is “weak” in the sense that the long-time mean velocity is small compared to the magnitude of the instantaneous velocity fluctuations, as can be readily observed from Fig. 6.1. Note that this is in contrast to the situation in an aspect-ratio-one cell where the LSC can be so strong that the instantaneous velocity only seldom changes sign (Shang et al., 2003). As a consequence of the weak circulation, the mean flow field shown in Fig. 6.3 cannot be observed from the instantaneous PIV snapshots. It

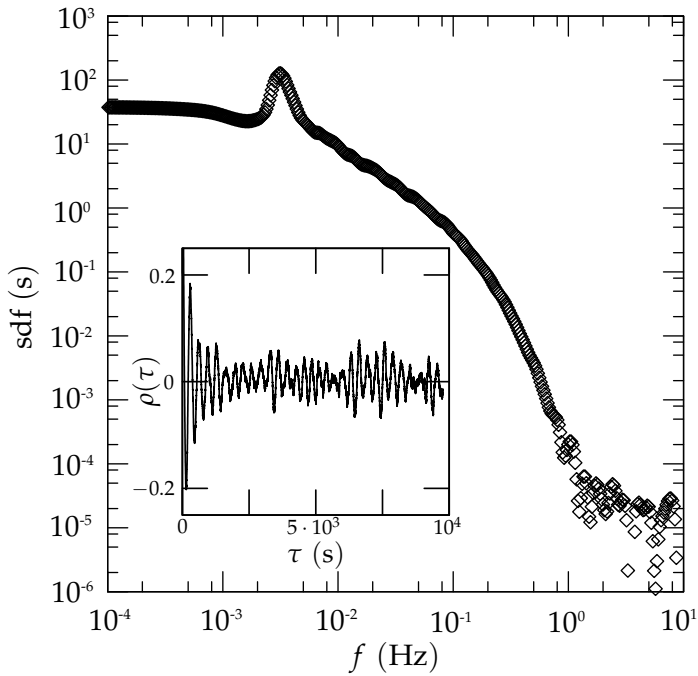


Figure 6.2: Spectral density function of the velocity component in x -direction measured at $x/W = 0.17, y = 0, z/H = 0.22$. Inset: autocorrelation function for the same position.

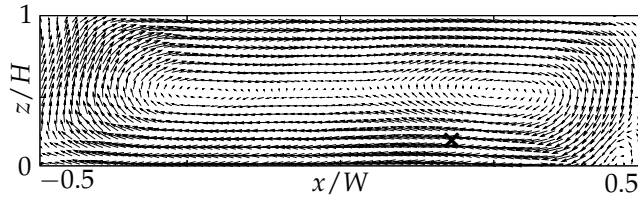


Figure 6.3: Mean flow field in the x, z -plane. The cross at $x/W = 0.17, z/H = 0.22$ indicates the LDA position.

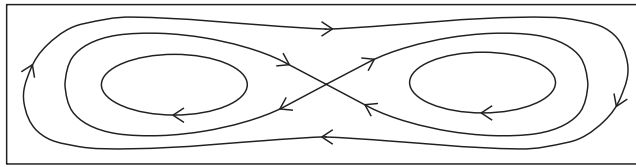


Figure 6.4: Sketch of the mean flow field in the $\Gamma = 4$ cell.

emerges only after averaging over a very long time.

For each PIV interrogation area one can extract a velocity time series from the PIV measurements. Clearly, the velocity samples in these time series are taken at regular intervals of 1 s, and standard data processing methods can be applied to compute the sdf. It was checked that the peak in the sdfs determined from the PIV time series was the same as that determined from the LDA data. Moreover, the sdfs determined from the PIV time series extracted at various locations in the RBC cell showed conclusively that the period of the oscillation was the same everywhere, thus proving that the oscillation is a global phenomenon.

From flow and temperature visualisations using thermochromic liquid crystal tracers, we have observed that groups of plumes tend to move along the side walls of the RBC cell, not dissimilar to what has been reported by Qiu et al. (2000) for aspect-ratio-one cells. They suggested that the buoyancy forces exerted on groups of plumes that rise or fall along the side walls is what drives the LSC. We find the same mechanism at work in the present RBC cell, but there are also interesting differences. As mentioned before, the LSC is weak in the present RBC cell, and plumes that are released from the horizontal walls are not strongly sheared. As a consequence, not all the plumes are carried towards the side walls before they move up (or down). The weak circulation allows the plumes to be released from the thermal boundary layers on the horizontal walls and move up (or down) long before reaching the side walls. We did not observe individual plumes reaching the opposite wall by traversing the turbulent core, but groups of plumes regularly form temporary pathways between the horizontal plates. The location, size and orientation of these pathways are not steady. Their lifetimes are of the same order of magnitude as the period of

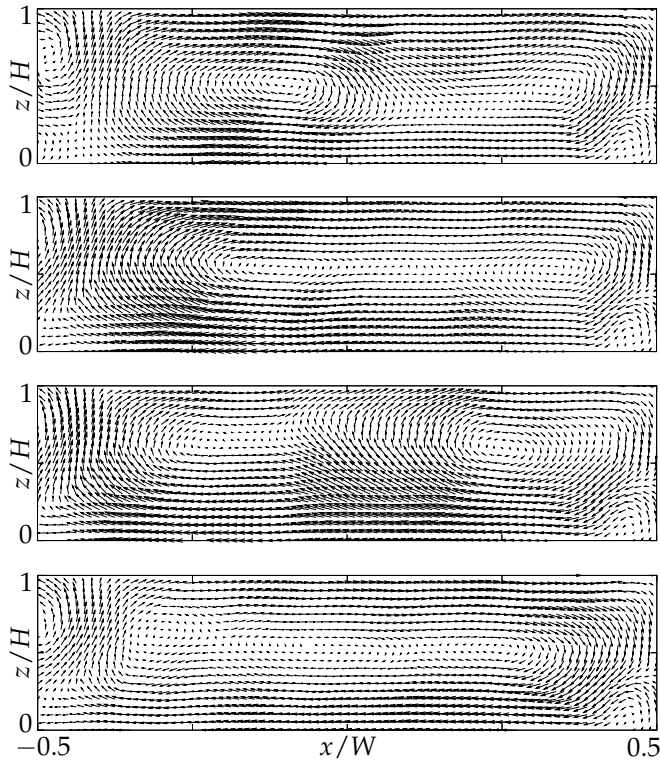


Figure 6.5: Phase resolved velocity fields for $N = 4$.

the oscillations, but generally shorter. It is speculated here that the two co-rotating rolls in the long-time mean flow field in Fig. 6.3 occur due to the formation of these pathways at preferential locations. In other words, one cannot predict when and where a pathway is formed, nor can one predict its size, strength and duration, but the long-time mean flow indicates that the pathways have a preferred location near the centre of the cell.

For the aspect-ratio-one cell, Villermaux (1995) proposed that the interaction between the thermal boundary layers on the upper and lower wall depends on the delay time H/U where U is the large scale velocity. Qiu et al. (2004) modified this view slightly by pointing out that U is actually a fluctuating quantity, but in essence, the oscillations observed in the $\Gamma = 1$ cell are proportional to U/H , so that a physical picture arises with alternating eruptions of groups of plumes from the thermal boundary layers. These groups move up or down in opposing side wall regions thus driving a LSC that takes the form of a single roll.

To determine a relation between the LSC, the plume motion and the low-frequency

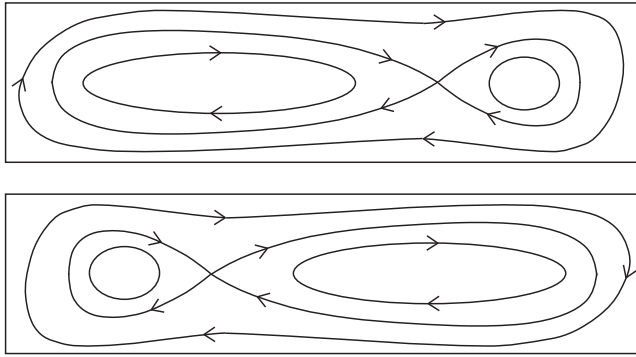


Figure 6.6: Sketch of two extreme states of the LSC with half a period phase difference.

oscillation for the present aspect-ratio-four cell, we decided to resolve the instantaneous velocity fields (i.e., the PIV snapshots) into phases. Phase-resolved velocity fields were determined as follows. The series of 3×10^4 instantaneous velocity fields was split into segments of 308 sequential snapshots thus matching the measured period. Each segment was subsequently divided into N intervals of equal length. The phase-resolved mean velocity field for the i -th phase followed from the mean of all snapshots in the i -th interval in each of the segments. Figure 6.5 shows the phase-resolved velocity fields for $N = 4$. In phase 1 (top insert) one can observe the saddle point and the two rolls with the left roll being much stronger than the right roll. The flow is along the circumference of the RBC cell, but there is also a tendency for the fluid to cross the cell along a “descending diagonal” located on the right-hand side of the strongest roll. During phase 2 the fluid no longer descends along this “diagonal,” but most of the momentum is still concentrated on the left-hand side of the RBC cell in the remnant of the left roll. A strengthening of the right roll sets in, and, during phase 3 fluid moves along the circumference and it can cross the RBC cell along an “ascending diagonal” on the left-hand side of the right roll. During phase 4 the right roll loses its strength, and the process repeats itself. The driving mechanism for the LSC are the buoyancy forces exerted on groups of plumes that move up (or down) in regions that are separated laterally, effectively providing a torque. These groups of ascending (or descending) plumes occur at two locations: (1) near the sidewalls as in the aspect-ratio-one cell, and (2) at “random” locations away from the sidewalls. The latter provides an additional channel for the transport of heat between the two horizontal plates that does not occur in the aspect-ratio-one cell. Although the exact location of these channels cannot be predicted, they appear to occur most frequently around the half width of the cell, thus forming “short” rolls with lateral size of about $2.5H$ that alternately appear on the left or on the right of the cell.

6.5 Conclusion

In summary, the experiments reveal that the LSC in the aspect-ratio-four RBC cell consists of a flow around the periphery that encloses two co-rotating rolls. Using a phase resolving technique, it is shown that the growth and decay of the rolls produce a well-defined period that is maintained for a very long time. Figure 6.6 sketches two extremes in the temporal evolution of the LSC that have a phase difference of half a period thus illustrating the nature of the oscillation in the aspect-ratio-four cell.

7

Spectral analysis of boundary layers in Rayleigh-Bénard convection

A combined experimental and numerical study of the boundary layer in a 4:1 aspect-ratio Rayleigh-Bénard cell over a four-decade range of Rayleigh numbers has been undertaken aimed at gaining a better insight into the character of the boundary layers. The experiments involved the simultaneous laser Doppler anemometry (LDA) measurements of fluid velocity at two locations, i.e. in the boundary layer and far away from it in the bulk, for Rayleigh numbers varying between 1.6×10^7 and 2.4×10^9 . In parallel, direct numerical simulations (DNS) have been performed for the same configuration for Rayleigh numbers between 7.0×10^4 and 7.7×10^7 . The temperature and velocity probability density functions and the power spectra of the horizontal velocity fluctuations measured in the boundary layer and in the bulk flow are found to be practically identical. Except for the smallest Rayleigh numbers, the spectra in the boundary layer and in the bulk central region are continuous and have a wide range of active scales. This indicates that both the bulk and the boundary layers are turbulent in the Ra number range considered. However, molecular effects can still be observed and the boundary layer does not behave like a classical shear-driven turbulent boundary layer.

7.1 Introduction

Rayleigh-Bénard (RB) convection in a fluid trapped between two horizontal plates of unequal temperature with the bottom wall being warmer than the top wall, has long served as a paradigm of thermal convection. Despite numerous studies (see e.g. overviews by Siggia (1994); Kadanoff (2001)), it continues to pose challenges because of a number of still unresolved and controversial issues. We recall that RB convection is characterised by the Rayleigh number $Ra = \alpha g \Delta T H^3 / (\nu \kappa)$, and the Prandtl number $Pr = \nu / \kappa$, where α is the thermal expansion coefficient, ΔT is the temperature difference between the cold and the hot plate, H is the vertical distance between the plates, ν is the kinematic viscosity, and κ is the thermal diffusivity. In practical RB set-ups the lateral size, W , of the plates is finite. This is taken into account by a third dimensionless number known as the aspect ratio $\Gamma = W/H$.

A topic of intense debate is the scaling law for the dimensionless heat transfer, $Nu \sim Ra^\gamma$, especially for the range $Ra > 10^7$ (Niemela et al., 2000). Here Nu is the Nusselt number $Nu = hH/\lambda = -H/(\Delta T)\partial\bar{T}/\partial z|_{\text{wall}}$, h stands for the convective heat transfer coefficient, λ is the thermal conductivity, and \bar{T} is the averaged temperature. Heslot et al. (1987), Castaing et al. (1989) and Wu et al. (1990) proposed scaling laws for the heat transfer and temperature statistics in RB convection, which differed from the classical theories, such as that of Howard (1963). In the search for general scaling behaviour, Grossmann and Lohse (2000) presented a unifying theory dividing the Ra, Pr plane into several regions, each with different scaling. Crucial assumptions in this theory are the existence of a large-scale circulation, also known as the wind, and a Blasius type laminar boundary layer. The assumption that the boundary layers of Rayleigh-Bénard convection behave as a laminar Blasius boundary layer is supported by several observations: (i) the scaling of the friction factor C_f is compatible with that of a laminar boundary layer past a flat plate at moderate Ra (Chavanne et al., 1997, 2001; Amati et al., 2005); (ii) the typical Reynolds number Re of the flow is low at moderate Ra : for water $Re \approx 200$ at $Ra = 10^7$ and $\Gamma = 4$, which is generally accepted to be too low to sustain turbulence. Grossmann and Lohse (2000) argued that at large enough Ra this laminar boundary layer breaks down and becomes turbulent, presuming that the transition to a turbulent boundary layer is shear triggered. The critical Ra number for this transition was estimated to be in the order of 10^{14} for $Pr = 1$.

Despite this apparently convincing evidence, it is not clear how a boundary layer which is highly unsteady due to continuous plume impingement and detachment can behave quantitatively as a laminar boundary layer. This would indicate that the plumes only cause unsteady disturbances and a consequent time-dependence in the boundary layer, but are passive otherwise.

The aim of this Chapter is to enhance the understanding of the boundary-layer dy-

namics by comparing velocity statistics in the boundary layer with those determined in the bulk. It has widely been regarded that the main prerequisite for unsteady velocity fluctuations to be qualified as turbulence, in contrast to other uncorrelated, chaotic and random fluctuations, is a power spectrum that is continuous over a wide range of scales. For this reason we focused on the analysis of spectral density functions (sdf), complemented with probability density functions (pdf), aimed at clarifying the nature of the fluctuations in the boundary layer. For this purpose we use in parallel complementary numerical and experimental techniques: direct numerical simulations (DNS) are performed for the lower Ra values, laser Doppler anemometry (LDA) measurements are conducted for the medium and higher Ra values. All experiments and simulations combined cover a Ra range between 7.0×10^4 and 2.4×10^9 . In the midrange both techniques overlap over about one decade.

7.2 Methodology

7.2.1 Experiments

The experiments were conducted in a $600 \times 600 \times 155 \text{ mm}^3$ ($W \times W \times H$) cell filled with water (described in more detail in Chapter 6). In brief, two copper plates at the top and bottom are kept at a constant temperature by passing water through the plates' internal channels, drawn from two basins containing constant temperature water (inaccuracy less than 0.03 K). The plates thus impose a controlled temperature difference ΔT on the working fluid. Throughout this paper we will use a Cartesian coordinate system with its origin at the centre of the bottom wall, Fig. 7.1. The x - and y -coordinates are measured along the bottom wall, parallel to the side walls of the RB cell. The z -coordinate measures the wall normal distance.

Velocities were measured by using two one-component laser Doppler anemometers manufactured by Dantec. The green (514.5 nm) and blue (488.0 nm) colours of a 5 W Argon-ion laser are used to simultaneously measure the horizontal component in the x -direction in the bulk and in the boundary layer. The measured velocity component is in the direction of the large-scale circulation. To enable the detection of instantaneous flow reversals one beam of each colour was frequency pre-shifted by a Bragg cell. The light scattered by $5 \mu\text{m}$ polyamide seed particles was collected in on-axis forward direction, which, in comparison to back-scatter, results in a superior signal-to-noise ratio of the Doppler signals. The photomultiplier output signals were first downmixed electronically to an effective pre-shift of 30 kHz and then fed to two Dantec BSA signal processors to determine the instantaneous velocities. The LDA system measured the instantaneous velocities of the seed particles with an inaccuracy of 0.5%. The length and diameter of both measurement volumes are 0.8 mm and 0.1 mm, respectively, which is sufficiently small to resolve the smallest length scales

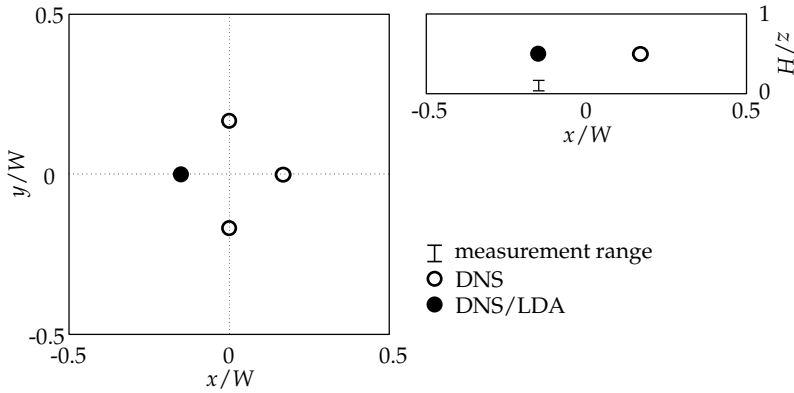


Figure 7.1: Schematic of the measurement points in the RB cell for both DNS and LDA measurements.

Ra	Pr	ΔT (K)	\bar{T} ($^{\circ}\text{C}$)	α (K^{-1})	ν ($\text{m}^2 \text{s}^{-1}$)	\mathcal{T} (s)
1.6×10^7	9.4	0.92	10.2	8.8×10^{-5}	1.3×10^{-6}	1.1×10^5
8.2×10^7	7.0	1.57	19.9	2.1×10^{-4}	1.0×10^{-6}	0.9×10^5
4.2×10^8	5.5	6.52	30.0	3.0×10^{-4}	8.0×10^{-7}	1.2×10^5
2.4×10^9	5.5	25.1	30.3	3.0×10^{-4}	8.0×10^{-7}	1.3×10^5

Table 7.1: Experimental details for the LDA measurements. All experiments have been performed in a $\Gamma = 4$ aspect ratio domain. \mathcal{T} denotes the measurement time.

of the flow. For each Ra number, the measurement time \mathcal{T} was at least 20 hours to have sufficient data for an accurate statistical description of the flow.

The mean data rate varied between 10 Hz and 30 Hz, depending on Ra and distance from the wall. For moderate Ra numbers, the relatively low characteristic velocities result in a relatively low data rate. Measurement locations close to the wall have an inherently low data rate due to the low fluid volume flux.

Table 7.1 shows the experimental parameters as well as the relevant non-dimensional numbers. The Rayleigh number is varied by changing the temperature difference ΔT between the bottom and top plates from nearly 1 K at $\text{Ra} = 1.6 \times 10^7$ to 25 K at $\text{Ra} = 2.4 \times 10^9$. For the highest Ra numbers, the relatively large temperature differences cause larger density differences, but these remain small enough to neglect non-Boussinesq effects. The Prandtl number will change as well, but the ratio between the smallest and largest Pr number is only 1.7.

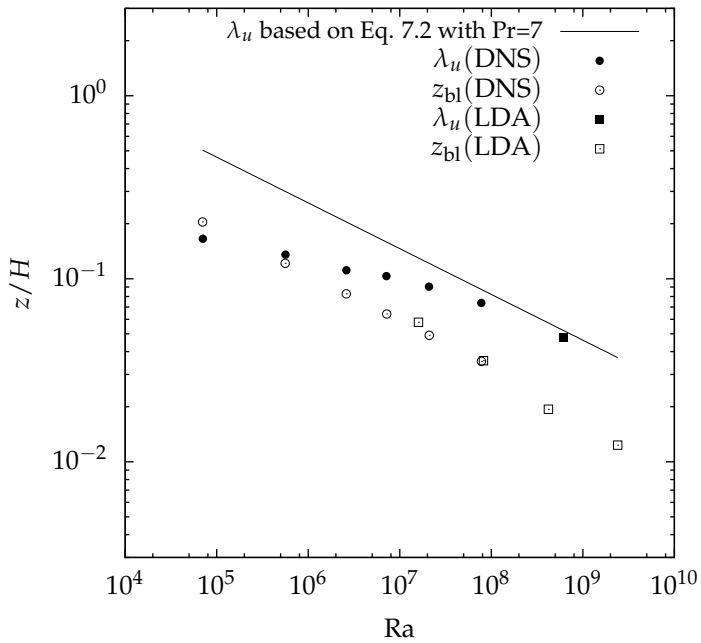


Figure 7.2: Kinematic boundary-layer height λ_u , based on Equation 7.2 as well as from DNS, and the measurement locations, z_{bl} , as function of Ra .

7.2.2 Simulations

The direct numerical simulations cover the lower to moderate Ra number range between $Ra = 7.0 \times 10^4$ and $Ra = 7.7 \times 10^7$. The numerics are based on staggered finite differences, with a central second order scheme for advection, and a second order Adams-Bashforth time integration scheme. To effectively resolve the boundary layers, grid stretching in the wall-normal direction has been implemented, and special care has been taken to preserve the skew-symmetry of the advective operator (Verstappen and Veldman, 2003). The code, as reported in van Reeuwijk (2007), has been extended to support sidewalls. In the situation without sidewalls, the Poisson equation is Fourier-transformed in the two homogeneous directions. As a result, the Poisson equation decouples for these directions, and the pressure amplitudes can be solved per component by solving a tridiagonal system in the wall-normal direction. To incorporate sidewalls, the Fourier-transform was replaced by a cosine transform, which automatically satisfies a Neumann boundary condition for pressure. The sidewall boundary conditions for the velocity and temperature could be enforced directly due to the explicit time-integration.

Dirichlet boundary conditions are applied at the top and bottom plate, i.e. no-slip and isothermal boundary conditions for velocity and temperature, respectively. On the sidewalls, Neumann boundary conditions are applied for both temperature and velocity, i.e. free-slip and insulating walls for velocity and temperature. The free-slip (stress free) velocity boundary conditions were used to avoid having to resolve the boundary layer at the sidewalls. Although this changes the flow physics near the sidewalls, its global effect is limited for large aspect ratio domains, as preliminary simulations showed. Neumann boundary conditions were applied for pressure at all boundaries.

In the simulations, the properties of water are used except that $Pr = 7$ is kept fixed for all Ra. The grid resolution (Table 7.2) is sufficient to resolve the smallest turbulent scales, i.e. the Kolmogorov scale $\eta_K = (v^3/\varepsilon)^{1/4}$ and the Corrsin scale $\eta_C = Pr^{-1/2} \eta_K$. At $Pr = 7$, the Corrsin scale dominates the grid requirements, and the resolution roughly corresponds to $\Delta x \approx \Delta y \approx \Delta z \approx 4\eta_C$. To resolve the boundary layers at the top and bottom wall properly, grid stretching has been applied in the wall-normal direction, such that at least eight points are within the thermal boundary layer. It should be noted that the simulation at the highest Ra number ($= 7.7 \times 10^7$) may be slightly under-resolved in the horizontal directions. High quality simulations as reported in Hanjalić (2005) at $Ra = 10^8$ and $Pr = 7$ required 768 points per horizontal direction, but reduction to 384 points was the only way to simulate over a sufficiently long time interval to obtain reliable one-point statistics required for the comparison with the experiments. The additional information shown in Table 7.2 are the dimensionless timestep t/t^* , the number of simulated turnovers \mathcal{T}/t^* and the average Nusselt number Nu. The typical convective turnover time

Ra	grid	$\Delta t/t^*$	\mathcal{T}/t^*	Nu
7.0×10^4	$64^2 \times 48$	4.0×10^{-4}	240	3.8
5.6×10^5	$96^2 \times 64$	2.3×10^{-4}	140	7.2
2.6×10^6	$128^2 \times 92$	1.7×10^{-4}	165	11.3
7.2×10^6	$192^2 \times 128$	1.3×10^{-4}	155	15.2
2.1×10^7	$384^2 \times 160$	1.0×10^{-4}	40	20.0
7.7×10^7	$384^2 \times 160$	1.0×10^{-4}	30	30.0

Table 7.2: Simulation details for DNS.

$t^* \equiv H/U$ with U the typical velocity based on the free fall scaling. The average Nusselt number is calculated as $\text{Nu} = -H/(\Delta T) \partial \bar{T}/\partial z|_{\text{wall}}$, with \bar{T} averaged over the entire bottom surface and over many turnovers.

7.2.3 Measurement locations

Simultaneous measurements have been performed in the boundary layer and in the bulk of the cell for various Ra. The measurement location in the bulk is at $x_{\text{bulk}} = W/3$, $y_{\text{bulk}} = W/2$ with a fixed wall distance $z_{\text{bulk}} = H/2$, see Fig. 7.1. The measurement location in the boundary layer has the same x - and y -coordinates, but the wall distance is different, i.e., $z_{\text{bl}} = 0.4\lambda_u$, where λ_u is the kinematic boundary layer thickness determined as in Grossmann and Lohse (2000):

$$\lambda_u = H/\sqrt{\text{Re}}. \quad (7.1)$$

In this expression for λ_u the Reynolds number, Re, was taken from Grossmann and Lohse (2000, 2001):

$$\text{Re} = 0.073\text{Ra}^{1/2}\text{Pr}^{-5/6}. \quad (7.2)$$

Table 7.3 lists the physical measurement locations, where the DNS values have been rescaled to $H = 155$ mm. Figure 7.2 shows that the wall distance for the boundary layer measurements slightly deviates from linear behaviour (on a double-log plot) due to minor changes in Pr for the experimental points. In separate experiments, LDA was used to determine mean-velocity and rms-velocity profiles above the wall (at $\text{Ra} \approx 8.0 \times 10^8$). The results of these experiments confirmed that the measurement locations at $z = z_{\text{bl}}$ were all located in the boundary layer for the full Ra number range considered in this study. The DNS values for λ_u , denoted by solid circles in

	Ra	Pr	Re	λ_u/H	z_{bl}/H
DNS	7.0×10^4	7.0	3.8	0.512	0.204
	5.6×10^5	7.0	11	0.305	0.121
	2.6×10^6	7.0	23	0.207	0.0827
	7.2×10^6	7.0	39	0.161	0.0641
	2.1×10^7	7.0	66	0.123	0.0490
	7.7×10^7	7.0	1.3×10^2	0.0884	0.0354
LDA	1.6×10^7	9.4	48	0.145	0.0578
	8.2×10^7	7.0	1.2×10^2	0.0897	0.0357
	4.2×10^8	5.5	4.2×10^2	0.0485	0.0193
	2.4×10^9	5.5	1.0×10^3	0.0309	0.0123

Table 7.3: Measurement heights for the different Ra experiments. The Re number is based on Equation 7.2.

Fig. 7.2, support this observation. Clearly, Eq. 7.1 overestimates the scaling exponent of λ_u , so that the prefactor α in the BL measurement points $z_{bl} = \alpha\lambda_u$ is a decreasing function of Ra. Hence, as Ra increases, the measurements are performed deeper into the kinematic boundary layer. The disparity between the theoretical prediction (Eq. 7.1) and the measurements for λ_u will be discussed in more detail at the end of section 7.3.2.

The DNS time series are short in respect to the LDA series. To enable a comparison between LDA and DNS results, the DNS data are extracted from four points in the domain. These points are symmetrically placed around the origin with horizontal coordinates $(\pm W/6, 0)$, $(0, \pm W/6)$, as shown in Fig. 7.1. The four obtained time series are regarded as nearly statistically independent, and are then averaged to effectively improve the statistics of the DNS time series.

7.3 Results

7.3.1 Probability density functions

Figure 7.3 shows the measured and computed variance of the horizontal velocity σ_u^2 in the boundary layer and in the bulk. The graph shows that for increasing Ra there is a gradual transition of the variances between DNS and LDA results giving confidence in the procedure followed.

Temperature pdfs obtained from DNS for the boundary layer and the bulk are depicted in Figure 7.4(b) and show an exponential distribution even for $Ra = 5.6 \times 10^5$.

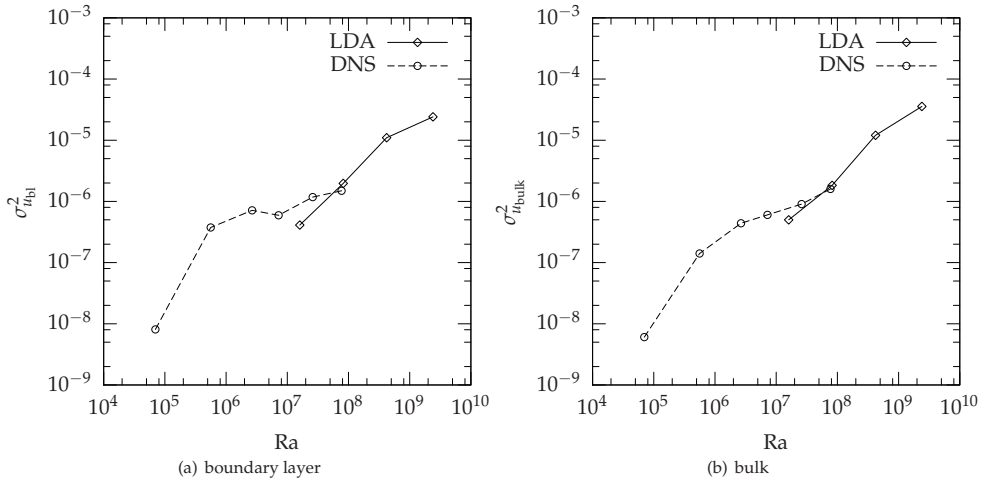


Figure 7.3: Variances of the horizontal velocity component, u , in the boundary layer (a) and in the bulk (b).

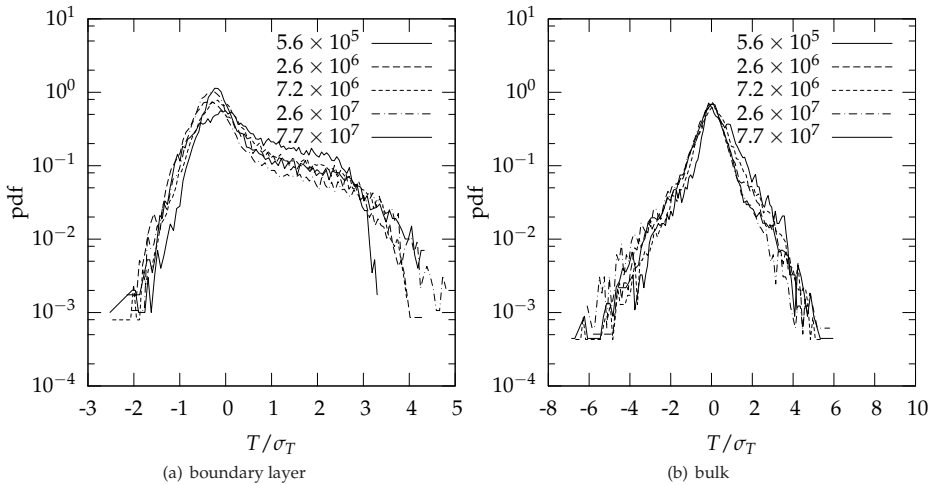
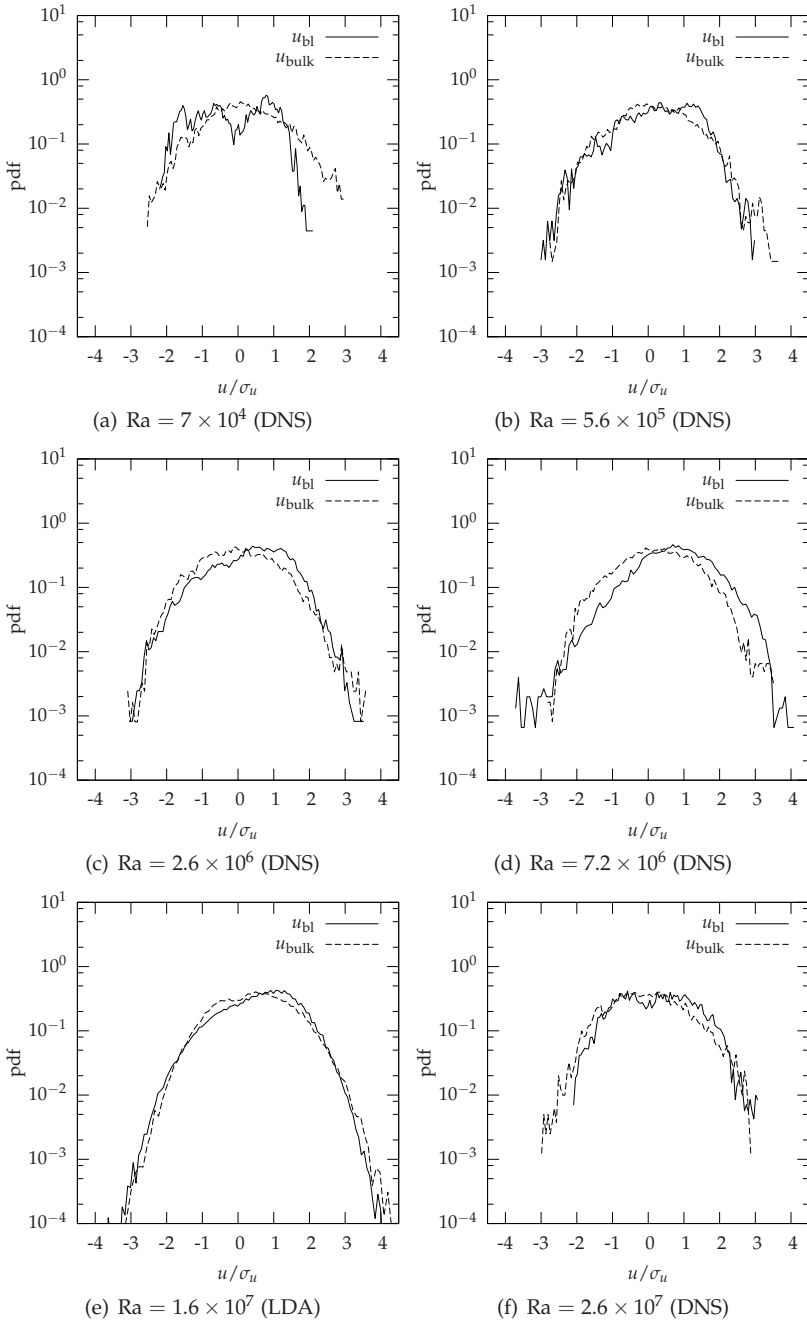


Figure 7.4: Probability density functions for temperature T in the boundary layer (a) and in the bulk (b) of the RB cell obtained from DNS. Histograms are scaled with their rms value σ_T .



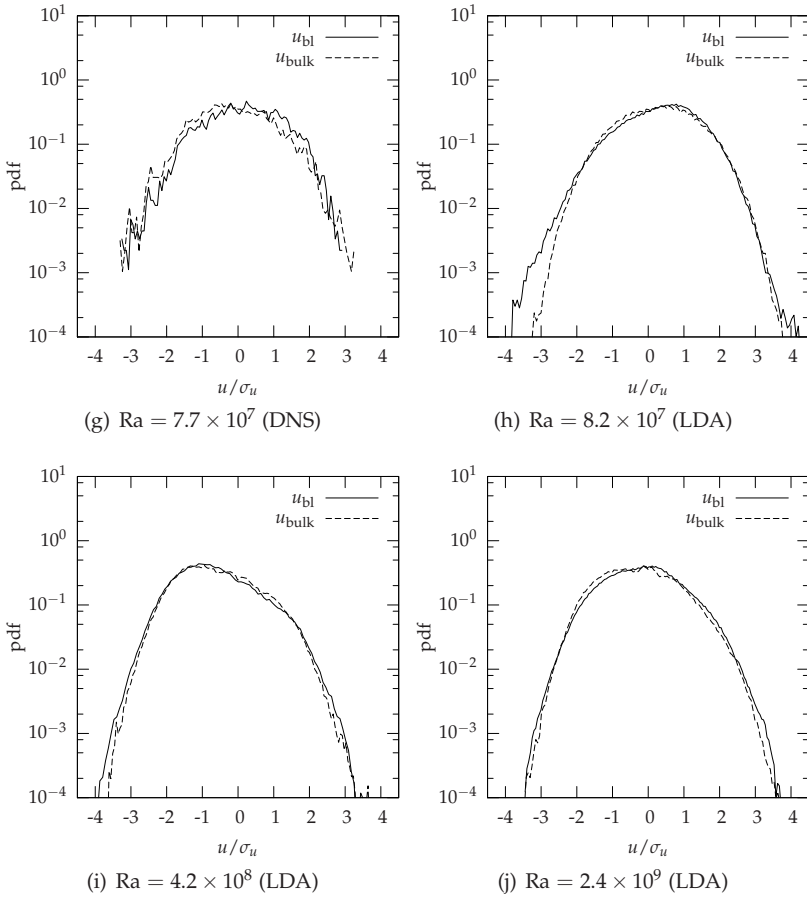


Figure 7.5: Probability density functions of the u horizontal velocity component in the boundary layer (bl) and in the bulk of the RB cell. Histograms are scaled with their rms value σ_u . The source of the data, DNS or LDA, is indicated.

The straight lines (on logarithmic scale) are generally associated with the hard turbulent regime, which sets in at $Ra = 4 \times 10^7$ for aspect-ratio-1 cells (e.g. Heslot et al. (1987); Castaing et al. (1989); Qiu and Tong (2001)). Recall that the transition between soft and hard turbulence takes place at relatively low Ra number in the aspect-ratio-4 cell, see Kerr (1996). The boundary layer pdf is skewed towards positive temperatures. This is generally attributed to the interaction of thermal plumes with the flow. Plumes leaving the boundary layer result in positive temperature excursions.

Figure 7.5 depicts the probability density functions (pdfs) of the computed and measured u component. As expected, the pdfs of both horizontal velocity components were found to have the same shape in the simulations. For brevity only the u component is therefore depicted in Figure 7.5. For a better comparison, the pdfs are scaled with the rms value σ_u . The results show that the pdfs in both the boundary layer and in the bulk exhibit a nearly Gaussian-like shape for the complete Ra number range. Only the pdfs at $Ra = 7 \times 10^4$ deviate largely from this trend, mainly due to the presence of a strong oscillatory component in the velocity time series, as will be shown later when discussing the power spectra.

Vincent and Meneguzzi (1991) and Mouri et al. (2002) make a distinction between sub-Gaussian, Gaussian and hyper-Gaussian stages in the development of turbulence. They argue that the nearly Gaussian shape of the pdfs in the present study indicates that turbulence is in a fully developed stage. The pdfs for the highest Ra values have non-zero mean values. This is caused by the large-scale circulation or “wind” within the RB cell. For $Ra = 4.2 \times 10^8$ the mean value is approximately 5 mm s^{-1} . The wind is rather weak in the sense that its mean value is small compared to the magnitude of the rms velocity fluctuations, in accordance with other findings. (van Reeuwijk et al., 2005; Verdoold et al., 2006a; Niemela and Sreenivasan, 2006; van Reeuwijk et al., 2008a). It is also observed that the wind is not always in the same direction. In some experiments (Fig. 7.5(h)) it appears to be clockwise, while in others (Figs. 7.5(i), (j)) it is counterclockwise.

7.3.2 Spectral density functions

The obtained velocity time series are investigated further by computing the spectral density function (sdf). The sdf is defined as the Fourier transform of the autocorrelation function $\rho(\tau) = \overline{u'(t)u'(t+\tau)}/\overline{u'^2}$, where $u'(t) (\equiv u(t) - \bar{u})$ is the fluctuating component of the turbulent velocity, t is time, τ is the time lag, and the overline denotes ensemble averaging. All sdfs are calculated using the same algorithm, to make a fair comparison for both DNS and LDA data. This algorithm, described in Tummers and Passchier (2001), can account for the randomness of the sampling times in LDA measurements.

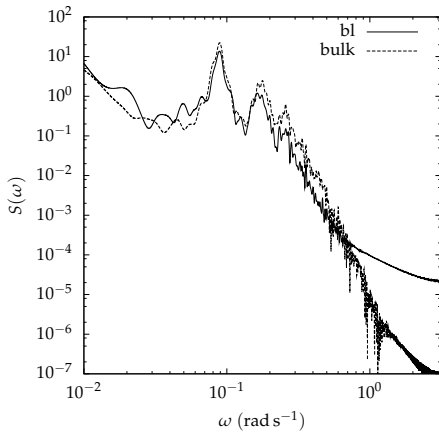
Figure 7.6 shows the sdfs of the horizontal component in the x -direction determined in the boundary layer and in the bulk for the full range of Ra considered in this study. The sdfs determined from DNS data are accurate at high frequencies, but less reliable in the low frequency range due to the relatively small measurement times. In contrast, the low frequency region in the LDA sdfs is accurate, while the high frequency range suffers from a relatively high statistical scatter caused by the random sampling process in LDA. The level of the statistical scatter (which strongly depends on the mean data rate) sets a lower limit to the spectral density that can be accurately determined from LDA data.

When comparing the various sdfs in Figure 7.6, it is clear that the sdf for $Ra = 7 \times 10^4$ is different from all others. At this low Ra numbers, the flow is not turbulent but in a state of spatio-temporal chaos. As mentioned earlier, the velocity time series is characterised by strong oscillations. As a consequence, the sdf in Fig. 7.6(a) (and to a lesser extent the sdf in Fig. 7.6(b)) is dominated by a limited number of discrete peaks and the sdf rolls off rapidly at higher frequencies.

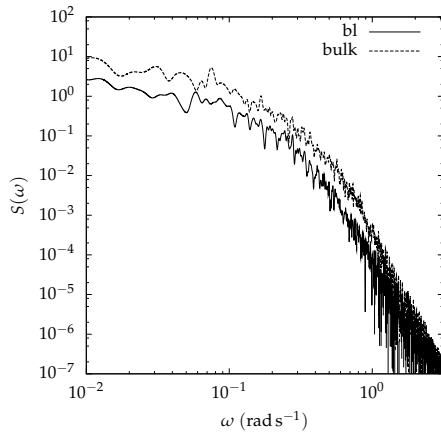
Peaks in the sdf also occur in the very low frequency range in Figs. 7.6(i) and 7.6(j). The peak frequencies ω_p correspond to periods of $2\pi/\omega_p = 283$ s and 172 s at $Ra = 4.2 \times 10^8$ and $Ra = 2.4 \times 10^9$, respectively. These oscillations are unrelated to the ones observed at low Ra , and have their origin in the alternating growth and decay of rolls that form the large scale circulation as discussed in Chapter 6.

For $Ra > 2.6 \times 10^6$ all sdfs measured in the bulk have a wide range of active scales, and this range increases with Ra . These sdfs are continuous, and are not dominated by a small number of frequencies as one might expect in spatio-temporal chaos. Clearly these sdfs indicate that the bulk in the RB cell is turbulent for $Ra > 2.6 \times 10^6$. Although an inertial subrange is absent for the measurements at lower Ra , the sdf at $Ra = 2.4 \times 10^9$ (Fig. 7.6(j)) shows an inertial subrange spanning roughly one decade. Note that the presence of an inertial subrange is not a necessary condition for turbulence. An inertial subrange can only form when there is a range of scales which is neither influenced by macro- or micro-scales, i.e. at high Re when the production and dissipation scales are sufficiently separated. Therefore, an inertial subrange is absent despite the turbulence at lower Re (see also Wu et al., 1990; Camussi and Verzicco, 1998).

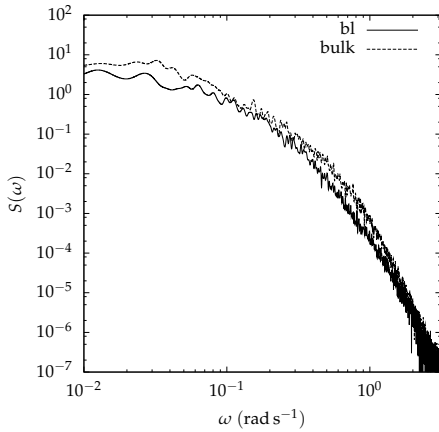
The most striking observation is that the sdfs in the bulk and in the boundary layer are practically identical for $Ra > 2.6 \times 10^6$. As the sdfs for the bulk indicate that the flow is turbulent, one cannot escape from the conclusion that the flow in the boundary layers must also be characterised as turbulent. It is difficult to reconcile this observation with the conceptual image of a laminar, Blasius-type boundary layer along the walls of the RB cell. For a Blasius boundary layer, the laminar-turbulent transition occurs at a relatively high Reynolds number, i.e., $Re_c^* \approx 10^5 - 10^6$ depend-



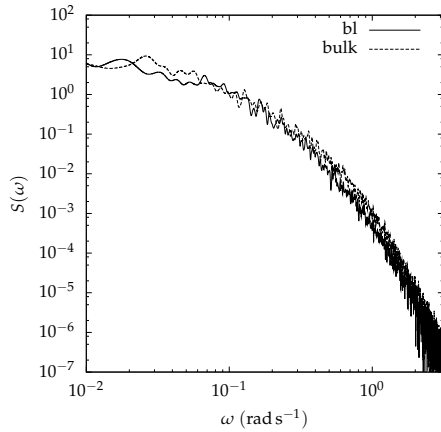
(a) $Ra = 7 \times 10^4$ (DNS)



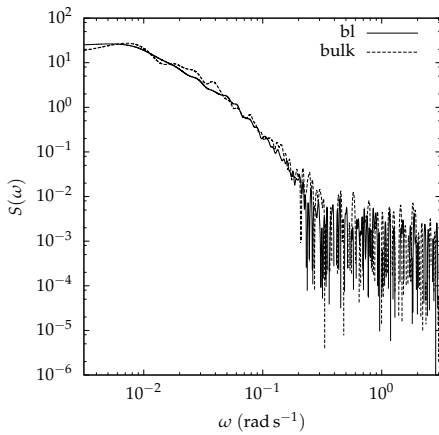
(b) $Ra = 5.6 \times 10^5$ (DNS)



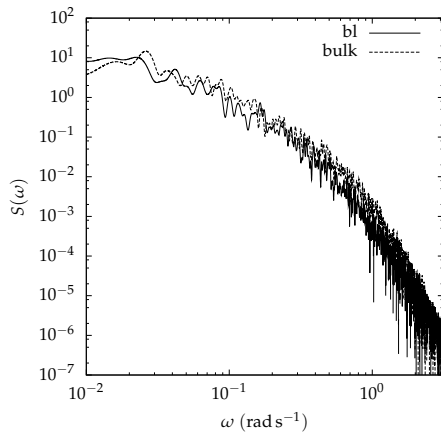
(c) $Ra = 2.6 \times 10^6$ (DNS)



(d) $Ra = 7.2 \times 10^6$ (DNS)



(e) $Ra = 1.6 \times 10^7$ (LDA)



(f) $Ra = 2.6 \times 10^7$ (DNS)

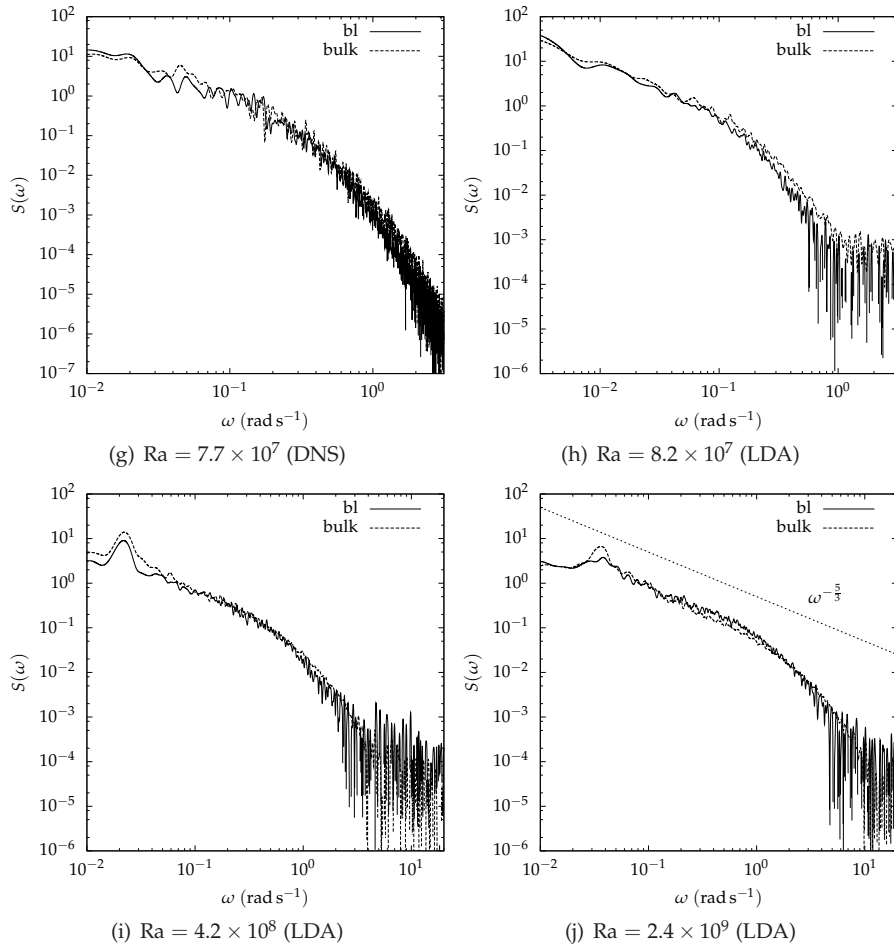


Figure 7.6: Spectral density functions for the horizontal velocity component u for points in the boundary layer (bl) and in the bulk of the RB cell. Ra ranging from 7.0×10^4 to 2.4×10^9 . The source of the data, DNS or LDA, is indicated.

ing on the intensity and nature of disturbances in the flow (Schlichting and Gersten, 1997). Here, Re_c^* is a Reynolds number based on plate length and outer velocity. However, even at the highest Ra considered in this study, the value of Re^* based on the cell width and the wind velocity is only 3×10^3 , which is far below the critical value for laminar-turbulent transition in a flat plate boundary layer. Thus, the turbulence in the boundary layer cannot be due to a shear-triggered transition (occurring inside the boundary layer), but more likely due to the impingement and detachment of plumes (travelling into and out of the boundary layer), which is corroborated by the great similarity between the bulk and the boundary-layer spectra.

Naturally, one can always envision that the boundary layer only *quantitatively* behaves as a laminar Blasius boundary layer: the plumes introduce a time-dependence on time-scales that prevent pure laminarity. The underlying assumption is that on the average, the thermals and plumes are passive when it comes to scaling of various important integral parameters of the kinematic boundary layer such as the friction factor C_f and the boundary layer thickness λ_u . Indeed, C_f scales as $C_f \propto Re^{-1/2}$, as one would expect for a laminar boundary layer past a flat plate at moderate Ra (Chavanne et al., 1997, 2001; Amati et al., 2005; van Reeuwijk et al., 2008b).

The scaling of the boundary layer thickness λ_u is slightly more complicated. Assuming a laminar boundary layer, λ_u scales as $\lambda_u \propto Re^{-1/2}$ (Schlichting and Gersten, 1997), which is related to Ra as $\lambda_u \propto Ra^{-1/4}$ upon assuming $Re \propto Ra^{1/2}$. Experiments show that a scaling exponent of -0.25 holds well for the boundary layer thickness of the sidewalls (Qiu and Xia, 1998b), but not for the scaling of the bottom and top boundary layers (Qiu and Xia, 1998a; Kerr, 1996; van Reeuwijk et al., 2008b) which scales with exponents from -0.11 to -0.16 . The simulations in this paper confirm the weak Ra number dependence of λ_u (Fig. 7.2). This disparity indicates that plumes impinging on and emerging from the boundary layer are not entirely passive, but actively influence the boundary layer thickness. Given the important role of λ_u in the theory of Grossmann and Lohse (2000), it seems to us that a detailed study of how the interplay of plumes, the wind and the boundary layer influences λ_u is desirable. A first step in this direction is taken in a forthcoming study van Reeuwijk et al. (2008a,b), of which the results indicate that the scaling of λ_u cannot be derived from laminar boundary layer theory and scales as $\lambda_u \propto \lambda_T^{-1} Re^{-1}$.

Although the sdfs point towards the presence of turbulence in the boundary layer, the characteristics of the boundary layer are of a rather different nature than those of classical (i.e. shear-driven) turbulent boundary layers. Indeed, viscous forces are still significant in the boundary layer, as can be deduced from the domain height H in viscous units $\delta_v = \nu/u_\tau$, where $u_\tau \equiv \sqrt{\nu \frac{\partial u}{\partial z}|_w}$ is the friction velocity (Schlichting and Gersten, 1997). Assuming that $\frac{\partial u}{\partial z}|_w \approx U/\lambda_u$, the ratio H/δ_v which is the shear-

Reynolds number Re_τ , can be approximated by

$$\text{Re}_\tau \equiv \frac{u_\tau H}{\nu} \approx \left(\frac{\lambda_u}{H} \right)^{-1/2} \text{Re}^{1/2}. \quad (7.3)$$

The simulations show that $\text{Re}_\tau = 70$ at $\text{Ra} = 2.1 \times 10^7$, and the viscous thickness of the boundary layer $\lambda_u/\delta_v = \lambda_u/H\text{Re}_\tau$ is only a fraction of this already very low value. Therefore, viscous effects are significant in the boundary layer.

It is interesting to note that the scaling of the boundary layer thickness for flat plate flow changes from $\delta/x \propto \text{Re}_x^{-1/2}$ (laminar) to $\delta/x \propto \text{Re}_x^{-1/7}$ (turbulent, see White (1991)), where Re_x is the Reynolds number based on the distance x to the leading edge of the plate, and the thickness δ is the location where the velocity is 99% of the outer velocity. The decreased exponent resembles larger entrainment and thus a quicker growth of the boundary layer as a function of x . Upon assuming that the typical development length is H and that $\text{Re} \propto \text{Ra}^{1/2}$, the anticipated scaling for a turbulent boundary layer is $\delta/H \propto \text{Ra}^{-1/14}$. If $\alpha \approx -0.11$ is the scaling exponent $\lambda_u \propto \text{Ra}^\alpha$ from the simulations, then $-1/4 < \alpha < -1/14$, so the exponent may resemble an intermediate state.

However, it is not clear whether the entrainment mechanism of a developing boundary layer past a flat plate is transferable to RB convection; the active role of plumes which transfer fluid (and heat) into and out of the boundary layer may significantly affect the entrainment characteristics. It is our suspicion that the relatively weak forcing in the horizontal direction due to the wind (which is responsible for the friction factor C_f) is only weakly coupled to the relatively strong forcing in the wall-normal direction due to buoyancy. This may be the reason why the boundary layer has an sdf which is typical of developed turbulence but has many laminar features at the same time. Due to the weak coupling, the conceptual image of a laminar boundary layer may be appropriate for C_f but not for λ_u in the boundary layer in RB convection. Therefore, the straightforward application of well-known characteristics of the Blasius-type boundary layer (such as the criteria for laminar-turbulent transition and the scaling of λ_u with Re) to the boundary layers in RB convection is questionable without additional justification.

7.4 Conclusion

A combined numerical and experimental investigation was carried out to study the boundary layers in RB convection in a 4:1 aspect-ratio cell filled with water. The study covers a wide range of Ra numbers varying between 7.0×10^4 and 2.4×10^9 . The results for the lower Ra numbers were obtained from direct numerical simula-

tions, while those for the higher Ra numbers followed from laser Doppler anemometry. In the midrange, both techniques have an overlap of about one decade.

The probability density functions of the horizontal velocity components have a Gaussian-like shape for the complete Ra number range, except at the lowest Ra where the flow is in a state of spatio-temporal chaos. Probability density functions that are scaled with the velocity rms value overlap for the entire Ra number range, with the exception of the largest Ra numbers where the large-scale circulation, or “wind”, is predominantly visible in the histograms.

The spectral density functions of the horizontal velocity component that were determined in the bulk flow and in the boundary layer are surprisingly similar. Spectra in both regions of the flow are continuous and have a wide range of active scales for $Ra > 2.6 \times 10^6$. This indicates that both the bulk and the boundary layers are turbulent in the Ra number range considered, while (i) molecular effects are still noticeable in the boundary layer and (ii) the boundary layer does not behave like a classical shear-driven turbulent boundary layer.

8

Prime modes of circulation in large-aspect-ratio turbulent Rayleigh-Bénard convection

Based on a detailed experimental investigation in an aspect-ratio-4 rectangular cell in the range $3.7 \times 10^7 \leq \text{Ra} \leq 3.7 \times 10^9$, we present evidence of possible new scenarios of the long-term dynamics of large-scale circulations (LSC) in bounded large-aspect-ratio turbulent Rayleigh-Bénard convection. Karhunen-Loève analysis of instantaneous velocity fields from long-time particle image velocimetry measurements suggests two different states, but both appear to be produced by a single large-scale flow structure. The measurements provide a new three-dimensional picture of LSC in the $\Gamma = 4$ cell. A modified scaling relation between the LSC peak frequency ω_p and Ra is proposed.

8.1 Introduction

It is widely assumed that a better insight into a broad spectrum of physical phenomena encountered in the Earth's mantle, atmosphere and oceans, can be gained from better understanding of the structure and dynamics of turbulent Rayleigh-Bénard convection (RBC). This paradigm of thermal convection occurs when a fluid layer between two horizontal plates is sufficiently heated from below and cooled from above. We recall that RB convection is characterised by the Rayleigh number $Ra = \alpha g \Delta T H^3 / (\nu \kappa)$, and the Prandtl number $Pr = \nu / \kappa$, where α is the thermal expansion coefficient, ΔT is the temperature difference between the cold and the hot plate, H is the vertical distance between the plates, ν is the kinematic viscosity, and κ is the thermal diffusivity. The generic RBC implies infinite lateral width W , while all experiments consider bounded finite width-cells, thus introducing the aspect ratio $\Gamma = W/H$ as an additional parameter next to Ra and Pr .

RBC has been studied thoroughly, but many important questions remain unanswered (Niemela et al., 2000; Siggia, 1994; Bodenschatz et al., 2000; Kadanoff, 2001). In particular, the heat transfer scaling for high Ra numbers and the structure and dynamics of the large-scale circulation (LSC) are topics of intense research (Niemela and Sreenivasan, 2006; Resagk et al., 2006; Brown and Ahlers, 2007). Both topics are closely related since the LSC affects the heat transfer.

Most information on the LSC has been deduced from experiments in cells with aspect ratios around $\Gamma = 1$ where generally the LSC appears in the form of a single roll spanning over the entire cell with a nearly vertical circulation plane that meanders in azimuthal direction (Qiu and Tong, 2001; Sreenivasan et al., 2002; Sun et al., 2005b; Brown and Ahlers, 2006b). However, it is questionable whether insights gained for such small aspect ratios are relevant to the generic RBC problem, or to practical situations which are often laterally unbounded. The experiments of Niemela and Sreenivasan (2006) in a (cylindrical) $\Gamma = 4$ cell for Ra numbers between 10^8 and 2×10^{13} suggested indeed that the LSC consists of a single roll also for $\Gamma = 4$, but direct evidence in terms of velocity or temperature field, was not presented. Wu and Libchaber (1992) performed measurements in a $\Gamma = 6.7$ cell and Funfschilling et al. (2005) carried out heat transfer measurements in cylindrical water-filled cells with Γ varying between 1 and 6. They noticed a small but systematic effect of the aspect ratio on the heat transfer. Recently, Xi and Xia (2008a,b) have reported on the LSC in RB cells with $\Gamma < 1$. For $\Gamma = 1/2$ the LSC was found to have a single roll structure for most of the time although a counter-rotating double roll also occurred for brief periods. An interesting aspect of the work by Xi and Xia (2008a) is the direct measurement of the LSC through planar velocity measurements with particle image velocimetry (PIV).

The current work focuses on the structure and dynamics of the LSC in a $\Gamma = 4$

cell. PIV was used to directly measure the flow field for a range of Ra numbers between 3.7×10^7 and 3.7×10^9 . The obtained data sets each contain about 2×10^4 individual PIV image pairs (acquired at 1 Hz), which were subsequently analysed using Karhunen-Loève (K-L) decomposition to determine the most energetic modes and their time dynamics.

8.2 Experimental method

The experiments were conducted in a $600 \times 600 \times 155 \text{ mm}^3$ ($W \times W \times H$) water-filled cell, see also Chapter 6. Two hollow 9 mm copper plates at the top and bottom are kept at constant temperatures by passing water from two basins containing constant temperature water (inaccuracy less than 0.03 K) through the plates internal channels. The plates thus impose a controlled temperature difference ΔT on the working fluid. The side walls are made of 10 mm thick glass to allow optical access. A Cartesian coordinate system with its origin at the centre of the bottom wall is adopted with the x - and y -coordinates being parallel to the side walls and the z -coordinate denoting the wall-normal distance.

Instantaneous velocity fields were measured by using a PIV system that included a Continuum Minilite double-pulsed Nd:YAG laser with a pulse energy of $2 \times 25 \text{ mJ}$. This laser produced an approximately 1 mm thick light sheet that illuminated the seeding particles (10 μm diameter). Two PCO Sensicam cameras with a resolution of 1280×1024 pixels recorded images of the seed particles in the light sheet. A 28 mm focal length lens with a numerical aperture $f^\# = 4$ was mounted on each PCO camera. The time separation between pulses varied between 30 and 90 ms depending on Ra. The image pairs were analysed in three subsequent steps consisting of (adaptive) cross correlation, Gaussian local median filtering and interpolation. The final interrogation area was 16×16 pixels, corresponding to an area in the measurement plane of $0.4 \times 0.4 \text{ cm}^2$.

8.3 Karhunen-Loève decomposition

To extract the most dominant flow structures Karhunen-Loève (K-L) decomposition of the velocity field is made using the “method of snapshots” Sirovich (1987); Berkooz et al. (1993); Liu et al. (2001). The velocity field is expanded into a finite series of N orthogonal basis functions $\phi_n(\vec{x})$ and independent dimensionless coefficients $a_n(t)$:

$$\vec{u}(\vec{x}, t) = \sum_{n=0}^{N-1} a_n(t) \phi_n(\vec{x}), \quad (8.1)$$

where \vec{u} denotes the velocity at position \vec{x} at time t . Both $\phi_n(\vec{x})$ and $a_n(t)$ are uncorrelated and statistically orthogonal. When applied to subsequent instantaneous snapshots, solving $a_n(t)$ can be reduced to solving the eigenvalue problem

$$\int_T C(t, t') a_n(t') dt' = \lambda_n a_n(t), \quad (8.2)$$

where the two-point correlation tensor C is defined as $C(t, t') = \frac{1}{T} \int \int_V \vec{u}(\vec{x}, t) \cdot \vec{u}(\vec{x}, t') d\vec{x}$ and λ_n denote the eigenvalues. The spatial basis function belonging to $a_n(t)$ is obtained from

$$\phi_n(\vec{x}) = \frac{1}{T \lambda_n} \int_T a_n(t) \vec{u}(\vec{x}, t) dt. \quad (8.3)$$

Because of the orthogonality of the basis functions, the energy contribution of each mode adds up to the total energy of the flow field, $E = \sum_{i=1}^{N_T} \lambda_i$, where N_T denotes the total number of eigenmodes. The large scale flow structures are deduced by summing the largest eigenvalues. The mode ϕ_0 represents the ensemble average of all instantaneous velocity fields. For this reason ϕ_0 is called the “steady” mode while the higher modes are known as the fluctuating modes. For RBC such a procedure has been performed earlier for numerical simulations of RBC at low Rayleigh number ($Ra \sim 5 \times 10^4$) (Sirovich and Park, 1990; Park and Sirovich, 1990; Sirovich and Deane, 1991; Deane and Sirovich, 1991; Zoldi et al., 1998).

8.4 Results

Long-time PIV measurements ($\approx 2 \times 10^4$ s) have been conducted in the $y = 0$ plane of the cell for twelve Ra numbers between 3.7×10^7 and 3.7×10^9 . In this Rayleigh number range the Prandtl number varied between 5 and 7. Non-Boussinesq effects did not play a significant role as $\Delta T < 10$ K ($Ra < 5 \times 10^9$) for all Ra numbers considered in this experiment.

The four most energetic modes of the K-L analysis for $Ra = 3.9 \times 10^7$ are depicted in descending order in Fig. 8.1. Streamlines are plotted to indicate the flow structures. The steady mode, ϕ_0 , consists of two counter rotating cells that are nearly symmetric with respect to the y, z -plane. The time series for $a_0(t)$ shows that there was no change in direction for any significant period during the 19000 s measurement. The fluctuating modes ϕ_1 to ϕ_3 indicate an increasing number of rolls. At $Ra \sim 10^7$ the most energetic fluctuating modes appear to be regular rolls. For higher K-L modes, i.e. from ϕ_4 onwards, small scale structures resembling intermittent plumes become dominant, while regular rolls patterns are no longer observed.

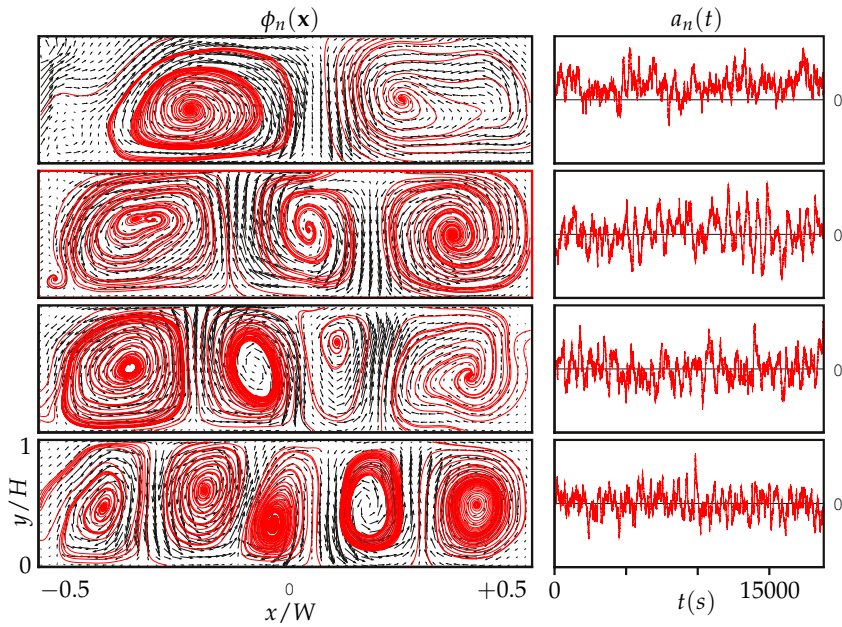


Figure 8.1: Spatial basis functions ϕ_n for the four most dominant K-L modes for $Ra = 3.9 \times 10^7$, $n = 0, 1, 2, 3$ (top-to-bottom). The depicted modes jointly contain 35% of the total energy in the system. The steady mode ϕ_0 contains 11% of the total energy.

Figures 8.2 and 8.3 show the results of the K-L decomposition for $Ra = 6.2 \times 10^8$ and $Ra = 5.9 \times 10^8$, respectively. For these Ra numbers a single roll encompassing the entire width of the RB cell has emerged as the steady mode ϕ_0 . This is consistent with the results of earlier PIV experiments reported in Chapter 7 that showed that the mean wind sets in for $Ra > 10^8$. From the analysis of the fluctuating modes in Figs. 8.2 and 8.3, it appeared that two different sets of modes can occur, indicating two different flow patterns. The first type (type I) is depicted in Fig. 8.2. In that case the higher order modes have an increasing number of rolls not dissimilar to the rolls seen in Fig. 8.1. For the fluctuating modes ϕ_2 and ϕ_3 , the flow in between the roll centres is inclined because the centres are not at the same height above the plate. This is in contrast to the situation for the lower Rayleigh number (Fig. 8.1) where the fluid appears to rise (or fall) more or less vertically in between the cell centres.

Figure 8.3 depicts the other set of modes (type II). In this case the fluctuating modes ϕ_1 and ϕ_2 are diagonal flow patterns. The steady mode ϕ_0 takes a larger share of the total energy than the steady mode for type I. It is interesting that the time series for $a_1(t)$ changes sign in a strongly periodic manner for both types of modes. We argue that the two sets of modes are produced by the same flow structure and expect the same pattern if data from different experiments are rotated by $\pm 90^\circ$ around the z -axis. At the start up of the RBC, this flow structure locks in a certain orientation and then appears at the fixed PIV plane as either a type I or a type II flow pattern. It may even be possible that the flow structure rotates during an experiment but this did apparently not happen during the measurements here presented.

Both sets of modes shown in Figs. 8.2 and 8.3 appear randomly in repeated experiments at the same Ra number. Reversals or cessations of the flow are not involved in this process as the time series for $a_0(t)$ do not change sign for any significant time during the measurements. Figure 8.4 sketches a three-dimensional model for the flow structure in the $\Gamma = 4$ cell. Plane A shows the counter rotating rolls corresponding to fluctuating mode ϕ_1 for type I. Plane B shows the steady mode ϕ_0 (dashed line) and the first fluctuating mode (thick line) for type II. As mentioned earlier, the mean wind is strongest in plane B (type II). Figure 8.4 also illustrates the effect of the periodicity in the fluctuating mode ϕ_1 . As explained in Chapter 6, during the first phase of the cycle, the mean wind is along the circumference of the cell with groups of plumes moving up (or down) along the side walls. However, there are also groups of plumes moving up long before reaching the side wall along an “ascending diagonal” in plane B (Fig. 8.4 (top)). The latter flow induces the counter rotating cells in plane A. During the second phase the fluid stops moving up along the diagonal. During the third phase the flow along the “descending diagonal” in plane B has set in as sketched in Fig. 8.4 (bottom). This causes the counter rotating cells in plane A to reverse direction. During phase four the flow along the descending diagonal loses its strength, and the process repeats itself.

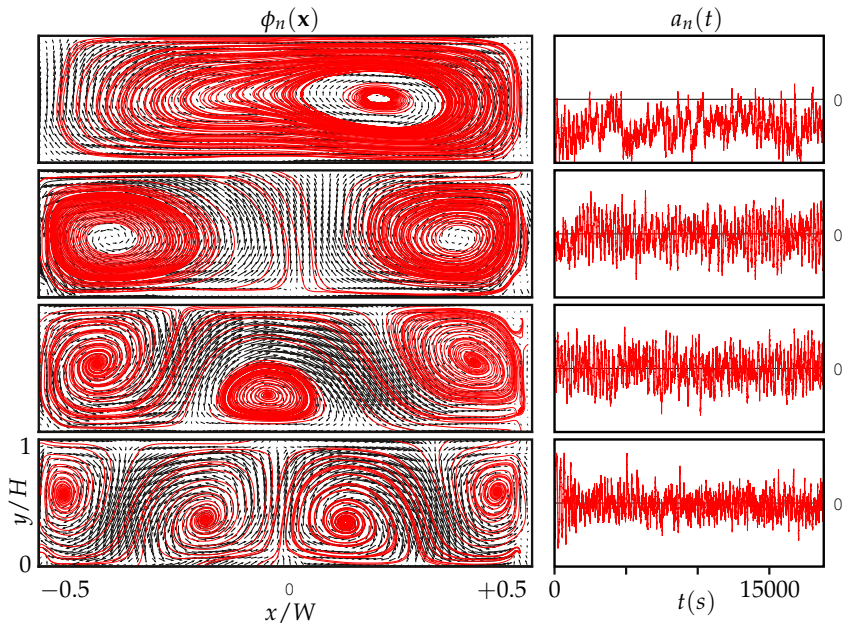


Figure 8.2: “Type 1” spatial basis functions ϕ_n (left) and corresponding coefficients $a_n(t)$ (right) for the four most dominant K-L modes at $Ra = 6.2 \times 10^8$, $n = 0, 1, 2, 3$ (top-to-bottom). The depicted modes jointly contain 41% of the total energy in the system, whereas the steady mode ϕ_0 contains 17% of the total energy.

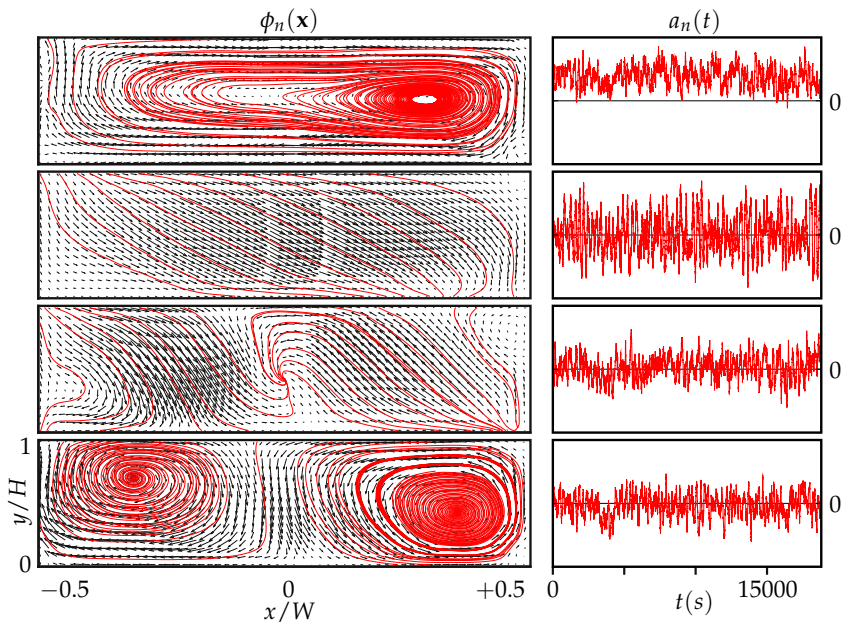


Figure 8.3: “Type 2” spatial basis functions ϕ_n (left) and corresponding coefficients $a_n(t)$ (right) for the four most dominant K-L modes at $Ra = 5.9 \times 10^8$, $n = 0, 1, 2, 3$ (top-to-bottom). The depicted modes jointly contain 50% of the total energy in the system, whereas the steady mode ϕ_0 contains 26% of the total energy.

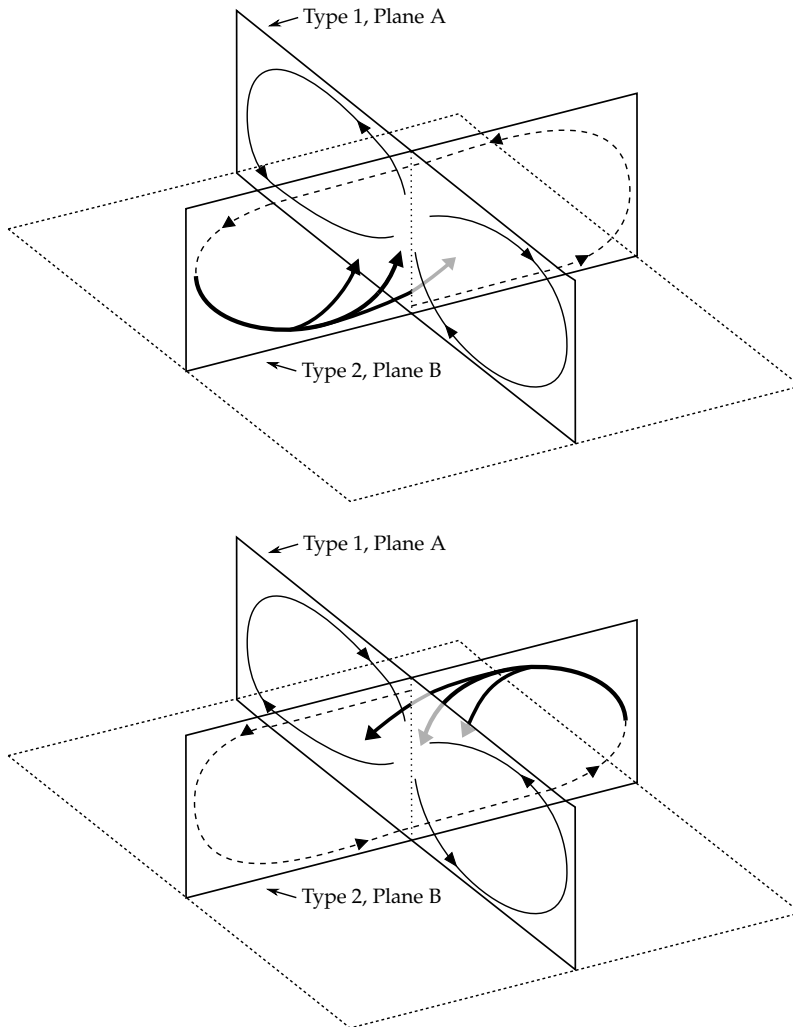


Figure 8.4: Schematic of the flow structure in the aspect-ratio-4 cell at two instants in time separated by half a period of the LSC.

The oscillating time series of $a_1(t)$ in Figs. 8.2 and 8.3 can be used to determine a power spectrum. The oscillation of the LSC shows up as a peak in this spectrum at a characteristic frequency ω_p . Unlike point measurements from a single PIV vector, a thermistor or a laser Doppler anemometer (LDA), the $a_1(t)$ time series is calculated using all spatial and temporal information of the instantaneous velocity fields, which effectively increases the statistical reliability of the power spectrum of $a_1(t)$. This is especially important for measurements at relatively low Rayleigh number, where characteristic time scales are very large.

The circular frequency ω_p of the oscillating LSC is often scaled with the size of the RBC cell and the diffusion coefficient to enable a comparison with data from other sources (Sano et al., 1989; Niemela et al., 2001). Niemela and Sreenivasan (2006) use the diagonal of the cell $\zeta = (H^2 + W^2)^{1/2}$ to make the circular frequency ω_p dimensionless as in $\omega_p^* = \omega_p H \zeta / \kappa$. Figure 8.5 shows the ω_p^* -Ra data from the present K-L data together with the data from our earlier LDA measurements (Chapter 7). Also shown are the results of an experiment in a $\Gamma = 4$ cell operated with helium gas around a temperature of 5 K (Niemela and Sreenivasan, 2006). A least-squares fit to the K-L data resulted in $\omega_p^* \sim \text{Ra}^{0.38 \pm 0.01}$. This exponent differs significantly from the 0.48 – 0.49 reported for other, mostly $\Gamma = 1$ experiments, though for significantly higher Ra numbers (Ciliberto et al., 1996; Niemela et al., 2001; Qiu and Tong, 2001; Qiu et al., 2004). Niemela and Sreenivasan (2006) reported that the dependency of ω_p^* on Ra was the same for $\Gamma = 1$ and $\Gamma = 4$ cells, i.e., $\omega_p^* \sim \text{Ra}^{0.46}$. However, Fig. 8.5 shows that for $\text{Ra} < 10^{10}$ the $\Gamma = 4$ data of Niemela and Sreenivasan (2006) have an exponent of 0.39 which is nearly equal to that found in the present experiment.

8.5 Conclusion

Our experiments show in detail the structure and dynamics and the large scale flow in thermal convection in square $\Gamma = 4$ convection cells. For $\text{Ra} < 10^8$, RB convection in this geometry is characterised by isolated rolls. For higher Ra, two types of flow patterns consistently appear. Both patterns are consistent with a three-dimensional model of the LSC explaining the observed periodicities of co- and counter-rotating modes. We conjecture that the scenario here described, can be generalised to bounded RB convection for a broader range of high aspect ratios, presumably valid for $\Gamma = 3 - 8$, with the exception of the first mode that may differ for very large Γ .

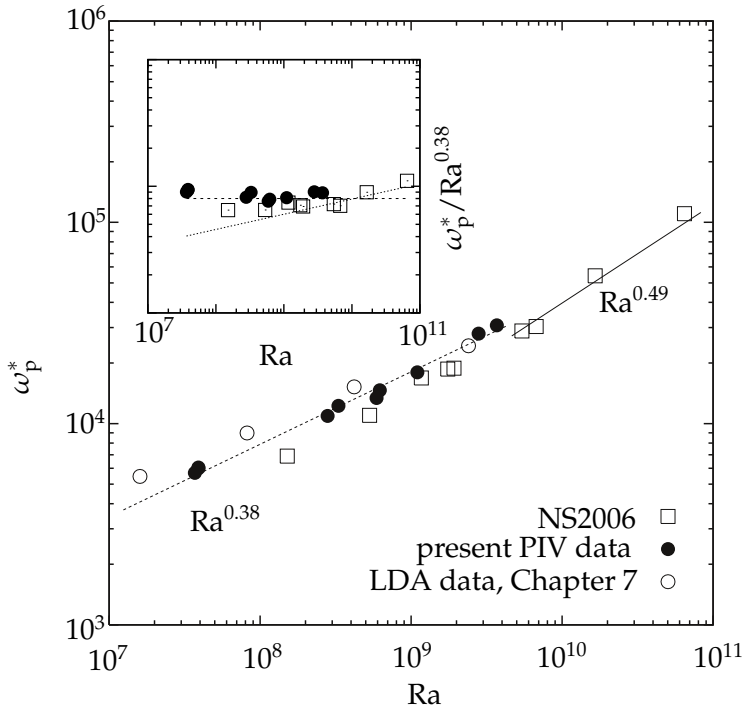


Figure 8.5: Dimensionless circular frequency $\omega_p^* = \omega_p H \zeta / \kappa$ as a function of Ra for the present PIV data, compared to data obtained with LDA (Chapter 7) and to $\Gamma = 4$ data from low-temperature helium cells (Niemela and Sreenivasan (2006), indicated by NS2006). A least-squares fit to the K-L data results in the relation $\omega_p^* \sim Ra^{(0.38 \pm 0.01)}$. The inset shows the same graph compensated with $Ra^{0.38}$.

9

Electromagnetic forcing visualisations

This chapter explores the potential of electromagnetic (EM) forcing on an electrolyte solution to enhance heat and momentum transfer in Rayleigh-Bénard and other types of thermal convection. EM flow control makes use of electrodes (current density \vec{j}) and sub-surface permanent magnets (magnetic induction \vec{B}) to create local Lorentz forces ($\vec{j} \times \vec{B}$). Near the wall the $\vec{j} \times \vec{B}$ forces induce direct effect upon the flow velocity and vorticity. Unlike common MHD applications where the magnetic force suppresses the fluid motion, turbulence and heat transfer, significant enhancement can be obtained with an appropriate set-up of the magnetic field EM forcing. Here we present some results of preliminary experiments in a “cold” environment (without any heating) for two different magnet configurations. Both a two and three dimensional forcing are investigated and visualisations are carried out with fluorescent dye. The extension of the work to the use of electromagnetic forcing in combination with thermal convection for a possible control of Rayleigh-Bénard convection is discussed.

Parts of this chapter have been published in the Proceedings of the 7th International Symposium on Fluid control, measurement and visualization, Verdoold et al. (2003)

9.1 Introduction

The potential of using an electromagnetic field to control flow, turbulence, heat and mass transfer in electrically conductive fluids has long been recognised. Magnetic brakes are widely used to stabilise the flow in metal casting, to suppress instabilities and turbulence in crystal growth, to control mixing of conductive fluids. In most cases the magnetic field suppresses the fluid and its fluctuations (turbulence), leading to a reduction in heat and mass transfer. However, with appropriate arrangement of the magnetic field (e.g. with permanent magnets attached to the bounding walls) and in combination with an imposed electric current, it is possible to generate local motion in the near-wall flow regions, which can lead to significant enhancement of heat and mass transfer. To explore this potential, we are investigating potential effects of electromagnetic (EM) forcing on thermal convection. The test case selected is Rayleigh-Bénard (RB) convection in which the heat transfer between a hot bottom and a cold top wall is to a large extent controlled by large-scale convection cells, generated by the characteristic upward hot and downward cold plumes. The origin of these plumes is, in turn, controlled by the motion and heat transfer in wall boundary layers at both horizontal walls. The conventional (non-magnetic) RB convection is a paradigm for thermal convection and much information is available in the literature. However, a recent numerical simulation by Hanjalić and Kenjereš (2000) revealed a striking reorganisation of the RB flow structures when a homogeneous, vertical magnetic field was applied. This reorganisation of flow structures resulted in a decrease of the heat transfer. In the present work the magnetic field is not homogeneous, but concentrated close to the (hot) wall. This type of forcing has been used earlier in experiments on boundary layer control (e.g. Henoach and Stace (1995) and Rossi and Thibault (2002)). With this forcing the heat transfer control can be focused to the near-wall region and indirectly further away from the walls by induced flow. In this way the flow can be induced and enhanced, which is a major difference from the common magnetohydrodynamics (MHD) applications where flows are damped. In this chapter the attention is confined to a cold experiment, aimed at investigating effects of various magnet arrangements on flow forcing.

Electromagnetic flow control makes use of a permanent magnetic field combined with an electrical current in a fluid. This generates the Laplace force $\vec{j} \times \vec{B}$, Eq. 2.39. For thermal convection subjected to electromagnetic forcing, the Navier-Stokes momentum equation, Eq. 2.2 can be written as:

$$\rho \frac{\partial u_i}{\partial t} + \rho u_j \frac{\partial u_i}{\partial x_j} = -\frac{\partial p}{\partial x_i} + \mu \frac{\partial^2 u_j}{\partial x_j^2} - \rho g + \epsilon_{ijk} j_j B_k, \quad (9.1)$$

where ϵ_{ijk} is the Einstein notation for the cross product $\vec{j} \times \vec{B}$. The last two terms

denote the buoyancy and electromagnetic force, respectively. Depending on the orientation of the local Lorentz force with respect to the gravitation vector these two forces can generate very different effects on flow and turbulence structure and heat transfer.

To close the Navier-Stokes equation, additional equations are needed connecting the electric current density, magnetic and velocity fields. Ohm's law (Eq. 2.40) makes a distinction between the current due to the presence of an electric field \vec{E} and the induced current from the motion of the fluid with velocity \vec{u} in the presence of a magnetic field \vec{B} . When comparing the order of magnitude of the terms, the $\vec{u} \times \vec{B}$ term can be neglected because $|\vec{u} \times \vec{B}| \ll |\vec{E}|$, so Eq. 2.40 simplifies to

$$\vec{j} \approx \sigma \vec{E}. \quad (9.2)$$

Combining the Maxwell equations with Ohm's law yields the magnetic induction equation (e.g. Davidson (2001) and Sect. 2.3):

$$\frac{\partial \vec{B}}{\partial t} = \nabla \times (\vec{u} \times \vec{B}) + \frac{1}{\text{Re}_m} \nabla^2 \vec{B}, \quad (9.3)$$

where the magnetic Reynolds number is defined by Eq. 2.44.

In this experiment the conductivity of the used fluids is low ($\sigma \approx 5 \text{ S m}^{-1}$) and the magnetic permeability is very close to the permeability of vacuum ($\mu_0 = 1.23 \times 10^{-6} \text{ H m}^{-1}$). This leads to a magnetic Reynolds number Re_m in the order of 10^{-5} to 10^{-7} . Furthermore, by the use of permanent magnets $\partial \vec{B} / \partial t$ is zero. This leads to a simplification of the induction equation:

$$\nabla^2 \vec{B} = 0. \quad (9.4)$$

From Equations 9.2 and 9.4 it can be seen that the electromagnetic forcing $\vec{j} \times \vec{B}$ is independent of any flow variable and thus the forcing is independent of the flow. This makes it an ideal external force to influence the flow.

9.2 Experimental set-up

The set-up used for the cold experiment is based on the $0.60 \times 0.60 \times 0.15 \text{ m}$ glass tank, described in Chapter 4. In the visualisation experiments, optical access from the top is required and no heat transfer is involved. Therefore, the top cooling element in Fig. 4.7 is removed and the glass box is now covered by a glass plate functioning as a top lid, whereas the bottom consists of a black coated 9 mm thick PVC plate, see Figure 9.1. At the top of the two glass sides of the tank, platinum wires are mounted in the cavities, which were specially added to house the platinum electrodes. When the electrodes are connected to a current supply, an electrical (\vec{E}) field

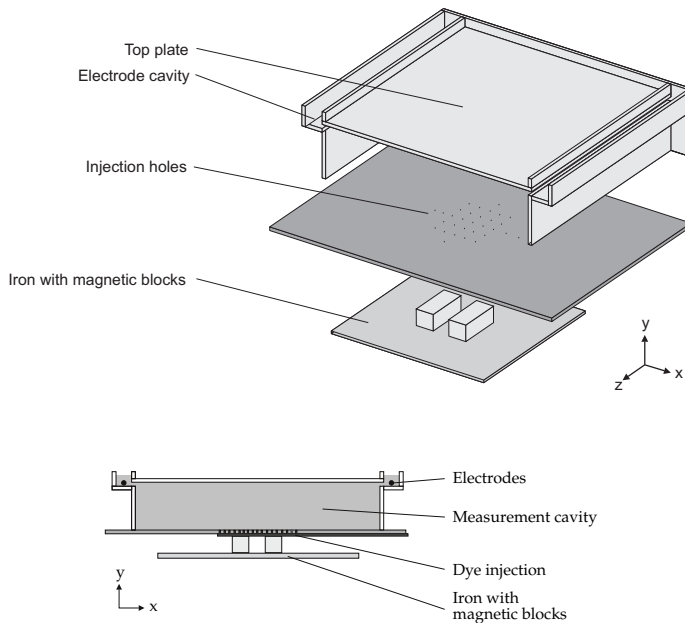


Figure 9.1: Experimental set-up. In the top image from top to bottom: glass tank, bottom plate, magnets on iron plate. Notice the confined volume for the electrodes at the top-left and top-right positions. The bottom image shows the front view of the set-up.

distribution is generated in the tank. Although the current supply is capable of generating higher currents, most of the time only 2 A at 10 V is used to provide the \vec{E} field. Higher currents are able to put the whole tank in motion. Higher currents also lead to intense electrolysis of the water, and, as a consequence, a large amount of hydrogen gas bubbles form and enter the measurement cavity, which is not desirable. The placement of the electrodes at the top gives an almost homogeneous field near the centre in the bottom of the tank, i.e. the place where the magnets have their largest influence. Results of calculations of the electrical field are displayed in Fig 4.6. Recall that the field is almost homogeneous in the x -direction near the bottom wall in the centre of the tank, the region where the magnetic field is maximum.

A static magnetic field near the bottom wall of the tank was created by using Neodymium-iron-boron (NdFeB) permanent magnets, as described in Sect. 4.3.2. The magnets (two opposite poles) are placed on an iron plate to close the magnetic field lines. The typical gap between the magnetic blocks is 40 mm, the same as their horizontal dimension.

Our aim is to investigate Rayleigh-Bénard convection at a reasonably high Rayleigh number of approximately 10^8 . Water was chosen as a working fluid because it

provides optical access for advanced measurement techniques such as particle image velocimetry (PIV), laser Doppler anemometry (LDA) and liquid crystal thermography (LCT). However, the conductivity of tap water is quite low, in the order of 0.01 S m^{-1} . To enhance the conductivity of the working fluid without changing its properties much, the glass tank is filled with an electrolyte solution. A 70 g l^{-1} sodium sulphate (Na_2SO_4) solution is used as a working fluid which has a much higher conductivity of 5.5 S m^{-1} . Sodium sulphate is preferred to other electrolytes, to prevent the formation of unwanted products through electrolysis, e.g. $\text{Cl}_2(\text{g})$ when using NaCl (used by Rossi (2001)) or solid copper $\text{Cu}(\text{s})$ when using CuSO_4 (used by Weier et al. (1998)). The conductivity can possibly be enlarged using strong acids, whose conductivity can be up to 200 S m^{-1} , but in that case special precautions have to be made for laboratory safety. The ratio of the viscosity of this electrolyte and water is approximately 1.20.

For visualisation purposes, 32 small holes with a diameter of 0.8 mm are placed in the bottom plate. The holes are connected to a tube system which leads to a container with the same sodium-sulphate solution coloured with a fluorescent disodium- fluorescein dye. It is used to visualise distinct paths in the flow. The fluorescein enters the experimental cavity in a quiescent way so that the effect on the flow is negligible. The illumination is provided by a 1000 W halogen light which can be focused on different parts of the water tank.

For investigation of the near-wall forcing, we can make a distinction in the way the magnets and the electrodes are placed. In the chosen design of the tank, the only adjustable parameter for the current density is the current itself which is in the order of 2 A.

For the magnetic part of the $\vec{j} \times \vec{B}$ forcing, there are more properties to adjust: the geometry of the magnetic blocks and their position. Changing the length scales of the block will result in changing the characteristic length of the forcing. An important parameter is the direction of the magnetic field between the magnets: it can be aligned with the current density vector which results in a two dimensional flow or it can be normal to \vec{j} which leads to a more complex three dimensional flow. Both configurations will be described in the next paragraphs and will be called the *Shear* and the *Pump-in & -out* configuration, respectively.

9.3 Computation and design

9.3.1 MHD dimensionless numbers

To provide an indication of the dominant forcing mechanism, two scaling parameters are used. The squared Hartmann number Ha is the ratio of the EM driving force and the viscous force in the boundary layer and is defined by Eq. 2.45. To relate the electromagnetic forces to inertial forces, the Stuart number or interaction parameter N is defined by Eq. 2.46. The characteristic scales for the present experiment are given in Table 9.1. The Hartmann number is larger than 10, and, therefore, it can be concluded that the electromagnetic forcing mechanism is strong compared to viscosity. The low Stuart number indicates that the flow becomes lightly dominated by inertia when the distance from the wall increases.

characteristic height h_{EM} (mm) ^a	37.5
characteristic velocity u_{EM} (mm s ⁻¹)	32.6
characteristic timescale \mathcal{T}_{EM} (s)	8.7
Hartmann number Ha	14
Interaction parameter N	0.2
typical temperature difference ΔT (K)	5
characteristic velocity u_{RB} (mm s ⁻¹)	33.8

Table 9.1: Calculated characteristic scales for the Shear configuration (*top*) and for a typical RB convection experiment (*bottom*). The characteristic height is defined as the height where 25% of the maximum forcing in z -direction is obtained.

9.3.2 Shear configuration

When the direction of the magnetic field between the magnetic blocks is in the x -direction, the $\vec{j} \times \vec{B}$ forcing will concentrate directly above the magnetic blocks as depicted in Figure 9.2(a). The flow will mainly be forced in z -direction, and will have a nearly two-dimensional character; it seems to shear the fluid along the wall. This shear motion will lead to the creation of a vortex in between the magnets.

9.3.3 Pump-in & -out configuration

When one magnetic block is added and the magnetic blocks are rotated over 90° with respect to their initial position, the $\vec{j} \times \vec{B}$ forcing will be pointing out of the magnetic

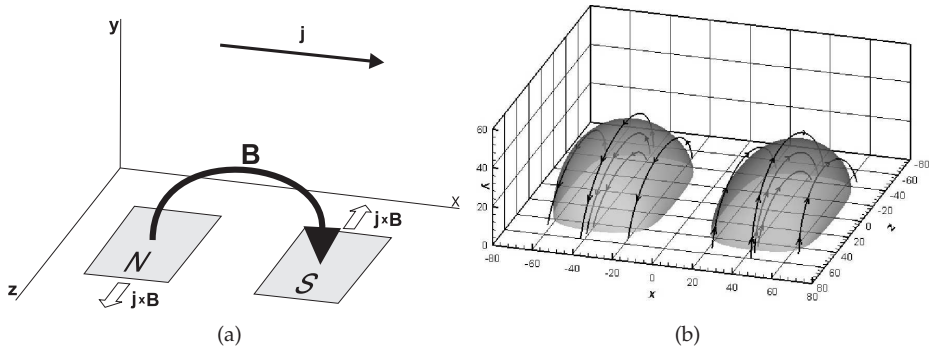


Figure 9.2: Shear configuration. (a) depicts a schematic of the configuration. (b) shows the calculated force lines and 25% isosurfaces of maximum longitudinal forcing $(\vec{j} \times \vec{B})_z$.

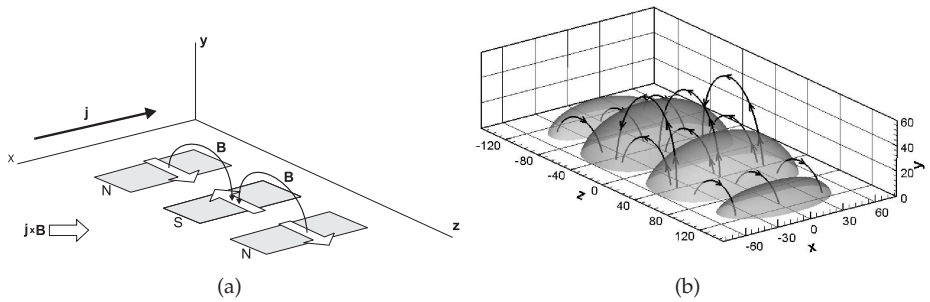


Figure 9.3: Pump-in & -out configuration. (a) depicts a schematic of the configuration. (b) shows the calculated force lines and 25% isosurfaces of maximum wall normal forcing $(\vec{j} \times \vec{B})_y$.

source regions as can be seen in Figure 9.3(a). The main flow will be accelerated over the three magnetic sources and two distinct regions seem to form in between: the *Pump-in* region where fluid is attracted to the wall, and the *Pump-out* region where fluid is pushed away from the wall.

9.4 Results and discussion

9.4.1 Shear configuration

To study the effect of various magnet arrangements on the dynamics of the flow and vortex structures, light sheets have been focused on various planes of interest. For the Shear configuration, three experiments have been conducted. In two ex-

periments we focused on the visualisation of the vortex structure in two horizontal planes (viewed from the top): one in the neighbourhood of the largest electromagnetic forcing, which is near the bottom wall (approximately 5 mm from the wall), and one far away from the EM forcing, close to the top wall (approximately 150 mm away from the bottom wall). In the third experiment the vortex structure was visualised from the side.

Visualisation in the near-bottom plane

To visualise the vortex structure, the dye is injected through two injection holes, placed precisely in the middle between the magnetic source areas. As can be seen in Figure 9.4, the vortex is initially attracted to the regions of highest EM forcing, i.e. the centre of the magnetic blocks. After about 20 s, the dye is accelerated in the region above the magnets and approximately 120 seconds after the first application of the electromagnetic forcing a strong vortex is created close to the bottom wall with a size roughly equivalent to the space between the magnetic blocks. However, the core of the vortex appears to move with time towards the wall, but remained positioned above the forcing area.

Visualisation in the near-top plane

Outside the direct forcing region an induced swirling flow develops above the magnetic blocks, as indicated in Figure 9.5. The time required for this induced vortex to develop, is only slightly longer than that for the development of the direct forced vortex. After about 180 seconds a stable vortex is created with a characteristic width of about 80 mm. The shear vortex viewed from the top shows similarities with a geophysical flow generated by Coriolis forces.

Side view

In Figure 9.6 the vortex structures in the Shear configuration are visualised from the side. Before applying the EM forcing, a large amount of dye is injected at the top of the box and, after the onset of the EM forcing, dye is continuously injected from the two holes in the bottom wall. The two dye threads immediately show the formation of the direct vortex. The height of the direct forcing is approximately 35 mm which corresponds to the calculated characteristic height h_{EM} for the Shear configuration. After about 20 s from the start of the EM forcing, the indirect vortex starts to pump down dye from the top wall to the bottom wall into the central region

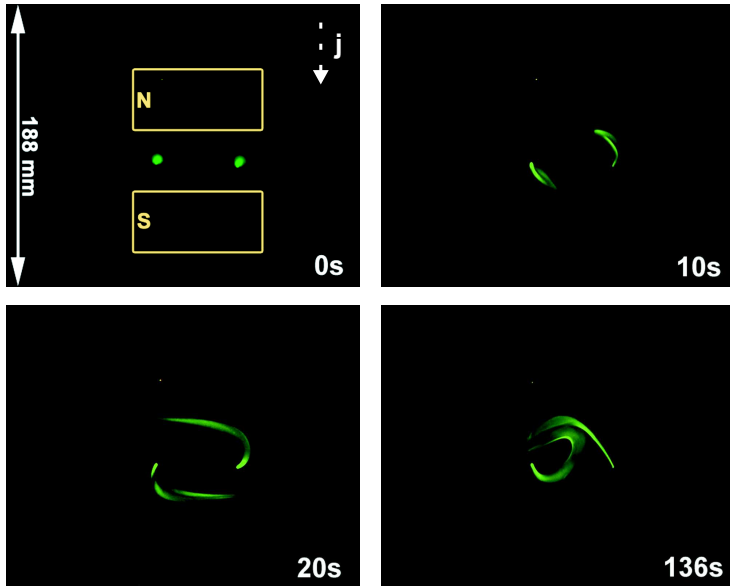


Figure 9.4: Traces of dye, injected from two holes, in the near-bottom plane (5 mm away from the bottom wall) for the Shear configuration. Electromagnetic properties: $I = 1.0 \text{ A}$, $v = 7.30 \text{ V}$, effective magnetic field at the surface $B_{\text{surf}} = 0.65 \text{ T}$ and $j = 10.4 \text{ A m}^{-2}$.

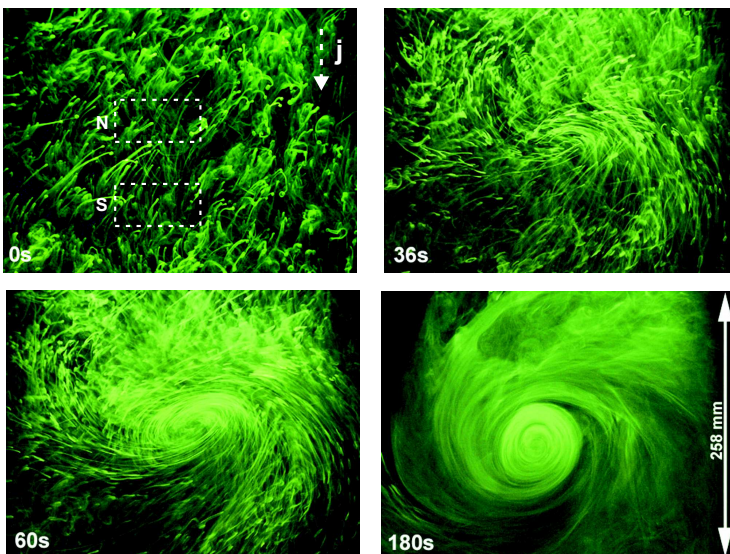


Figure 9.5: Vortical structures for the Shear configuration. Dye is initially randomly distributed. EM properties: $I = 2.0 \text{ A}$, $V = 11.9 \text{ V}$, $B_{\text{surf}} = 0.65 \text{ T}$ and $j = 21.7 \text{ A m}^{-2}$.

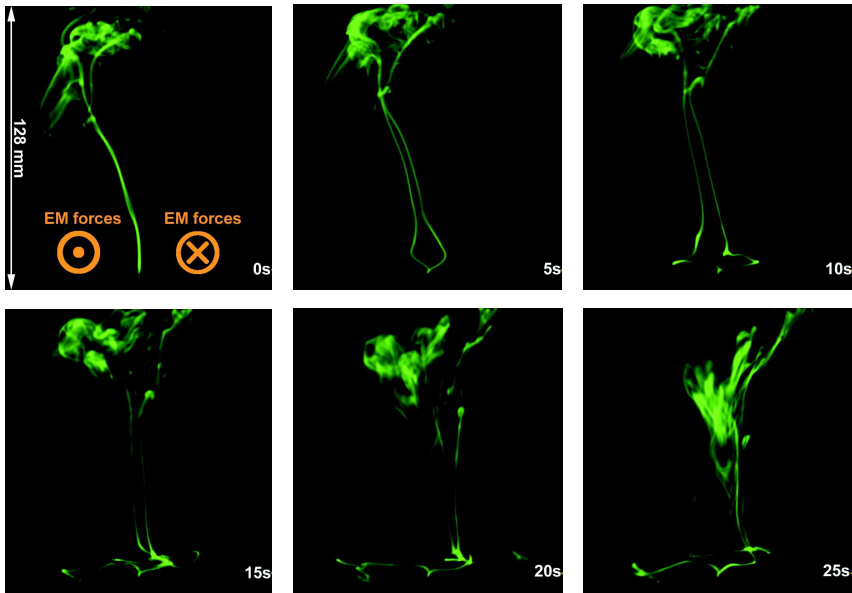


Figure 9.6: Vortex structure in the Shear configuration viewed from the side. Dye is injected from two holes in the bottom wall. Before application of the forcing the dye had already formed two lines in the measurement cavity. EM properties: $I = 2.2 \text{ A}$, $V = 11.9 \text{ V}$, $B_{\text{surf}} = 0.65 \text{ T}$ and $j = 23.5 \text{ A m}^{-2}$.

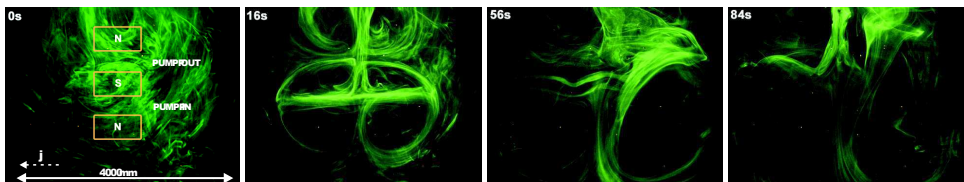


Figure 9.7: Results of the Pump-in & out configuration, viewed from above. Dye is initially randomly distributed. EM properties: $I = 2.2 \text{ A}$, $V = 11.9 \text{ V}$, $B_{\text{surf}} = 0.65 \text{ T}$ and $j = 23.5 \text{ A m}^{-2}$.

of the tank. A counterflow can be observed at both sides of the vortex. For Rayleigh-Bénard convection this configuration can lead to more intense cold falling plumes while increasing the mixing near the wall and thus the heat transfer.

9.4.2 Pump-in & -out configuration

Top view

Figure 9.7 depicts the results of the Pump-in & -out configuration when viewed from above. The initially randomly distributed dye organises itself quite rapidly in a six cell structure. The fluid accelerates into the Pump-in region as it moves over the first magnetic block. In the Pump-out region fluid is moved to both sides, while the fluid is pushed out of this volume.

Side view

In Figure 9.8 the Pump-in & -out configuration is viewed from the side. Several dye emission lines are used for visualisation. In the Pump-in region the flow converges in the first moments after the application of the EM forcing. After 40 seconds, vorticity is generated in this region and wall-parallel vortex rolls develop. Fluid is accelerated over the centre magnet and the vortex rolls are transported by this flow until they reach the Pump-out region, where the fluid is effectively accelerated outwards. It would be interesting to study the effects of an array of magnets with alternating polarity for the Pump-in & -out configuration.

In the case when the Pump-in & -out configuration is used in combination with Rayleigh-Bénard convection, it can attract the flow towards the wall in the Pump-in region, enabling control of the local thermal boundary layer. When cold plumes descend, they can be pumped close to the wall and accelerated. The heat transfer is possibly larger than in the conventional Rayleigh-Bénard convection where the thermal buoyancy is the only force. Hot rising plumes can be accelerated further in the Pump-out region, where the vertical velocity will be enhanced.

9.5 Conclusions and perspectives

We presented some qualitative results of an experimental investigation of electromagnetic forcing (EM) effects on initially stationary conductive fluid in a tank with different magnet arrangements. This exploration is the introduction into a study of

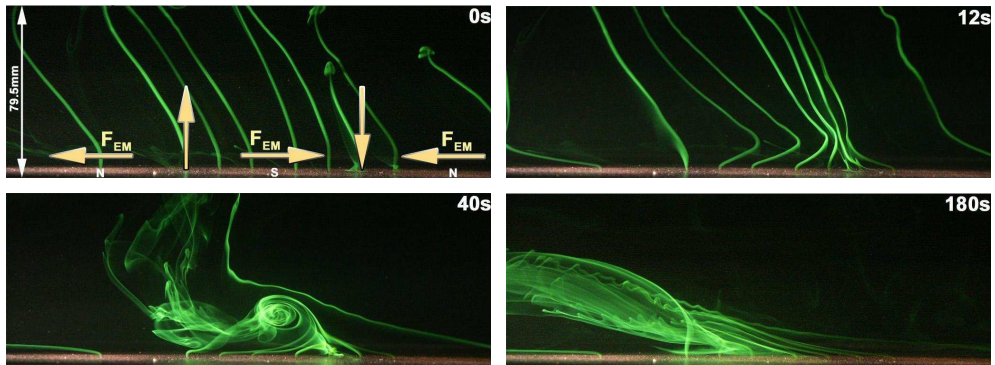


Figure 9.8: Flow visualisation for the Pump-in & -out configuration, viewed from the side. EM properties: $I = 1.0 \text{ A}$, $V = 8.4 \text{ V}$, $B_{\text{surf}} = 0.65 \text{ T}$ and $j = 10.8 \text{ A m}^{-2}$. Arrows indicate the direction of the EM forcing F_{EM} .

the potential of EM control and enhancement of thermal convection. Two configurations have been studied: a configuration that yields a two dimensional forcing creating a vortex with dimensions that are directly linked to the dimensions of the magnetic field, and another configuration where fluid is attracted and accelerated between two magnetic blocks and pumped away in between two other blocks. Both these configurations seem suitable for imposing desirable changes in the wall boundary layer and thereby the local heat transfer.

Unlike the Shear configuration where length scales are directly linked to the shape of the magnetic source, the Pump-in &-out configuration is very sensitive to the shape and the number of magnets. An experiment with an array of magnets could give more understanding of the use of three dimensional EM forcing in controlling free and forced thermal convection.

A quantitative analysis on the instantaneous velocity and vorticity fields will be described in the next chapter.

10

Electromagnetic control experiments

This chapter reports on an investigation of the interaction between thermal buoyancy and electromagnetic (EM) forcing, aimed at utilising the latter to control heat transfer in natural and mixed convection. Recent numerical simulations by Kenjereš and Hanjalić (2004) indicated a reorganisation of coherent flow structures in Rayleigh-Bénard (RB) convection when a local forcing is applied. The focus of this chapter is on manipulating these structures by local Lorentz forces. The two and three magnet configurations from Chapter 9 are further investigated with PIV and compared to LES simulations. Temperature measurements are performed to test the application of the three-magnet configuration to modulate the boundary layer in Rayleigh-Bénard convection. The results of the measurements reveal characteristic vortices as well as a change in heat transfer in the vicinity of the local forcing.

Parts of this chapter have been published in the proceedings of the Fifth Symposium on Turbulence, Heat and Mass Transfer, Dubrovnik, Croatia, September 25-29, 2006, Verdoold et al. (2006b) and in Int. J. of Heat and Fluid Flow, Kenjereš et al. (2009).

The numerical data (LES) is provided by a finite-volume Navier-Stokes/Maxwell solver for three-dimensional non-orthogonal geometries. The Cartesian vector and tensor components in the collocated mesh are applied for both fluid flow ($\overline{u}_i, \overline{p}$) and electromagnetic variables ($\overline{B}_i, \overline{E}_i$). All details can be found in Kenjereš et al. (2009).

The control of fluid flow and heat transfer by electromagnetic fields has many applications, such as magnetic braking to stabilise a flow in metal casting and avoiding instabilities and damping turbulence in crystal growth processes. The objective in many of those applications is to suppress turbulence or retard a flow. However, with a suitable arrangement of a magnetic and an electric field, it is possible to generate motion in the near-wall flow regions. In contrast to the forementioned applications, using a local forcing can increase the heat and mass transfer significantly.

To investigate this process, a well-known type of thermal convection has been selected, Rayleigh-Bénard (RB) convection, in which a number of self-organised phenomena are known to exist including erupting plumes, large-scale circulation, and wind reversals (e.g. Siggia, 1994; Niemela et al., 2000; Verdoold et al., 2006a). In RB convection, a flow medium between two constant temperature walls is cooled from above and heated from below. Heat transfer will be mainly governed by a large-scale circulation (also known as “wind”), which is generated by characteristic upward hot and downward cold plumes. RB convection has been extensively studied, but so far not much is known about the interaction with other body forces. Hanjalić and Kenjereš (2000) revealed a reorganisation of the typical structures in RB convection when a homogeneous, vertical magnetic field was applied, resulting in a decrease of heat transfer.

In contrast to earlier measurements on EM boundary layer control, where often an array of magnets with alternating polarity is used (e.g. Henoch and Stace (1995) and Crawford and Karniadakis (1997)), we make use of a strong local forcing close to the wall. The EM forcing is imposed by placing permanent magnets below an electrically conducting fluid, which will create a Lorentz force normal to both fields.

10.1 Methodology

The experiments are conducted in the same $0.600 \times 0.600 \times 0.155$ m ($W \times W \times H$) glass cell, used for the experiments reported in the previous chapters. It is filled with degassed Na_2SO_4 electrolyte solution to provide a larger conductivity, $\sigma \approx 5 \text{ S m}^{-1}$.

Two constant-temperature plates at the top and at the bottom impose a temperature difference on the working fluid, like the Rayleigh-Bénard convection experiments described in Chapter 4. The magnetic blocks, described in Chapter 9, are placed underneath the lower copper plate. Copper, as non-ferro metal, will not influence the magnetic field lines. The obtained results can be thus compared to the visualisation experiments.

A liquid crystal sheet, described in Sect. 4.2.3, is mounted on the lower plate for near-wall temperature measurements. The complete set-up for the measurements

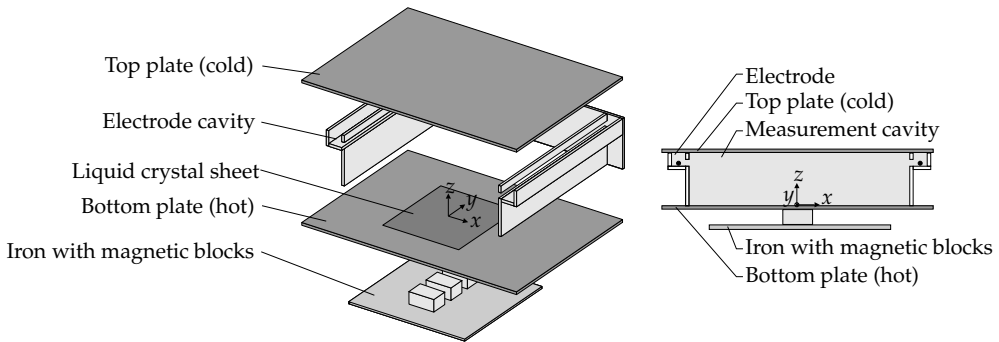


Figure 10.1: Exploded view (*left*) and side view (*right*) of the Rayleigh-Bénard cell.

reported in this chapter is depicted in Fig. 10.1.

10.1.1 Electromagnetic forcing

As the conductivity of the working fluid in this experiment is low ($\sigma \approx 5 \text{ S m}^{-1}$) and the magnetic permeability is very close to the permeability of vacuum ($\mu_0 = 1.23 \times 10^{-6} \text{ H m}^{-1}$), the magnetic Reynolds number Re_m is in the order of 10^{-6} . Moreover, by the use of permanent magnets $\partial \vec{B} / \partial t$ is zero. This leads to a simplification of the induction equation: $\nabla^2 \vec{B} = 0$. We recall, as in Chapter 9, that $\vec{j} \times \vec{B}$ is independent of any flow variable and thus the forcing is independent of the flow. The induced electric field is almost homogeneous in the horizontal directions near the bottom wall in the centre of the tank.

10.1.2 Particle image velocimetry

The velocity fields were measured by using a PIV system manufactured by ILA, which included a Continuum Minilite double-pulsed Nd:YAG laser with a pulse energy of 25 mJ. Neutrally buoyant hollow glass spheres with a size in the order of $10 \mu\text{m}$ were mixed in the working fluid in a concentration of approximately $1.0 \times 10^{-2} \text{ g l}^{-1}$. A PCO Sensicam camera was used to record the images, using a 55 mm lens with numerical aperture $f^\# = 4$. Snapshots are captured at a frequency of 2 Hz and for statistical analysis about 5000 frames are processed per configuration.

The PIV technique has been used to provide velocity data in x, z -planes in the middle of the tank, normal to both walls, as well as in x, y -planes parallel to the walls. For the x, z -plane measurements, two PCO cameras were used in combination with an algorithm to merge the two sides of the PIV images.

10.1.3 Liquid crystal thermography

On the bottom plate of the tank, a thermochromic liquid crystal sheet (Hallcrest, R30C5WA) with a measurable temperature range of 5 K was placed. Since the top wall of the RB cell is not transparent, a PCO Sencam colour camera was equipped with a tilt adapter to observe the liquid crystal sheet from the side through one of the glass walls. The optical setup obeys the Scheimpflug condition for sharp imaging, see also Fig. 4.5. Using an in-situ hue-versus-temperature calibration (Hay and Hollingsworth, 1998) and a perspective transformation, temperature fields on the bottom wall, i.e. the x, y -plane, could be determined accurately. It should be noted that the additional tilt of the camera reduces the effective viewing angle between the camera and the liquid crystal sheet, which results in a decrease of the measurable temperature range to approximately 2 K.

10.2 Results

10.2.1 Three magnet configuration

Electromagnetic forcing is introduced by placing three magnetic blocks with alternating polarity, i.e. North-South-North, under the RB cell. As a result of the changing poles of the magnets, two areas of attraction and repulsion are induced near the bottom wall. Between the middle (S) and the right (N) magnet a region of convergent Lorentz forces is generated: all $\vec{E}_L \sim \vec{j} \times \vec{B}$ vectors converge, see also the three magnet configuration in Fig. 4.8(b). In contrast, the Lorentz force vectors diverge between the middle (S) and the left (N) magnet. The resulting force is depicted in Fig. 10.2. The regions that are mainly influenced by the forcing are the areas between the magnetic blocks.

Side view

Fig. 10.3(a) depicts a side view of the obtained steady state. It is visualised by injecting disodium-fluorescein dye like in Chapter 9. We observed a region between the middle and the right magnet where the fluid is attracted to the wall. Due to the continuous inflow of mass, a vortex is generated marking the initiation of a steady flow along the wall. In the region between the left and middle magnet, the fluid is forced away from the wall and ejected in the bulk of the RB cell, as can be seen in Fig. 10.3(b). This mechanism can be seen as a non-intrusive transport mechanism to transfer heat towards or away from the wall.

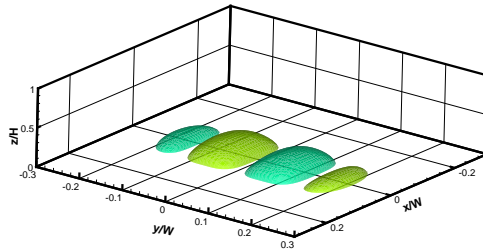
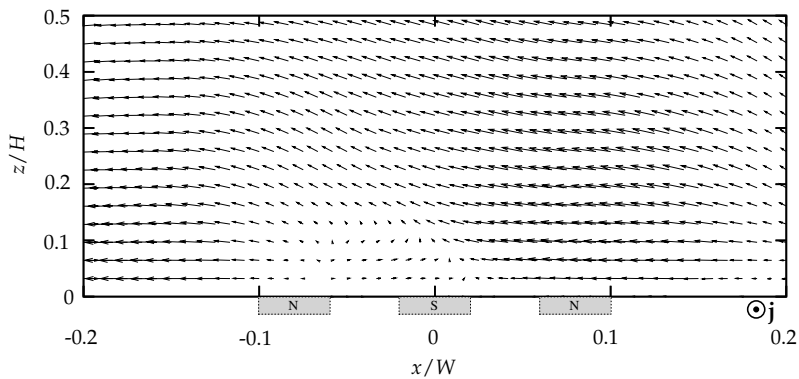


Figure 10.2: Calculated isosurfaces of 25% of the maximum longitudinal forcing $(\vec{j} \times \vec{B})_z$. Light and dark colours indicate opposing signs.



(a)



(b)

Figure 10.3: Side view of EM forced flow for $I = 1.0 \text{ A}$, $j = 10.8 \text{ A m}^{-2}$, $B_{\text{surf}} = 0.65 \text{ T}$. (a) Fluorescein visualisation, area of view: $223 \times 80 \text{ mm}^2$, (b) velocity field obtained using PIV. Rectangles indicate the magnetic blocks and both figures have the same scale.

Top view

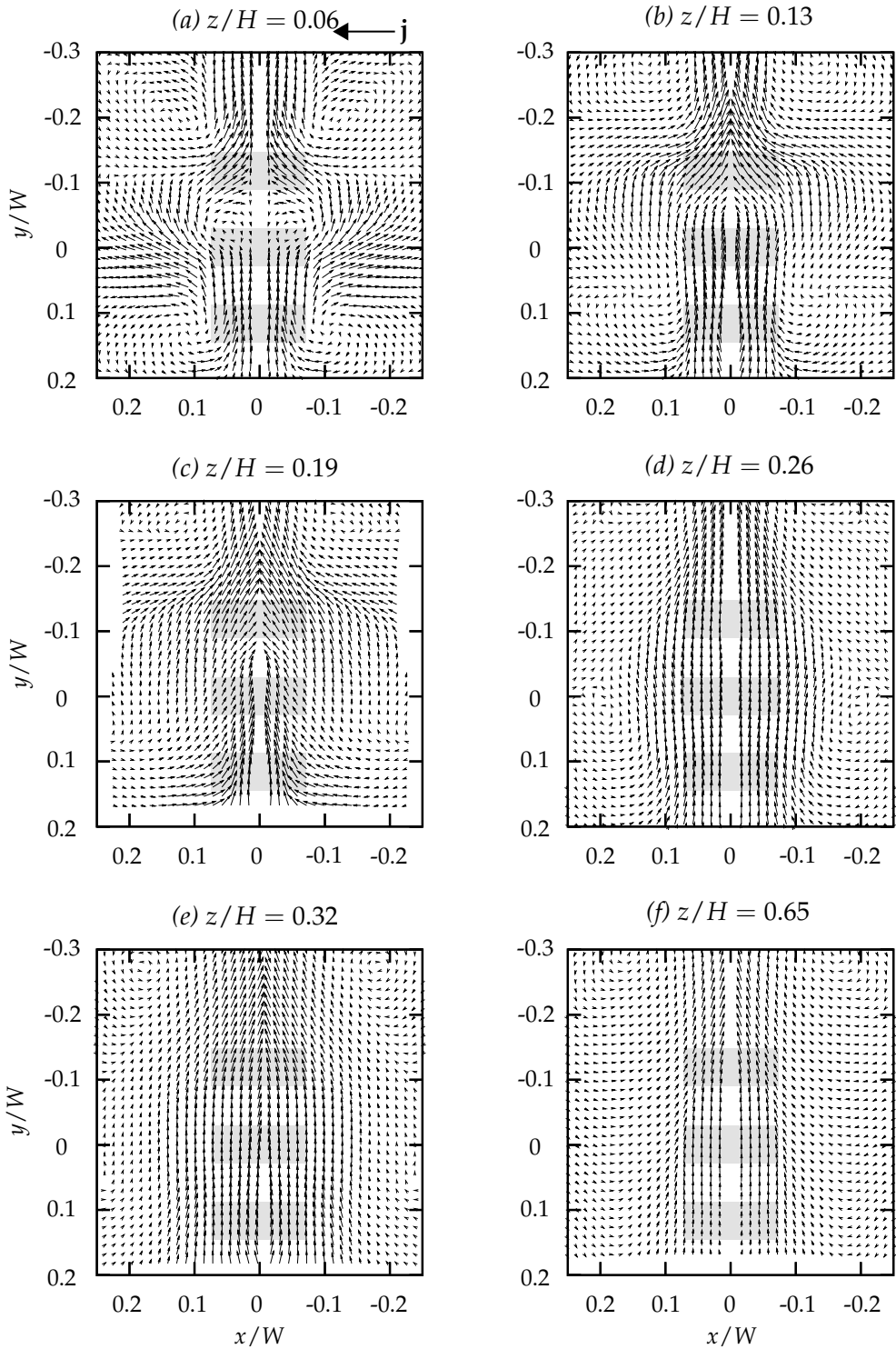
Figure 10.4 depicts the mean velocity fields at six different measurement planes above the bottom wall of a steady EM forced flow with $I = 0.5$ A. The mean fields are constructed by averaging 1500 individual PIV snapshots taken at 1 Hz. The measurements are performed in the right half of the domain. The figures are mirrored in the x, y -plane at $x = 0$ for easier understanding and the magnetic blocks, in N-S-N order, are indicated as gray rectangles.

It can be clearly seen that fluid is being accelerated in the region of the bottom (N) and the middle (S) magnet (Fig.10.4a). The flow then recirculates near the area of the divergent Lorentz forces, after which it accelerates again away from the top (N) magnetic block. The obvious decrease in strength of the forcing can be seen in Figs. 10.4(b)-(e). Further away from the bottom wall the flow field still has a main direction, but this is presumably caused by the limited size of the set-up (Fig. 10.4(f)). The typical velocities near the wall at $z/H = 0.02$ and further from the wall at $z/H = 0.22$ have been measured with laser Doppler anemometry and are in the order of 5 mm s^{-1} and 15 mm s^{-1} respectively for currents in the order of 1 A.

Comparison between PIV and LES

The horizontal velocity profiles at different vertical locations are shown in Fig. 10.5. Positive values of the horizontal velocity (indicating a recirculating flow pattern) are visible at 0.02 m from the bottom wall. The agreement between LES and PIV is good for all considered profiles. Some deviation between PIV and LES is visible in the proximity of the left wall, where the PIV values do not obey the exact no-slip boundary condition. This is due to experimental errors caused by the light reflection at the wall, and may be improved by painting all walls with a non-reflective material.

Figure 10.4: Top view of the mean velocity field of a locally forced flow. $I = 1.0$ A, $j = 10.8 \text{ A m}^{-2}$, $B_{\text{surf}} = 0.65$ T. Measurement planes with increasing distance from the bottom wall ($z = 0.01, 0.02, 0.03, 0.04, 0.05, 0.10$ m respectively). Rectangles indicate the positions of magnetic blocks. Figures are mirrored in the (y, z) plane at $x = 0$. The mean velocity ranges from 5 to 15 mm s^{-1} .



10.2.2 Two magnet configuration

Top view

The two-magnet configuration generates a well-defined swirling flow pattern, as was seen in Sect. 9.3.2. Fig. 10.6 shows a comparison between PIV and LES results for the two-magnet configuration with a relatively high current is imposed, $I = 10$ A, resulting in a well-developed turbulent flow. In addition to the main central vortical structure, a pair of smaller secondary vortical structures is also present, Fig. 10.6-top. The central vortical structure becomes nearly axi-symmetrical as the distance from the lower wall increases.

The time-averaged velocity fields from PIV and LES in the zoomed-in region denoted by a solid rectangle are shown in Fig. 10.6-bottom. Both PIV and LES show the strong vortical structure with identical size and velocity magnitude. The PIV shows a slightly asymmetrical distribution (slightly stronger downward motion at the left edge of the vortex compared to weaker upward motion along the left vortex edge), while the LES provides perfectly symmetrical distributions. The PIV measurements show a slightly stronger shear flow in the measurements near the wall.

Side view

The circumferentially averaged (from the centre towards the outer edge of the vortex) horizontal velocity magnitude profiles are shown in Fig. 10.7. It can be seen that the peak value stays constant with wall distance and its location moves more towards the outer edge of the vortex. For these profiles, there is again a good agreement between PIV and LES (especially with respect to the exact peak value), while some discrepancies are visible at locations towards the vortex edge.

The vertical profiles of the horizontal velocity at different locations ($x = -0.05$ m and $x = 0.05$ m) are shown in Fig. 10.8. Note that the measured vertical profiles do not span the entire height of the setup and consequently, velocity values are non-zero at the top locations. The locations of the velocity peak values in the proximity of the lower wall are reasonably well captured at both locations. Some deviations between PIV and LES can be observed in the upper part for $z > 0.075$ m at the first location $x = -0.050$ m. The velocity peak value is slightly underestimated at the second location $x = 0.05$ m, but the velocity profile trend is well captured.

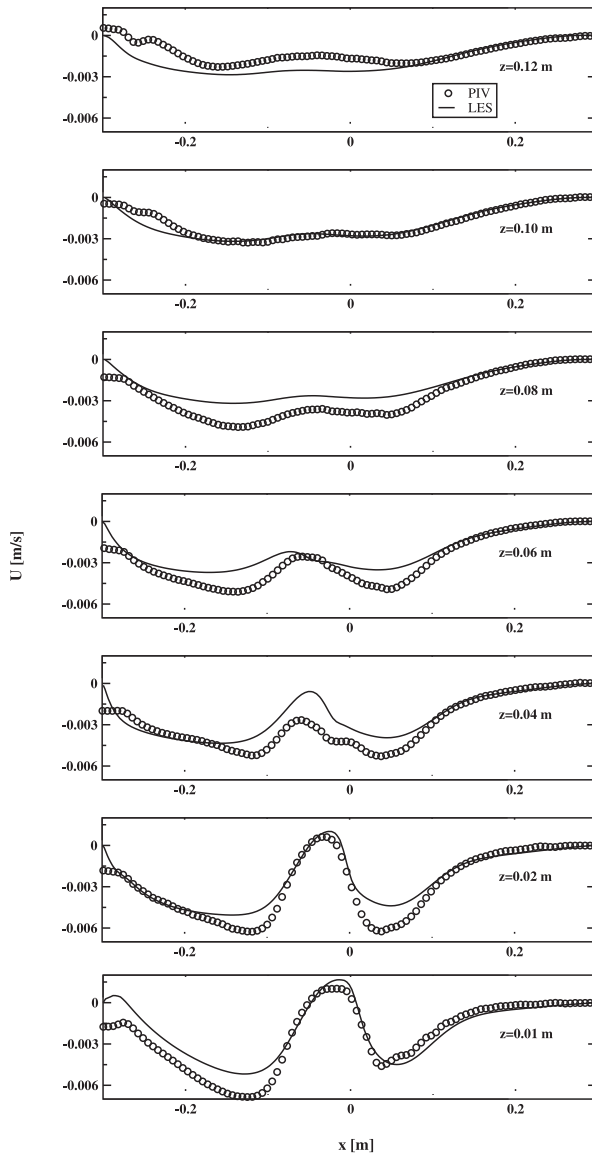


Figure 10.5: Horizontal velocity (u) profiles at different vertical distances from the bottom wall. Comparison between PIV (ring operator) and LES (minus). Configuration with 3-magnets. $B_{\text{surf}} = 0.65$ T and $I = 0.5$ A.

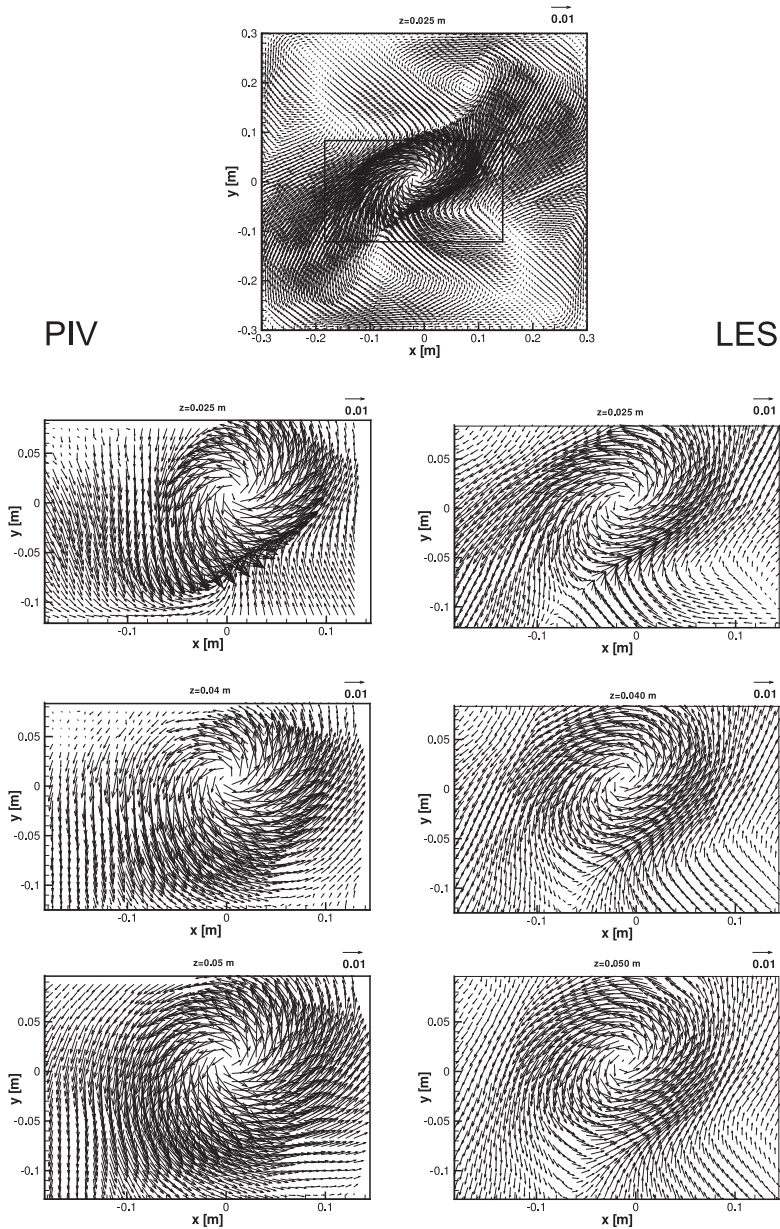


Figure 10.6: Velocity vector fields for the two magnet configuration in a horizontal plane at $z = 0.025$ m, $z = 0.040$ m, and $z = 0.050$ m. $B_{\text{surf}} = 0.65$ T, $I = 10$ A. Top figure: full field LES plane. Below: velocity fields for the marked region obtained with PIV (left) and LES (right).

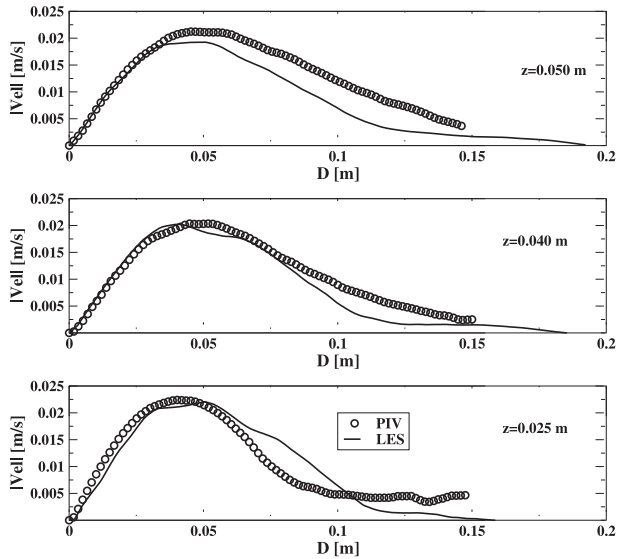


Figure 10.7: Comparison of the circumferentially averaged horizontal velocity magnitude ($|\vec{v}| = \sqrt{u^2 + v^2}$, along the vortex diameter ($D = \sqrt{x^2 + y^2}$) at different vertical wall distances for the 2-magnet configuration. ($B_{\text{surf}} = 0.65$ T, $I = 10$ A).

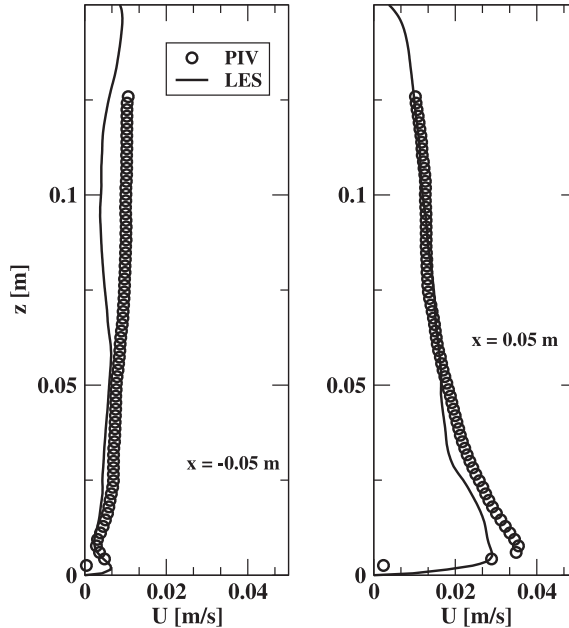


Figure 10.8: The vertical profiles of the horizontal velocity (u) at two characteristic locations, $x = -0.05, 0.05$ m. Configuration with 2-magnets ($B_{\text{surf}} = 1$ T, $I = 10$ A).

10.2.3 Rayleigh-Bénard convection with EM forced flow

Fig. 10.9 depicts an average temperature field for a thermal convection experiment subjected to the EM forcing. The temperature difference between the two walls is approximately 16 K, which results in $Ra = 4 \times 10^9$. The typical spoke patterns as earlier observed with liquid crystals (e.g. Theerthan and Arakeri, 2000) can be clearly seen in the instantaneous temperature fields. The acceleration found in the velocity fields matches the relatively cold region between the magnets in the negative y -direction. Cold fluid is attracted to the wall and locally cools the surface by approximately 0.4 K. The region is rather narrow, at maximum 10 percent of the magnetic blocks. When the flow is moving towards the area between the magnets in the positive y -direction, where the forcing is away from the wall, the flow diverges (Fig. 10.4a) and the cooling effect is reduced. The vortices just above the middle magnet cause a downward flow and reduce the heat transfer, which results in a rectangular cooling region just below the top magnetic block. Above this area, the spraying effect is at its maximum (Fig. 10.3(b)). Because the force on the fluid is pointing from the wall almost normally, there is no additional cooling. This leads to an increase of the temperature above the top (N) magnet (Fig. 10.9).

Comparing Figs. 10.4 and 10.9, it becomes clear that of the three cold spots along the side of the magnets, the top and bottom cold spots are directly induced by the Lorentz forcing near the wall, as the velocity pattern (Fig. 10.4(a)) is matching these two areas. However, the central cold spot cannot be attributed to this force. Fig. 10.4(d) shows that some vorticity is created in the plane $z/H = 0.26$, but this seems to be very weak and not exactly at the right position.

The relatively large current of 8 A is possibly the cause for the narrow region of cooling and dominant presence of the EM structures. Decreasing the current will probably lead to a more better balance between the electromagnetic and buoyant forces.

10.3 Conclusion

Velocity measurements are performed in the same two configurations that were considered in the visualisations in Chapter 9. The velocity fields confirm the findings of these earlier obtained visualisations, and show that after an initial phase, a steady flow is created above the EM forced region.

An comparison between PIV results and results of LES with electromagnetically extended subgrid closure showed a good agreement for both 2- and 3-magnets configurations. The 3-magnet configuration demonstrated that it can be used for effective

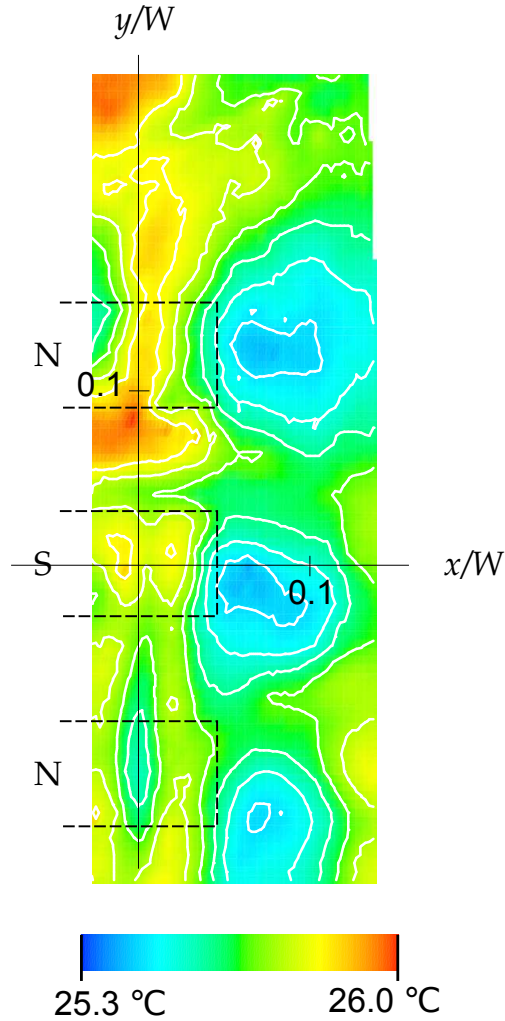


Figure 10.9: Average temperature field obtained from measurements near the hot wall during Rayleigh-Bénard convection subjected to local Lorentz forcing by 3 magnets. $\Delta T \approx 16$ K, $Ra = 4 \times 10^9$. $I = 8.0$ A, $B_{\text{surf}} = 0.65$ T. The rectangles indicate the position of the magnetic blocks.

modulation of the wall-boundary layers. The well-defined three-dimensional body force induced by the 2-magnets configuration can be used to put the entire tank into motion without any mechanical forcing through propellers or similar devices. This is of practical relevance for studies of fluid flow / EM interactions.

Moreover, temperature measurements were performed using liquid crystal thermography for a specific configuration of three magnets with alternating polarity. Direct effects of the applied EM forcing are identified in the temperature field such as local heating/cooling regions and the structure of the mean flow. The present results are dominated by the EM forcing. However, for a balance between thermal buoyancy and electromagnetic body forces, the used current should be reduced in future experiments.

11

Conclusion

As this thesis is for a large part a composition of individual papers, detailed conclusions and perspectives were given at the end of each chapter. This chapter summarises the main findings and general results.

Large-scale circulation

The experiments in Chapter 6 show that the time-averaged large-scale circulation in the aspect-ratio-four Rayleigh-Bénard convection cell consists of a flow around the periphery that encloses two co-rotating rolls. Using a phase resolving technique, it is shown that the growth and decay of the rolls produce a well-defined period in the velocity components that is maintained for a very long time. The sketch in Fig. 6.6 shows two extremes in the temporal evolution of the LSC with a phase difference of half a period, illustrating the nature of the oscillation in the aspect-ratio-four cell.

Using a large number of PIV realisations, the experiments reported in Chapter 8 show in detail the structure, and dynamics of the large-scale circulation in the aspect-ratio-four Rayleigh-Bénard convection cell. For $Ra < 10^8$, the RB convection in this geometry is characterised by isolated rolls. For higher Ra , two types of flow patterns consistently appear. Fig. 8.4 depicts a three-dimensional model of the LSC in which the observed co- and counter-rotating modes consistently fit. The model can be generalised to bounded RB convection systems with a broader range than the aspect-ratio-4 cell described in this work. It is presumably valid for $\Gamma = 3 - 8$, with the exception of the first mode that may differ for very large Γ .

Boundary layers in Rayleigh-Bénard convection

A combined numerical and experimental investigation of the boundary layers in RB convection in the aspect-ratio-4 cell filled with water is reported in Chapter 7. The study covers a wide range of Ra numbers varying between 7.0×10^4 and 2.4×10^9 . The results for the lower Ra numbers were obtained from direct numerical simulations, while those for the higher Ra numbers followed from laser Doppler anemometry. In the midrange, both techniques had an overlap of about one decade.

The probability density functions of the horizontal velocity components have a Gaussian-like shape for the complete Rayleigh number range, except at the lowest Ra where the flow is in a state of spatiotemporal chaos. Probability density functions that are scaled with the velocity rms value overlap for the entire Rayleigh number range, with the exception of the largest Rayleigh numbers where the large-scale circulation, or “wind”, is predominantly visible in the histograms.

The spectral density functions (sdfs) of the horizontal velocity component that were determined in the bulk flow and in the (kinetic) boundary layer are surprisingly similar. Sdfs in both regions of the flow are continuous and have a wide range of active scales for $Ra > 2.6 \times 10^6$. This indicates that both the bulk and the boundary layers are turbulent in the Rayleigh number range considered. However, molecular effects are still noticeable in the boundary layer and the boundary layer does not behave like a classical shear-driven turbulent boundary layer.

Electromagnetic forcing and control

In Chapters 9 and 10 an experimental investigation of the effects of electromagnetic forcing (EM) on an initially stationary conductive fluid layer is described. Two configurations have been studied: a 2-magnet configuration that can be used to generate a well-defined three-dimensional body force that can put the entire liquid bulk into motion without any mechanical stirring, and a 3-magnet configuration that demonstrates its use for effective modulation of the wall-boundary layers. Both are of significance to fundamental studies of interactions between fluid flow and electromagnetic fields.

Combined numerical (LES) and experimental studies (PIV) proves that the different combinations of permanent magnets and electrodes can be used for fundamental studies of electromagnetically driven flow, turbulence and heat transfer control. A good agreement was found between the LES simulations and PIV measurements. By changing the intensity of the imposed DC electric current, different flow regimes can be achieved. A particularly intriguing and interesting feature of the resulting flow is the simultaneous presence of different flow regimes in different parts of the setup.

In Chapter 10 the potential heat transfer modulation is experimentally validated. Direct effects of the applied EM forcing, such as local heating/cooling regions, and the structure of the mean flow are identified. The results also indicate a great potential in using magnetic fields for designing an efficient control on friction, heat and mass transfer in electrically conducting fluids.

Bibliography

- Absil, L. H. J. (1995). *Analysis of the laser Doppler measurement technique for application in turbulent flows*. PhD thesis, Delft University of Technology, Delft, The Netherlands.
- Adrian, R. J., Ferreira, R. T. D. S., and Boberg, T. (1986). Turbulent thermal convection in wide horizontal fluid layers. *Exp. Fluids*, 4(3):121–141.
- Adrian, R. J. and Yao, C.-S. (1985). Pulsed laser technique application to liquid and gaseous flows and the scattering power of seed materials. *Appl. Opt.*, 24:44–52.
- Akino, N., Kunugi, T., Ichimiya, K., Mitsushiro, K., and Ueda, M. (1989). Improved liquid-crystal thermometry excluding human color sensation. *J. Heat Trans.-T. ASME*, 111(2):558–565.
- Amati, G., Koal, K., Massaioli, F., Sreenivasan, K. R., and Verzicco, R. (2005). Turbulent thermal convection at high Rayleigh numbers for a Boussinesq fluid of constant Prandtl number. *Phys. Fluids*, 17(12):121701.
- Anderson, M. R. and Baughn, J. W. (2004). Hysteresis in liquid crystal thermography. *J. Heat Trans.-T. ASME*, 126(3):339–346.
- Arts, T. and Charbonnier, J.-M. (1994). *Measurement techniques in fluid dynamics; an introduction*, chapter 4. Temperature measurements, pages 139–144. Lecture series Von Karman Institute for Fluid Dynamics. Rhode Saint Gènesse, Von Karman Institute for Fluid Dynamics. VKI LS 1994-01.
- Barnett, D. O. and Bentley, H. T. (1974). Statistical bias of individual realization velocimeters. In *Proc. of the Second Intl. Workshop on Laser Velocimetry, Vol. 1*, pages 428–444.
- Baughn, J. W., Anderson, M. R., Mayhew, J. E., and Wolf, J. D. (1999). Hysteresis of thermochromic liquid crystal temperature measurement based on hue. *J. Heat Trans.-T. ASME*, 121(4):1067–1072.
- Behle, M., Schulz, K., Leiner, W., and Fiebig, M. (1996). Color-based image processing to measure local temperature distributions by wide-band liquid crystal thermography. *Appl. Sci. Res.*, 56(2-3):113–143.

- Bénard, H. (1901). *Les tourbillons cellulaires dans une nappe liquide propageant de la chaleur par convection en régime permanent*. PhD thesis, Université de Paris.
- Berkooz, G., Holmes, P., and Lumley, J. L. (1993). The proper orthogonal decomposition in the analysis of turbulent flows. *Annu. Rev. Fluid Mech.*, 25:539–575.
- Bird, R. B., Stewart, W. E., and Lightfoot, E. N. (2007). *Transport phenomena*. Wiley, New York, 2nd rev. edition.
- Bodenschatz, E., Pesch, W., and Ahlers, G. (2000). Recent developments in Rayleigh-Bénard convection. *Annu. Rev. Fluid Mech.*, 32:709–778.
- Boussinesq, J. V. (1901-1903). *Théorie analytique de la Chaleur*, volume 1 and 2. Gauthier-Villars, Paris.
- Brown, E. and Ahlers, G. (2006a). Effect of the Earth's Coriolis force on the large-scale circulation of turbulent Rayleigh-Bénard convection. *Phys. Fluids*, 18(12):5108.
- Brown, E. and Ahlers, G. (2006b). Rotations and cessations of the large-scale circulation in turbulent Rayleigh-Bénard convection. *J. Fluid Mech.*, 568(0):351–386.
- Brown, E. and Ahlers, G. (2007). Large-scale circulation model for turbulent Rayleigh-Bénard convection. *Phys. Rev. Lett.*, 98:134501.
- Camussi, R. and Verzicco, R. (1998). Convective turbulence in mercury: Scaling laws and spectra. *Phys. Fluids*, 10(2):516–527.
- Castaing, B., Gunaratne, G., Heslot, F., Kadanoff, L., Libchaber, A., Thomae, S., Wu, X.-Z., Zaleski, S., and Zanetti, G. (1989). Scaling of hard thermal turbulence in Rayleigh-Bénard convection. *J. Fluid Mech.*, 204(0):1–30.
- Cerisier, P., Sylvain, J. D., and Dauby, P. (2002). Application of the laser beam deflection to the study of temperature fields in Rayleigh-Bénard convection. *Exp. Fluids*, 33(3):391–397.
- Chavanne, X., Chillà, F., Castaing, B., Hébral, B., Chabaud, B., and Chaussy, J. (1997). Observation of the ultimate regime in Rayleigh-Bénard convection. *Phys. Rev. Lett.*, 79(19):3648–3651.
- Chavanne, X., Chillà, F., Chabaud, B., Castaing, B., and Hébral, B. (2001). Turbulent Rayleigh-Bénard convection in gaseous and liquid He. *Phys. Fluids*, 13(5):1300–1320.
- Ching, E. S. C., Guo, H., Shang, X. D., Tong, P., and Xia, K.-Q. (2004). Extraction of plumes in turbulent thermal convection. *Phys. Rev. Lett.*, 93(12):124501.
- Ching, E. S. C., Leung, C. K., Qiu, X.-L., and Tong, P. (2003). Intermittency of velocity fluctuations in turbulent thermal convection. *Phys. Rev. E*, 68(2):026307.

- Chu, T. Y. and Goldstein, R. J. (1973). Turbulent convection in a horizontal layer of water. *J. Fluid Mech.*, 60(1):141–159.
- Ciliberto, S., Cioni, S., and Laroche, C. (1996). Large-scale flow properties of turbulent thermal convection. *Phys. Rev. E*, 54(6):R5901–R5904.
- Ciofalo, M., Signorino, M., and Simiano, M. (2003). Tomographic particle-image velocimetry and thermography in Rayleigh-Bénard convection using suspended thermochromic liquid crystals and digital image processing. *Exp. Fluids*, 34(2):156–172.
- Collings, P. J. and Patel, J. S. (1997). *Handbook of Liquid Crystal Research*. Oxford University Press.
- Coolen, M. C. J., Kieft, R. N., Rindt, C. C. M., and van Steenhoven, A. A. (1999). Application of 2-D LIF temperature measurements in water using a Nd:YAG laser. *Exp. Fluids*, 27(5):420–426.
- Crawford, C. H. and Karniadakis, G. E. (1997). Reynolds stress analysis of EMHD-controlled wall turbulence. Part I. Streamwise forcing. *Phys. Fluids*, 9(3):788–806.
- Dabiri, D. (2009). Digital particle image thermometry/velocimetry: a review. *Exp. Fluids*, 46:191–241.
- Dabiri, D. and Gharib, M. (1996). The effects of forced boundary conditions on flow within a cubic cavity using digital particle image thermometry and velocimetry (DPITV). *Exp. Therm. Fluid Sci.*, 13(4):349–363.
- Davidson, P. A. (2001). *An introduction to magnetohydrodynamics*. Cambridge texts in applied mathematics. Cambridge University Press.
- Davis, A. H. (1922). Natural convective cooling in fluids. *Philosophical Magazine*, 44(263):920–940.
- Deane, A. E. and Sirovich, L. (1991). A computational study of Rayleigh-Bénard convection. Part 1. Rayleigh-number scaling. *J. Fluid Mech.*, 222:231–250.
- Du, Y.-B. and Tong, P. (2000). Turbulent thermal convection in a cell with ordered rough boundaries. *J. Fluid Mech.*, 407(0):57–84.
- Elser, W. and Ennulat, R. D. (1976). Selective reflection of cholesteric liquid crystals. In Brown, G. H., editor, *Advances in Liquid Crystals*, volume 2, pages 73–172, London. Academic Press.
- Ferguson, J. L. (1968). Liquid crystals in nondestructive testing. *Appl. Optics*, 7(9):1729–1737.
- Fitzjarrald, D. E. (1976). An experimental study of turbulent convection in air. *J. Fluid Mech.*, 73(FEB24):693–719.

- Fujisawa, N. and Funatani, S. (2004). Simultaneous measurement of temperature and velocity in a turbulent thermal convection by the extended range scanning liquid crystal visualization technique. *Exp. Fluids*, 29(7):S158–S165.
- Fujisawa, N., Funatani, S., and Katoh, N. (2005). Scanning liquid-crystal thermometry and stereo velocimetry for simultaneous three-dimensional measurement of temperature and velocity field in a turbulent Rayleigh-Bénard convection. *Exp. Fluids*, 38(3):291–303.
- Fujisawa, N. and Hashizume, Y. (2001). An uncertainty analysis of temperature and velocity measured by a liquid crystal visualization technique. *Meas. Sci. Technol.*, 12(8):1235–1242.
- Funatani, S., Fujisawa, N., and Ikeda, H. (2004). Simultaneous measurement of temperature and velocity using two-colour LIF combined with PIV with a colour CCD camera and its application to the turbulent buoyant plume. *Meas. Sci. Technol.*, 15(5):983–900.
- Funfschilling, D. and Ahlers, G. (2004). Plume motion and large-scale circulation in a cylindrical Rayleigh-Bénard cell. *Phys. Rev. Lett.*, 92(19):194502.
- Funfschilling, D., Brown, E., Nikolaenko, A., and Ahlers, G. (2005). Heat transport by turbulent Rayleigh-Bénard convection in cylindrical samples with aspect ratio one and larger. *J. Fluid Mech.*, 536(1):145–154.
- Geers, L. F. G. (2004). *Multiple impinging jet arrays: an experimental study on flow and heat transfer*. PhD thesis, Delft University of Technology.
- Getling, A. V. (1998). *Rayleigh-Bénard convection*. Advanced series in nonlinear dynamics II. World Scientific, Singapore, Singapore.
- Gluckman, B. J., Williams, H., and Gollub, J. P. (1996). Geometry of isothermal and isoconcentration surfaces in thermal turbulence. *Phys. Fluids A*, 5(3):647–661.
- Grewal, G. S., Bharara, M., Cobb, J. E., Dubey, V. N., and Claremont, D. J. (2006). A novel approach to thermochromic liquid crystal calibration using neural networks. *Meas. Sci. Tech.*, 17(7):1918–1924.
- Griffiths, D. J. (1989). *Introduction to electrodynamics*. Prentice-Hall, Englewood Cliffs, 2nd edition.
- Grossmann, S. and Lohse, D. (2000). Scaling in thermal convection: a unifying theory. *J. Fluid Mech.*, 407(0):27–56.
- Grossmann, S. and Lohse, D. (2001). Thermal convection for large Prandtl numbers. *Phys. Rev. Lett.*, 86(15):3316–3319.

- Grossmann, S. and Lohse, D. (2003). On geometry effects in Rayleigh-Bénard convection. *J. Fluid Mech.*, 486(0):105–114.
- Günther, A. and Rudolf von Rohr, P. (2002a). Influence of the optical configuration on temperature measurements with fluid-dispersed TLCs. *Exp. Fluids*, 32(5):533–541.
- Günther, A. and Rudolf von Rohr, P. (2002b). Structure of the temperature field in a flow over heated waves. *Exp. Fluids*, 33(6):920–930.
- Hanjalić, K. (2005). Synergy of experiments and computer simulations in research of turbulent convection. *Int. J. Heat Fluid Fl.*, 26(6):828–842.
- Hanjalić, K. and Kenjereš, S. (2000). Reorganization of turbulence structure in magnetic Rayleigh-Bénard convection: a T-RANS study. *J. Turb.*, 1(8):22pp. 22 pp.
- Hay, J. L. and Hollingsworth, D. K. (1996). A comparison of trichromic systems for use in the calibration of polymer-dispersed thermochromic liquid crystals. *Exp. Therm. Fluid Sci.*, 12(1):1–12.
- Hay, J. L. and Hollingsworth, D. K. (1998). Calibration of micro-encapsulated liquid crystals using hue angle and a dimensionless temperature. *Exp. Therm. Fluid Sci.*, 18(3):251–257.
- He, X. and Tong, P. (2009). Measurements of the thermal dissipation field in turbulent Rayleigh-Bénard convection. *Phys. Rev. E*, 79:026306.
- Hecht, E. (1998). *Optics*. Addison-Wesley, Reading, 3rd edition.
- Hekker, S. (2003). Temperature measurements in Rayleigh-Bénard convection using suspended liquid crystals. Master's thesis, Delft University of Technology, Department of Applied Sciences, Thermal and Fluids Sciences.
- Henoch, C. and Stace, J. (1995). Experimental investigation of a salt water turbulent boundary layer modified by an applied streamwise magnetohydrodynamic body force. *Phys. Fluids*, 7(6):1371–1383.
- Heslot, F., Castaing, B., and Libchaber, A. (1987). Transitions to turbulence in helium gas. *Phys. Rev. A*, 36(12):5870–5873.
- Hiller, W. J., Koch, S., and Kowalewski, T. A. (1989). Three-dimensional structures in laminar natural convection in a cubic enclosure. *Exp. Therm. Fluid Sci.*, 2(1):34–44.
- Hiller, W. J., Koch, S., Kowalewski, T. A., and Stella, F. (1993). Onset of natural-convection in a cube. *Int. J. Heat Mass Tran.*, 36(13):3251–3263.
- Hiller, W. J. and Kowalewski, T. A. (1986). Simultaneous measurement of temperature and velocity fields in thermal convective flows. In Véret, C., editor, *Flow Visualization IV, Proc. of the 4th Int. Symp. on Flow Vis., August 26-29, 1986*, pages 617–622.

- Hoesel, W. and Rodi, W. (1977). New biasing elimination method for laser-Doppler velocimeter counter processing. *Rev. Sci. Instrum.*, 48(7):910.
- Howard, L. N. (1963). Heat transport by turbulent convection. *J. Fluid Mech.*, 17(3):405–432.
- Howard, L. N. (1964). Convection at high Rayleigh numbers. In *Proceedings of the 11th International Congress on Applied Mechanics*, pages 1109–1115, Berlin. Springer-Verlag.
- Ireland, P. T. and Jones, T. V. (1987). The response time of a surface thermometer employing encapsulated thermochromic liquid crystals. *J. Phys. E*, 20(10):1195–1199.
- Jackson, J. D. (1999). *Classical electrodynamics*. Wiley, New York, 3rd edition.
- Janssen, L. P. B. M. and Warmoeskerken, M. M. C. G. (1997). *Transport phenomena data companion*. Delftse Universitaire pers, Delft, 3rd edition.
- Kadanoff, L. P. (2001). Turbulent heat flow: Structures and scaling. *Physics Today*, 54(8):34–39.
- Kasagi, N., Moffat, R. J., and Hirata, M. (2001). *Flow visualization*, chapter 8. Liquid crystals, pages 111–129. Taylor & Francis, 2nd edition.
- Keane, R. and Adrian, R. J. (1990). Optimization of particle image velocimeters. Part I: Double pulsed systems. *Meas. Sci. Tech.*, 1:1202–1215.
- Keane, R. D. and Adrian, R. J. (1992). Theory of cross-correlation analysis of PIV images. *Applied Scientific Research*, 49(3):191–215.
- Kenjereš, S. and Hanjalić, K. (2004). Numerical simulation of magnetic control of heat transfer in thermal convection. *Int. J. Heat Fluid Fl.*, 25(3):559–568.
- Kenjereš, S., Verdool, J., Tummers, M. J., Hanjalić, K., and Kleijn, C. R. (2009). Numerical and experimental study of electromagnetically driven vortical flows. *Int. J. Heat Fluid Flow*, 30(3):494–504.
- Kerr, R. M. (1996). Rayleigh number scaling in numerical convection. *J. Fluid Mech.*, 310:139–179.
- Khoo, I.-C. (1995). *Liquid crystals: physical properties and nonlinear optical phenomena*. Wiley Interscience.
- Kittel, C. (1996). *Introduction to Solid State Physics*. Wiley, New York, 7th edition.
- Kobayashi, T. and Saga, T. (1998). Time response characteristics of microcapsulated liquid-crystal particles. *Heat Transfer - Japanese Research*, 27(5):390–398.

- Kowalewski, T. A. (1999). Measurement of temperature and velocity of freezing water using liquid crystal tracers. In K. Hutter, Y. W. and Beer, H., editors, *Advances in Cold-Region Thermal Engineering and Sciences*, volume 533 of *Lecture Notes in Physics*, pages 83–90. Springer Verlag, Berlin.
- Kowalewski, T. A. and Stasiek, J. (1998). Thermochromic liquid crystals in heat transfer research. In *Prace Nauk. Polit. Wrocl.*, Swieradow. Invited paper at Heat Mass Transfer Conference.
- Kraichnan, R. H. (1962). Turbulent thermal convection at arbitrary Prandtl number. *Phys. Fluids*, 5(11):1374–1389.
- Krishnamurti, R. (1995). Low frequency oscillations in turbulent Rayleigh-Bénard convection: laboratory experiments. *Fluid Dyn. Res.*, 16(2–3):87–108.
- Krishnamurti, R. (2000). Low frequency oscillation in turbulent convection. *Ann. N.Y. Acad. Sci.*, 898(1):122–126.
- Krishnamurti, R. and Howard, L. N. (1981). Large-scale flow generation in turbulent convection. *Proceedings of the National Academy of Sciences of the United States of America*, 78(4):1981–1985.
- Kruse, N. and Rudolf von Rohr, P. (2006). Structure of turbulent heat flux in a flow over a heated wavy wall. *Int. J. Heat Mass Tran.*, 49(19–20):3514–3529.
- Libchaber, A. (1987). From chaos to turbulence in Bénard convection. *Proceedings of the Royal Society of London Series A-Mathematical and Physical Sciences*, 413(1844):63–69.
- Lide, D. R. (2006). *CRC Handbook of chemistry and physics : a ready-reference book of chemical and physical data*. Boca Raton : CRC Press, 87th edition.
- Liu, Z., Adrian, R. J., and Hanratty, T. (2001). Large-scale modes of turbulent channel flow: transport and structure. *J. Fluid Mech.*, 448:53–80.
- Lutjen, P. M., Mishra, D., and Prasad, V. (2001). Three-dimensional visualization and measurement of temperature field using liquid crystal scanning thermography. *J. Heat Trans.-T. ASME*, 123(5):1006–1014.
- Malkus, W. V. R. (1954a). Discrete transitions in turbulent convection. *Proceedings of the Royal Society of London: Series A - Mathematical and Physical Sciences*, 225(1161):185–195.
- Malkus, W. V. R. (1954b). The heat transport and spectrum of thermal turbulence. *Proceedings of the Royal Society of London. Series A, Mathematical and Physical Sciences*, 225(1161):192–212.

- McLaughlin, D. K. and Tiederman, W. G. (1973). Biasing correction for individual realization of laser anemometer measurements in turbulent flows. *Phys. Fluids*, 16(7):2082.
- Moffat, R. J. (1990). Some experimental methods for heat transfer studies. *Exp. Therm. Fluid Sci.*, 3(1):14–32.
- Moreau, R. (1990). *Magnetohydrodynamics*. Fluid mechanics and its applications. Kluwer Academic Publishers, Dordrecht.
- Mouri, H., Takaoka, M., Hori, A., and Kawashima, Y. (2002). Probability density function of turbulent velocity fluctuations. *Phys. Rev. E*, 65(5):056304.
- Niemela, J. J., Skrbek, L., Sreenivasan, K. R., and Donnelly, R. (2000). Turbulent convection at very high Rayleigh numbers. *Nature*, 404(6780):837–840.
- Niemela, J. J., Skrbek, L., Sreenivasan, K. R., and Donnelly, R. J. (2001). The wind in confined thermal convection. *J. Fluid Mech.*, 449(0):169–178.
- Niemela, J. J. and Sreenivasan, K. R. (2006). Turbulent convection at high Rayleigh numbers and aspect ratio 4. *J. Fluid Mech.*, 557:411–422.
- Nieuwstadt, F. T. M. (1998). *Turbulentie, inleiding in de theorie en toepassingen van turbulente stromingen*. Number 24 in Epsilon uitgaven. Epsilon uitgaven, 2nd edition.
- Park, H. and Sirovich, L. (1990). Turbulent thermal convection in a finite domain: Part II. Numerical results. *Phys. Fluids A*, 2(9):1659–1668.
- Park, H. G., Dabiri, D., and Gharib, M. (2001). Digital particle image velocimetry/thermometry and application to the wake of a heated circular cylinder. *Exp. Fluids*, 30(3):327–338.
- Parsley, M. (1991). *Handbook of Thermochromic Liquid Crystal Technology*. Hallcrest, Glenview, IL, US.
- Petrie, H. L., Samimy, M., and Addy, A. L. (1988). Laser Doppler velocity bias in separated turbulent flows. *Exp. Fluids*, 6(2):80–88.
- Pope, S. B. (2000). *Turbulent flows*. Cambridge University Press, Cambridge, UK.
- Pottebaum, T. S. and Gharib, M. (2004). The pinch-off process in a starting buoyant plume. *Exp. Fluids*, 37(1):87–94.
- Praisner, T. J., Sabatino, D. R., and Smith, C. R. (2001). Simultaneously combined liquid crystal heat transfer and PIV flow-field measurements. *Exp. Fluids*, 30(1):1–10.
- Prasad, A. K. and Gonuguntla, P. V. (1996). Turbulence measurements in nonpenetrative thermal convection. *Phys. Fluids*, 8(9):2460–2470.

- Priestley, M. B. (1981). *Spectral Analysis and Time Series, volume 1: Univariate Series*. Probability and Mathematical Statistics. Academic Press, New York, 1st edition.
- Puthenveetil, B. A., Ananthakrishna, G., and Arakeri, J. H. (2005). The multifractal nature of plume structure in high-rayleigh-number convection. *J. Fluid Mech.*, 526(0):245–256.
- Qiu, X.-L., Shang, X. D., Tong, P., and Xia, K.-Q. (2004). Velocity oscillations in turbulent Rayleigh-Bénard convection. *Phys. Fluids*, 16(2):412–423.
- Qiu, X.-L. and Tong, P. (2001). Large-scale velocity structures in turbulent thermal convection. *Phys. Rev. E*, 64(3):036304.
- Qiu, X.-L. and Tong, P. (2002). Temperature oscillations in turbulent Rayleigh-Bénard convection. *Phys. Rev. E*, 66(2):026308.
- Qiu, X.-L. and Xia, K.-Q. (1998a). Spatial structure of the viscous boundary layer in turbulent convection. *Phys. Rev. E*, 58(5):5816–5820.
- Qiu, X.-L. and Xia, K.-Q. (1998b). Viscous boundary layers at the sidewall of a convection cell. *Phys. Rev. E*, 58(1):486–491.
- Qiu, X.-L., Yao, S. H., and Tong, P. (2000). Large-scale coherent rotation and oscillation in turbulent thermal convection. *Phys. Rev. E*, 61(6):R6075–R6078.
- Raffel, M., Willert, C., and Klompenhaus, J. (1998). *Particle Image Velocimetry, a practical guide*. Experimental Fluid Mechanics. Springer, Berlin. 253pp.
- Raffel, M., Willert, C. E., Wereley, S. T., , and Klompenhaus, J. (2007). *Particle Image Velocimetry, a practical guide*. Experimental Fluid Mechanics. Springer, Berlin, 2nd edition. 448pp.
- Rayleigh, L. (1916). On convection currents in a horizontal layer of fluid, when the higher temperature is on the under side. *Philosophical Magazine Series 6*, 32(192):529–546.
- Resagk, C., du Puits, R., Thess, A., Dolzhansky, F., Grossmann, S., Araujo, F. F., and Lohse, D. (2006). Oscillations of the large scale wind in turbulent thermal convection. *Phys. Fluids*, 18(9):095105.
- Roberts, G. T. and East, R. A. (1996). Liquid crystal thermography for heat transfer measurement in hypersonic flows: A review. *J. Spacecraft Rockets*, 33(6):761–768.
- Rossi, L. (2001). *Contrôle Électromagnétique d'écoulement en eau de mer*. PhD thesis, Université Joseph Fourier, Grenoble.
- Rossi, L. and Thibault, J.-P. (2002). Investigation of wall normal electromagnetic actuator for seawater flow control. *J. Turb.*, 3(5).

- Roth, W. A. and Scheel, K. (1923). *Landolt-Börnstein physikalisch-chemische Tabellen*. Springer, Berlin, 5th edition.
- Sabatino, D. R., Praisner, T. J., and Smith, C. R. (2000). A high-accuracy calibration technique for thermochromic liquid crystal temperature measurements. *Exp. Fluids*, 28(6):497–505.
- Sano, M., Wu, X. Z., and Libchaber, A. (1989). Turbulence in helium-gas free convection. *Phys. Rev. A*, 40(11):6421–6430.
- Scarano, F. and Riethmuller, M. L. (1999). Iterative multigrid approach in PIV image processing with discrete window offset. *Exp. Fluids*, 26(6):513–523.
- Scarano, F. and Riethmuller, M. L. (2000). Advances in iterative multigrid PIV image processing. *Exp. Fluids*, 29(7):S051–S060.
- Schlichting, H. and Gersten, K. (1997). *Grenzschicht-Theorie*. Springer-Verlag Berlin Heidelberg, 9th edition.
- Seuntjens, H. J., Kieft, R. N., Rindt, C. C. M., and van Steenhoven, A. A. (2001). 2D temperature measurements in the wake of a heated cylinder using LIF. *Exp. Fluids*, 31(5):588–595.
- Shang, X.-D., Qiu, X.-L., Tong, P., and Xia, K.-Q. (2003). Measured local heat transport in turbulent rayleigh-bénard convection. *Phys. Rev. Lett.*, 90(7):074501.
- Shepard, D. (1968). A two-dimensional interpolation function for irregularly-spaced data. In *Proceedings of the 1968 23rd ACM national conference*. ACM New York, NY, USA.
- Siggia, E. D. (1994). High Rayleigh number convection. *Annu. Rev. Fluid Mech.*, 26(0):137–168.
- Sirovich, L. (1987). Turbulence and the dynamics of coherent structures: I - Coherent structures, II - Symmetries and transformations, III - Dynamics and scaling. *Q. Appl. Math.*, 45(3):561–590.
- Sirovich, L. and Deane, A. E. (1991). A computational study of Rayleigh-Bénard convection. Part 2. Dimension considerations. *J. Fluid Mech.*, 222:251–265.
- Sirovich, L. and Park, H. (1990). Turbulent thermal convection in a finite domain: Part I. Theory. *Phys. Fluids A*, 2:1649–1655.
- Solomon, T. H. and Gollub, J. P. (1990). Sheared boundary layers in turbulent Rayleigh-Bénard convection. *Phys. Rev. Lett.*, 64(20):2382–2385.
- Sreenivasan, K. R., Bershadskii, A., and Niemela, J. J. (2002). Mean wind and its reversal in thermal convection. *Phys. Rev. E*, 65(05):056306–056309.

- Stasiek, J. (1997). Thermochromic liquid crystals and true colour image processing in heat transfer and fluid-flow research. *Heat Mass Transfer*, 33(1–2):27–39.
- Stasiek, J. A. and Kowalewski, T. A. (2002). Thermochromic liquid crystals applied for heat transfer research. *Opto.-Electron. Rev.*, 10(1):1–10.
- Sun, C., Xi, H.-D., and Xia, K.-Q. (2005a). Azimuthal symmetry, flow dynamics, and heat transport in turbulent thermal convection in a cylinder with an aspect ratio of 0.5. *Phys. Rev. Lett.*, 95(07):4502–4505.
- Sun, C., Xia, K.-Q., and Tong, P. (2005b). Three-dimensional flow structures and dynamics of turbulent thermal convection in a cylindrical cell. *Phys. Rev. E*, 72(2):026302.
- Sun, J. H., Leong, K. C., and Liu, C. Y. (1997). Influence of hue origin on the hue-temperature calibration of thermochromic liquid crystals. *Heat Mass Transfer*, 33(1–2):121–127.
- Tennekes, H. and Lumley, J. L. (1972). *A first course in turbulence*. MIT Press.
- Theerthan, S. A. and Arakeri, J. H. (1998). A model for near-wall dynamics in turbulent Rayleigh-Bénard convection. *J. Fluid Mech.*, 373(0):221–254.
- Theerthan, S. A. and Arakeri, J. H. (2000). Planform structure and heat transfer in turbulent free convection over horizontal surfaces. *Phys. Fluids*, 12(4):884–894.
- Tong, P. and Shen, Y. (1992). Relative velocity fluctuations in turbulent Rayleigh-Bénard convection. *Phys. Rev. Lett.*, 69(14):2066–2069.
- Travis, D. (1990). *Effective Color Displays: Theory and Practice*. Academic Press.
- Tropea, C., Foss, J. F., and Yarin, A. L., editors (2007). *Springer handbook of experimental fluid mechanics*. Springer, Berlin.
- Tummers, M. J. (1999). *Investigation of a Turbulent Wake in an Adverse Pressure Gradient using Laser Doppler Anemometry*. PhD thesis, Delft University of Technology.
- Tummers, M. J. and Passchier, D. M. (2001). Spectral analysis of biased LDA data. *Meas. Sci. Technol.*, 12(10):1641–1650.
- van Reeuwijk, M. (2007). *Direct simulation and regularization modeling of turbulent thermal convection*. Dissertation, Delft University of Technology.
- van Reeuwijk, M., Jonker, H. J. J., and Hanjalić, K. (2005). Identification of the wind in Rayleigh-Bénard. *Phys. Fluids*, 17(5):051704.
- van Reeuwijk, M., Jonker, H. J. J., and Hanjalić, K. (2008a). Wind and boundary layers in Rayleigh-Bénard convection. I. Analysis and modeling. *Phys. Rev. E.*, 77:036311.

- van Reeuwijk, M., Jonker, H. J. J., and Hanjalić, K. (2008b). Wind and boundary layers in Rayleigh-Bénard convection. II. Boundary layer character and scaling. *Phys Rev. E.*, 77:036312.
- Verdoold, J., Rossi, L., Tummers, M. J., and Hanjalić, K. (2003). Towards electromagnetic control of thermal convection. In *Proceedings of the 7th International Symposium on Fluid control, measurement and visualization*.
- Verdoold, J., Tummers, M. J., and Hanjalić, K. (2006a). Oscillating large-scale circulation in turbulent Rayleigh-Bénard convection. *Phys. Rev. E*, 73(5):056304.
- Verdoold, J., Tummers, M. J., and Hanjalić, K. (2009). Prime modes of circulation in large-aspect-ratio turbulent Rayleigh-Bénard convection. *Phys. Rev. E*, 80(3):037301.
- Verdoold, J., van Reeuwijk, M., Tummers, M. J., Jonker, H. J. J., and Hanjalić, K. (2008). Spectral analysis of boundary layers in Rayleigh-Bénard convection. *Phys. Rev. E*, 77(1):016303.
- Verdoold, J., Wibowo, A. B., Tummers, M. J., and Hanjalić, K. (2006b). Electromagnetic control of Rayleigh-Bénard convection. In Hanjalić, K., Nagano, Y., and Jakirlić, S., editors, *Fifth Symposium on Turbulence, Heat and Mass Transfer, Dubrovnik, Croatia, September 25-29, 2006*. Begell House.
- Verdoold, J., Witte, P., Hoek, L., Tummers, M. J., and Hanjalić, K. (2005). Identification and electromagnetic control of structures in Rayleigh-Bénard convection. In Humphrey, J. A. C., Gatski, T. B., Eaton, J. K., Friedrich, R., Kasagi, N., and Leschziner, M. A., editors, *Fourth International Symposium on Turbulence and Shear Flow Phenomena, Williamsburg USA 27-29 June, 2005*, volume 3, pages 1107–1112. Elsevier.
- Verstappen, R. W. C. P. and Veldman, A. E. P. (2003). Symmetry-preserving discretization of turbulent flow. *J. Comput. Phys.*, 187(1):343–368.
- Villermaux, E. (1995). Memory induced low frequency oscillations in closed convection boxes. *Phys. Rev. Lett.*, 75(25):4618–4621.
- Vincent, A. and Meneguzzi, M. (1991). The spatial structure and statistical properties of homogeneous turbulence. *J. Fluid Mech.*, 225:1–20.
- Watanabe, Y., Hashizume, Y., and Fujisawa, N. (2007). Temperature measurement by two-color LIF technique using Nd:YAG lasers. *Journal of Visualization*, 10(4):343–344.
- Weier, T., Gerbeth, G., Mutschke, G., Platacis, E., and Lielausis, O. (1998). Experiments on cylinder wake stabilization in an electrolyte solution by means of electromagnetic forces localized on the cylinder surface. *Exp. Therm. Fluid Sci.*, 16(1–2):84–91.

- Westerweel, J. (1993). *Digital Particle Image Velocimetry - Theory and Applications*. PhD thesis, Delft University of Technology, Delft.
- Westerweel, J. (1994). Efficient detection of spurious vectors in particle image velocimetry data. *Exp. Fluids*, 16:236–247.
- Westerweel, J., Dabiri, D., and Gharib, M. (1997). The effect of a discrete window offset on the accuracy of cross-correlation analysis of digital PIV recordings. *Exp. Fluids*, 23:20–28.
- Westerweel, J. and Scarano, F. (2005). Universal outlier detection for PIV data. *Exp. Fluids*, 39:1096–1100.
- White, F. M. (1991). *Viscous fluid flow*. McGraw-Hill.
- Wiberg, R. and Lior, N. (2005). Heat transfer from a cylinder in axial turbulent flows. *Int. J. Heat Mass Tran.*, 48(8):1505–1517.
- Willert, C. (1996). The fully digital evaluation of photographic PIV recordings. *Appl. Sci. Res.*, 56(2–3):79–102.
- Witte, P. (2006). Temperature measurements in Rayleigh-Bénard convection using thermochromic liquid crystals. Master's thesis, Delft University of Technology, Faculty of Applied Sciences, Department of Multi-Scale Physics.
- Wu, X.-Z., Kadanoff, L. P., Libchaber, A., and Sano, M. (1990). Frequency power spectrum of temperature fluctuations in free convection. *Phys. Rev. Lett.*, 64(18):2140–2143.
- Wu, X.-Z. and Libchaber, A. (1991). Non-Boussinesq effects in free thermal convection. *Phys. Rev. A*, 43(6):2833–2839.
- Wu, X.-Z. and Libchaber, A. (1992). Scaling relations in thermal turbulence - the aspect-ratio dependence. *Phys. Rev. A*, 45(2):842–845.
- Xi, H.-D. and Xia, K.-Q. (2008a). Azimuthal motion, reorientation, cessation, and reversal of the large-scale circulation in turbulent thermal convection: A comparative study in aspect ratio one and one-half geometries. *Phys Rev. E.*, 78(3):036326.
- Xi, H.-D. and Xia, K.-Q. (2008b). Flow mode transitions in turbulent thermal convection. *Phys. Fluids*, 20:055104.
- Xia, K.-Q., Sun, C., and Zhou, S.-Q. (2003). Particle image velocimetry measurement of the velocity field in turbulent thermal convection. *Phys. Rev. E*, 68(6):066303.
- Zocchi, G., Moses, E., and Libchaber, A. (1990). Coherent structures in turbulent convection, an experimental study. *Physica A*, 166(3):387–407.

Zoldi, S. M., Liu, J., Bajaj, K. M. S., Greenside, H. S., and Ahlers, G. (1998). Extensive scaling and nonuniformity of the Karhunen-Loève decomposition for the spiral-defect chaos state. *Phy. Rev. E*, 58(6):R6903.

Nomenclature

Constants

σ_B	Stefan-Boltzmann constant	$5.670 \times 10^{-8} \text{ W m}^{-2} \text{ K}^{-4}$
c	Speed of light in vacuum	$2.998 \times 10^8 \text{ m s}^{-1}$
g	Standard gravitational acceleration	9.81 m s^{-2}
ϵ_0	Vacuum permittivity	$8.854 \times 10^{-12} \text{ F m}^{-1}$
μ_0	Vacuum permeability	$1.256 \times 10^{-6} \text{ N A}^{-2}$

Greek symbols

α	Angle	$^\circ$
α	Scaling exponent	
α	Stringency parameter for PIV validation	
α	Thermal expansion coefficient	K^{-1}
α_n, β	Non-dimensional fit parameters	
δ	Boundary layer thickness	m
δ_z	Depth of field	m
ϵ	Emissivity	
ϵ_{ijk}	Einstein notation for cross product	
ϵ	Dissipation of kinetic energy	$\text{m}^2 \text{s}^{-3}$
η	Dynamic viscosity of a fluid	Pa s
η_C	Corrsin scale	m
η_K	Kolmogorov scale	m
Γ	Aspect-ratio	
γ	Scaling exponent Rayleigh number	
κ	Thermal diffusivity	$\text{m}^2 \text{s}^{-1}$
λ	Thermal conductivity	$\text{W m}^{-1} \text{K}^{-1}$
λ	Wavelength	nm
λ_n	Peak wavelength of light travelling along helical axis	nm
λ_p	Peak wavelength	nm
λ_0	Wavelength (laser)	nm
λ_n	Eigenvalue of mode n	$\text{m}^3 \text{s}^{-2}$
λ_T	Thermal boundary layer height	m
λ_u	Kinetic boundary layer height	m
$\Delta\lambda$	Reflection bandwidth	m
μ	Dynamic viscosity	Pa s
ν	Kinematic viscosity	$\text{m}^2 \text{s}^{-1}$

Nomenclature

ω_p^*	Dimensionless peak frequency	
ω_p	Peak circular frequency	rad
ϕ_{LC}	Liquid crystal concentration	vol. %
ϕ_n	Orthogonal spatial basis function of mode n	$m^{-\frac{1}{2}}$
φ	Displacement angle	$^\circ$
ρ	Density	$kg\ m^{-3}$
$\rho(\tau)$	Autocorrelation function	
ρ'	Density fluctuation	$kg\ m^{-3}$
ρ_0	Reference density	$kg\ m^{-3}$
$\delta\rho$	Density difference	$kg\ m^{-3}$
σ	Electrical conductivity	$S\ m^{-1}$
σ_T	Standard deviation in T	K
$\sigma_u, \sigma_v, \sigma_w$	Standard deviation in u, v, w	$m\ s^{-1}$
τ	Time lag	s
τ_D	Characteristic time scale	s
τ_η	Time micro scale	s
θ	Angle between laser beams	rad
$\Theta, \Theta_t, \Theta_i, \Theta_v$	Angle, total angle, illumination angle, viewing angle	$^\circ$
θ_p	Number of particles passing a measurement volume	s^{-1}
ζ	Diagonal length ($\sqrt{H^2 + W^2}$)	m

Roman symbols

A_p	Cross section of the measurement volume	m^2
A_\perp	Infinitesimal unit area	m^2
a_n	Dimensionless coefficient of mode n	
B_{surf}	Magnetic field at surface	T
\vec{B}, \vec{B}_0	Magnetic field, reference magnetic field	T
B	Blue intensity	
$C(t, t')$	Two-point temporal correlation tensor	$m^3\ s^{-3}$
C_f	Friction factor	
C_p	Concentration of particles	m^{-3}
c_p	Specific heat capacity at constant pressure	$J\ kg^{-1}\ K^{-1}$
D	Vortex diameter $\sqrt{x^2 + y^2}$	m
D_a	Aperture diameter	m
D_k	Turb. kinetic energy transport by viscous forces	$m^2\ s^{-3}$
d	Distance	m
d_{diff}	Diffraction limited spot size	m
d_f	Fringe spacing	mm
d_1	Size of an interrogation area	m
d_i	Particle image diameter	m
d_p	Diameter of a particle	mm
E	Total energy of the flow field	$m^3\ s^{-2}$
\vec{E}	Electric field	$V\ m^{-1}$
\vec{e}_d	Unit vector of scattered light	
$\vec{e}_{i,2}$	Unit vectors	
F_1	Correlation left after in-plane motion of tracer particles	
F_0	Correlation left after out-of-plane motion of tracer particles	
\vec{F}_L	Lorentz force	N
\vec{F}	Force	N

f	Focal length	m
f_D	Doppler frequency	Hz
f_s	Frequency shift	Hz
$f^\#$	Numerical aperture	
f_i	Body force in i direction	N m^{-3}
$f_n(\Theta)$	Arbitrary function of Θ	
$f_{0,1,2}$	Frequency	Hz
$f_{i,\text{em}}$	Electromagnetic body force	N m^{-3}
$f_{i,\text{g}}$	Gravitational body force	N m^{-3}
\vec{f}	Force per unit volume	N m^{-3}
\vec{g}	Gravitational acceleration vector	$\text{m}^2 \text{s}^{-1}$
G	Green intensity	
δH	Uncertainty in hue	$^\circ$
H	Height	m
H	Hue	$^\circ$
HSI	Hue-saturation-intensity triplet	
HSV	Hue-saturation-value triplet	
h	Heat transfer coefficient	$\text{W m}^{-2} \text{K}^{-1}$
h_{EM}	Characteristic height EM experiment	mm
Ha	Hartmann number	
I	Intensity	
i, j	Integer coordinates	
dI	Infinitesimal amount of charge	A
$\hat{I}_{1,2}$	Fourier transformed image	
j_x	x -component of the current density	A m^{-2}
\vec{j}	Current density vector	A m^{-2}
k	Kinetic energy	$\text{m}^2 \text{s}^{-2}$
k'	$\frac{1}{2}u_i^2$	$\text{m}^2 \text{s}^{-2}$
L	Typical length scale	m
M	Image magnification factor	
m	Integer value	
N	Magnetic interaction parameter (Stuart number)	
N	Total number of samples	
N_i	Particle image concentration	
Nu	Nusselt number	
$N_{\mathcal{T}}$	Total number of eigenmodes	
n	Mode number	
n_o	Refraction index of orthogonal component	
n_p	Refraction index of parallel component	
Δn	Magnitude of birefringence	
\bar{n}	Mean refractive index	
P	Chiral pitch	m
P	Power	W
P_k	Production of kinetic energy	$\text{m}^2 \text{s}^{-3}$
Pr	Prandtl number	
p	Pressure	Pa
p'	Pressure fluctuation	Pa
\bar{p}	Ensemble average of pressure	Pa
p'	Dimensionless pressure	
P_k	Turb. kinetic energy transport by pressure fluctuations	$\text{m}^2 \text{s}^{-3}$
Q	Volumetric water flow rate	l min^{-1}
q	Point charge	C
q''_{cond}	Conductive heat flux	W m^{-2}

Nomenclature

q''_{conv}	Convective heat flux	W m^{-2}
q''_{rad}	Radiative heat flux	W m^{-2}
q''	Heat flux	W m^{-2}
Q_1, Q_2, Q_3	Signals	
R	Correlation	
R	Red intensity	
R_C	Mean background correlation	
R_D	Displacement correlation	
R_F	Noise due to random particle correlation	
$R_{i,j}$	Correlation at pixel i, j	
RGB	Red, green, and blue, red-green-blue triplet	
Ra	Rayleigh number	
Ra_c	Critical Rayleigh number	
Re	Reynolds number	
Re_m	Magnetic Reynolds number	
Re_τ	Shear-Reynolds number	
Re_c^*	Reynolds number based on plate length and outer velocity	
Re_x	Reynolds number based on distance x	
r_p	Radius of a particle	mm
\vec{r}	Molecular director	m
S	Saturation (HSV)	
\vec{s}	Particle displacement	m
T	Temperature	K
T_{bulk}	Bulk temperature	K
T_{surf}	Surface temperature	K
ΔT	Temperature difference	K
δT	Maximum temperature difference	K
δT	Temperature difference	K
δT	Uncertainty in temperature	K
\hat{T}	Dimensionless temperature	
T'	Temperature fluctuation	K
T_0	Reference temperature	K
\bar{T}	Ensemble average of temperature	K
\bar{T}	Mean temperature	K
\mathcal{T}_{EM}	Characteristic timescale EM experiment	s
\mathcal{T}	Measurement time	s
\mathcal{T}_k	Turb. kinetic energy transport by velocity fluctuations	$\text{m}^2 \text{s}^{-3}$
t, t'	Time	s
t^*	Typical convective turn-over time	s
Δt	Time difference	s
\tilde{t}	Dimensionless time	
U	Characteristic velocity	m s^{-1}
u_{bl}	Velocity in the boundary layer	m s^{-1}
u_{bulk}	Velocity in the bulk	m s^{-1}
u_{EM}	Characteristic velocity EM experiment	mm s^{-1}
u_{RB}	Characteristic velocity RB convection experiment	mm s^{-1}
u'_i	Velocity fluctuation of sample i (in Sect. 3.1)	m s^{-1}
u_η	Velocity micro scale	m s^{-1}
u_τ	Friction velocity	m s^{-1}
u_i	Velocity in i direction	m s^{-1}
u_i	Velocity of sample i (in Sect. 3.1)	m s^{-1}
u'_i	Fluctuating part of the i^{th} velocity component	m s^{-1}
\vec{u}	Velocity vector	m s^{-1}

Δu	Velocity difference	m s^{-1}
\tilde{u}_i	Dimensionless velocity	
$\overline{u'_i u'_i}$	Reynolds stress	$\text{m}^2 \text{s}^{-2}$
$\overline{u'_i T'}$	Turbulent heat flux	m K s^{-1}
\bar{u}	Ensemble average of the velocity	m s^{-1}
\bar{u}_i	Ensemble average of velocity in i direction	m s^{-1}
V	Arbitrary volume	m^3
V	Voltage	V
V	Value (HSV)	
u_{\max}	Maximum in-plane velocity	m s^{-1}
u_x, u_y, u_z	Velocity component in x -, y -, z -direction	m s^{-1}
$\tilde{u}_{\text{surr}}(i, j)$	Median of vectors surrounding central vector at (i, j)	m s^{-1}
W	Width	m
w_{\max}	Maximum out-of-plane velocity	m s^{-1}
w_i	Weight factor for the i th sample	
x	Position vector	m
x_{bulk}	x -coordinate of measurement location in the bulk	m
y_{bulk}	y -coordinate of measurement location in the bulk	m
z_{bulk}	z -coordinate of measurement location in the bulk	m
x_0, y_0	Coordinates of the correlation peak in pixels	
x_i	i -th component of the position vector	
x, y, z	Coordinates	m
\tilde{x}_i	Dimensionless position	
$\Delta x, \Delta y, \Delta z$	Grid size	m
z_{bl}	Measurement location in the boundary layer	m
Δz_0	Thickness of the light sheet	m

Acronyms

acf	Autocorrelation function
CCD	Charge-coupled device
CMOS	Complementary metal oxide semiconductor
DC	Direct current
DNS	Direct numerical simulations
EM	Electromagnetic
FFT	Fast Fourier transform
FT	Fourier transform
K-L	Karhunen-Loève
LC	Liquid crystal
LCT	Liquid crystal thermography
LDA	Laser Doppler anemometry
LDV	Laser Doppler velocimetry
LES	Large eddy simulation
LSC	Large-scale circulation
MHD	Magnetohydrodynamics
Nd	Neodymium
NdFeB	Neodymium-iron-boron
pdf	Probability density function
PIV	Particle-image velocimetry
PLIF	Planar laser-induced fluorescence

Nomenclature

PVC	Polyvinyl chloride
RBC	Rayleigh-Bénard convection
RB	Rayleigh-Bénard
rms	root-mean-square
sdf	Spectral density function
SNR	Signal-to-noise ratio
TLC	Thermochromic liquid crystal
WIDIM	Window displacement iterative multi-grid
YAG	Yttrium aluminium garnet, $Y_3Al_5O_{12}$
YLF	Yttrium lithium fluoride, $LiYF_4$

List of publications

- VERDOOLD, J., ROSSI, L., TUMMERS, M. J., HANJALIĆ, K. (2003) Towards electromagnetic control of thermal convection, *Proc. of the 7th International Symposium on Fluid control, measurement and visualization*, August 25-28, 2003.
- VERDOOLD, J., WITTE, P., HOEK, L., TUMMERS, M. J., HANJALIĆ, K. (2005) Identification and electromagnetic control of structures in Rayleigh-Bénard convection, *Proc. of the 4th International Symposium on Turbulence and Shear Flow Phenomena*, June 27-29, 2005.
- VERDOOLD, J., WIBOWO, A. B., TUMMERS, M. J., HANJALIĆ, K. (2006) Electromagnetic control of Rayleigh-Bénard convection, *Proc. of the 5th Symposium on Turbulence, Heat and Mass Transfer*, September 26-29, 2006.
- VERDOOLD, J., TUMMERS, M. J., HANJALIĆ, K. (2006) Oscillating large-scale circulation in turbulent Rayleigh-Bénard convection, *Phys. Rev. E* **73**, 056304.
- KENJEREŠ, S., VERDOOLD, J., WIBOWO, A.B., KLEIJN, C.R., HANJALIĆ, K. (2007) Large eddy simulations of electromagnetically driven vortical flows, *Proceedings of the 11th EUROMECH European Turbulence Conference*, June 25-27 2007, University of Porto, Porto, Portugal, **117**, 656–658, *Advances in Turbulence XI*, Springer Proceedings in Physics, Springer Verlag, Berlin
- VERDOOLD, J., VAN REEUWIJK, M., TUMMERS, M. J., JONKER, H.J.J., HANJALIĆ, K. (2008) Spectral analysis of boundary layers in Rayleigh-Bénard convection, *Phys. Rev. E* **77**, 016303.
- KENJEREŠ, S., VERDOOLD, J., TUMMERS, M. J., HANJALIĆ, K. AND KLEIJN, C. R. (2008) Numerical and experimental study of electromagnetically driven vortical flows, *Proceedings of the 7th International ERCOFTAC Symposium on Turbulence Modelling and Measurements, ETMM-7*, 4-6 June 2008, Limassol, Cyprus, **2**, 364–369.
- VERDOOLD, J. TUMMERS, M.J., AND HANJALIĆ, K. (2009) Prime modes of circulation in large-aspect-ratio turbulent Rayleigh-Bénard convection, *Phys. Rev. E*, **80**, 3, 037301.

- KENJEREŠ, S., VERDOOLD, J., TUMMERS, M. J., HANJALIĆ, K. AND KLEIJN, C. R. (2009) Numerical and experimental study of electromagnetically driven vortical flows, *Int. J. Heat Fluid Flow*, **30**, 3, 494–504.
- VERDOOLD, J., TUMMERS, M. J., HANJALIĆ, K. (2010) Digital particle image velocimetry and thermometry in turbulent Rayleigh-Bénard convection. (*in preparation*)

Long-term unsteadiness and large-scale structures in Rayleigh-Bénard convection with and without electromagnetic forcing

This dissertation focuses on turbulent thermal convection, which occurs in a wide range of (geo)physical situations, like in the atmosphere, the oceans, the interior of stars or planets, and engineering applications, like metal casting or crystal growth processes.

In this work, a special type of thermal convection, Rayleigh-Bénard convection, is studied with and without an additional electromagnetic body force. Experiments are performed in a rectangular RB convection cell of aspect-ratio $\Gamma=4$ filled with water. Particle image velocimetry (PIV), laser Doppler anemometry (LDA), and liquid crystal thermography (LCT) measurements are used to obtain velocity and temperature information.

The first part of this dissertation describes an investigation of the large-scale circulation (LSC) in Rayleigh-Bénard convection. In the second part, a study of the boundary layers in Rayleigh-Bénard convection is described. The last part reports on the control and enhancement of the heat transfer in Rayleigh-Bénard convection using an additional electromagnetic body force.